UNIVERSITY OF CALIFORNIA, SAN DIEGO

Mixed valency and electronic structure in self-assembled monolayers, self-exchange, and hydrogen bonded assemblies

A dissertation submitted in partial satisfaction of the requirements for the degree of Doctor of Philosophy

in

Chemistry

by

John Christopher Goeltz

Committee in charge:

Professor Clifford P. Kubiak, Chair
Professor Mevlin Y. Okamura
Professor Michael J. Sailor
Professor Michael J. Tauber
Professor F. Akif Tezcan

2011

The dissertation of John Christopher Goeltz is approved, and it is acceptable in quality and form for publication on microfilm and electronically:

Chair

University of California, San Diego

2011

DEDICATION

This dissertation is dedicated to Melissa, for more love and support than I can describe on page iv and to my family, blood relations and otherwise.

EPIGRAPH

These are the good times, people.

The Presidents of the United States of America

TABLE OF CONTENTS

LIST OF FIGURES

LIST OF TABLES

ACKNOWLEDGEMENTS

I find myself halfway through the 21st grade with many, many people to acknowledge for helping me get this far. I will do my best to be complete, not only to show my gratitude in writing, but also because it is heartwarming and simply fun to remember how many great people have shown up in the course of life thus far. Most luckily of all, they show no sign of stopping.

My parents set me on course for non-stop learning at an early age. My mother tells me I spontaneously turned from the pre-school bully into a pre-school leader and never looked back. My father let me learn on my own but was happy to help with guidance whenever asked. They helped me get in Yale, and they helped me through it. They were supportive of another 5-6 years of schooling, and indeed my father is nearing the completion of his Ph. D. as I write this.

I also met with much support through the Montclair public school system. Mrs. Rennie and Ms. Rinaldi taught me to wonder in 2nd and 3rd grades. Mr. Rossenagel told me I could sing and that I was bound for Princeton. Boy, was he mistaken. Ms. Axton told me I could sing, and by then she was right. Mr. Dickerson and Mr. Kyle taught me very little history, through no fault of their own, but more importantly managed to teach me to write a bit. Mr. Orso imparted to me a cynical love of chemistry, which persists to this day to both my gain and detriment.

Yale was truly a remarkable place. In my very first year I met Charlie Schmuttenmaer, who may be the biggest fan Snafoo still has. He encouraged me to explore Yale's chemical engineering major in a way so supportive and fun I stayed in chemistry. Later, Ann Valentine would set the bar for teaching coordination chemistry, and even now I have not seen a better instructor in the subject. Prof. J. Michael McBride would advise my senior research, and let me learn the AFM the hard way. I now would sooner become a biologist than use that instrument again, but that is a story for another set of preliminary pages. Prof. McBride did manage to instill in me an understanding of dynamic

equilibrium and crystallization kinetics that I think few other graduate students have even by the end of their theses.

Unquestionably the most instrumental person in leading me to independent research was Prof. K. Travis Holman of Georgetown. I worked in his laboratory for just one semester, and really enjoyed the freedom and lack of pressure from above. He was happy to teach me crystallography and help with synthesis when I was stuck, but was also happy to do his thing and just see what I could do.

I would not say Snafoo had an advisor, but I did receive a lot of support in those days. The list of friends who helped me then really is too long to print, so those other than Richmond, Josh, Bins, Priber, Ian, and Fat Mike will just have to believe me when I say I appreciate them.

Professor Clifford P. Kubiak is a good advisor. He appreciates joke telling as an art form, with Groucho Marx and Rodney Dangerfield as the old masters. He likes pale ales as well as wine. He believes bread should be good, and agrees with me that California bagels are actually some form of roll. Maybe most importantly he lets students succeed and fail on their own. There were times when this was not at all a fun way to do research, but Cliff's students come out able to speak with other professors in their own language and hold their own, and often able to sneak in a jab or two, and this is an invaluable skill.

Cliff likes to say that his students choose him, he doesn't choose them, and it is unquestionably true. Without the help and support of Catherine, Johnny, Caballero, Joey, Kristina, Aaron, Starla, Smieja, Eric, Candace, Bhupi, and Gabe, I would be either working at HomeBrew Mart or in a bar in Brooklyn. Most days I'm glad I'm not. H. Paul, Katey, and Beedle, despite having chosen inferior labs, were also key in helping me maintain what remains of my brains.

This all leads up to thanking the person most instrumental in helping me get where I am. Melissa has not only put up with a lot of crap from me in San Diego, she has been encouraging the entire time. I cannot find adequate words to thank her for everything she has done, so she will have to content herself to know she is loved.

SPECIFIC CHAPTER ACKNOWLEDGMENTS

Chapter 2: Much of the material in this chapter comes directly from a manuscript entitled, "Mixed valence self-assembled monolayers: polarizabilities of the mixed valence states," by John C. Goeltz and Clifford P. Kubiak, which has been published in *J. Phys. Chem. C* **2008**, *112* (22), 8114-8116.

Chapter 3: Much of the material in this chapter comes directly from a manuscript entitled "Rates of electron self-exchange reactions between oxo-centered ruthenium clusters are determined by orbital overlap," by John C. Goeltz, Christina J. Hanson and Clifford P. Kubiak, which has been published in *Inorg. Chem.*, **2009**, *48* (11), 4763–4767.

Chapter 4: Much of the material in this chapter comes directly from a manuscript entitled "Electronic structural effects in self-exchange reactions," by John C. Goeltz, Eric E. Benson and Clifford P. Kubiak, which has been published in *J. Phys. Chem. B*, **2010**, *114* (45), 14729-14734.

Chapter 5: Much of the material in this chapter comes directly from a manuscript entitled "Mixed valency across hydrogen bonds," by John C. Goeltz and Clifford P. Kubiak, which has been published in *J. Am. Chem. Soc.*, **2010**, *132* (49), 17390-17392.

VITA

2003	Bachelor of Science, Yale University
2007	Master of Science, University of California, San Diego
2011	Doctor of Philosophy, University of California, San Diego

PUBLICATIONS

Goeltz, J. C.; Glover, S. D.; Hauk, J.; Kubiak, C. P. "Basic ruthenium acetate and mixed valence derivatives" *Inorg. Synth.* **2011**, in press.

Goeltz, J. C.; Kubiak, C. P. "Mixed valency across hydrogen bonds" *J. Am. Chem. Soc.* **2010,** *132,* 17390-17392.
http://dx.doi.org/10.1021/ja108841k

Goeltz, J. C.; Benson, E. E.; Kubiak, C. P. "Electronic structural effects in self-exchange reactions" *J. Phys. Chem. B,* **2010,** *114*, 14729-14734.
http://dx.doi.org/10.1021/jp103009b

Dreyse, P. A.; Isaacs, M. A.; Iturriaga, P.E.; Villagra, D. A.; Aguirre, M. J.; Kubiak, C. P.; Glover, S. D.; Goeltz, J. C. "Electrochemical preparation of conductive films of tetrapyridylporphyrins coordinated to four [Ru(5-NO2-phen)(2)Cl](+) groups" *J. Electroanal. Chem.* **2010,** *648,* 98-104.
http://dx.doi.org/10.1016/j.jelechem.2010.08.007

Arshad, M. N.; Mough, S. T.; Goeltz, J. C.; Holman, K. T. "Methyl 3,5-bis[(4-hydroxymethyl-2-methoxyphenoxy)methyl]benzoate" *Acta Cryst. E,* **2010,** *66,* O703.
http://dx.doi.org/10.1107/S160053681000677X

Glover, S. D.; Goeltz, J.C.; Lear, B. J.; Kubiak, C.P. "Inter- or intramolecular electron transfer between triruthenium clusters: we'll cross that bridge when we come to it" *Coord. Chem. Rev.,* **2010,** *254,* 331-345.
http://dx.doi.org/10.1016/j.ccr.2009.09.005

Glover, S. D.; Goeltz, J. C.; Lear, B. J.; Kubiak, C. P. "Mixed Valency at the Nearly Delocalized Limit: Fundamentals and Forecast" *Eur J. Inorg. Chem.,* **2009,** *5,* 585-594.
http://dx.doi.org/10.1002/ejic.200800910

Goeltz, J. C.; Hanson, C. J.; Kubiak, C. P. ”Rates of electron self-exchange reactions between oxo-centered ruthenium clusters are determined by orbital overlap” *Inorg. Chem.*, **2009,** *48*, 4763–4767. http://dx.doi.org/10.1021/ic8022024

Goeltz, J. C.; Kubiak, C. P. “Mixed valence self-assembled monolayers: electrostatic polarizabilities of the mixed valence states” *J. Phys. Chem. C*, **2008,** *112*, 8114-8116. http://dx.doi.org/10.1021/jp802209u

Drain, C. M.; Bazzan, G.; Milic, T.; Vinodu, M; Goeltz, J. C. “Formation and Applications of Stable 10 nm to 500 nm Supramolecular Porphyrinic Materials” *Isr. J. Chem.* **2005,** *45*, 255-269. http://dx.doi.org/10.1560/9QTD-B1GJ-K8J7-7YJR

Mough, S. T.; Goeltz, J. C.; Holman K. T. "Isolation and Structure of an 'Imploded' Cryptophane" *Angew. Chem. Int. Ed.* **2004,** *43*, 5631–5635. http://dx.doi.org/10.1002/anie.200460866

ABSTRACT OF THE DISSERTATION

Mixed valency and electronic structure in self-assembled monolayers, self-exchange, and hydrogen bonded assemblies

by

John Christopher Goeltz

Doctor of Philosophy in Chemistry

University of California, San Diego, 2011

Professor Clifford P. Kubiak, Chair

Mixed valency and electron transfer are explored in self-assembled monolayers, in intermolecular electron self-exchange reactions in solution, and in hydrogen bonded assemblies. Tetrathiafulvalene is derivatized for binding to gold in self-assembled monolayers, but the trinuclear ruthenium cluster $Ru_3O(OAc)_6L_3$ (where L is an ancillary ligand) is used as a building block for the majority of the work. While oxo-centered trinuclear hexaacetate clusters of many transition metals are known, the triruthenium cluster is particularly versatile because of the kinetically stable binding of a wide variety of ligands.

The electronic structure can be depicted by molecular orbitals diagrams or more recently by computer generated combinations of atomic orbitals, and remains relatively unchanged for variously substituted clusters. The important differences with respect to getting an electron in or out of a cluster lie in electron delocalization onto ligand based orbitals. In combination with reorganization energies calculated from accumulated structural and vibrational data, the molecular orbital diagrams offer a great deal of explanatory power. When allowed by symmetry and energy matching, electrons in reduced clusters are delocalized onto pyridine π^* orbitals, greatly easing the transfer to an oxidized cluster in the face of a large reorganization energy. When electron delocalization is not allowed, electron self-exchange can be fast only if the reorganization energy is small.

In hydrogen bonded assemblies of these ruthenium clusters, the electronic structure is still dominant in electron transfer behavior. In these cases the increase in delocalization upon dimerization appears to induce large changes in the orbital energies. This is consistent with the electronic absorptions and the thermal electron transfer behavior observed.

The take-home message of this dissertation is that one must understand to electronic structure of a complex in order to understand its behavior in electron transfer reactions. This may seem obvious, but is often overlooked. With the knowledge of the electronic structure of reactants and products, one has a much greater chance of understanding the path between them. Molecular orbital diagrams seem cumbersome and outdated in this age of calculated chemistry, but many cases drawing them out is worth the investment in time. Who knows, you may even learn something.

Chapter 1

Electron transfer is not the most important thing in chemistry. It is the only thing.

1.1 Introduction

Jay Kochi was arguably nuts. He regularly berated students and post-doctoral researchers into leaving of their own accord, rather than graduate them or help them find academic positions.[1] He broke into offices because he was convinced other professors were spying on him.[2] After many years and many seriously useful contributions to organic chemistry,[3-4] he became utterly fixated on one particular phenomenon: electron transfer in donor-acceptor complexes.[5-7]

He may have seen the world a little differently than some of us, but that does not mean he was wrong on all accounts. Electron transfer and transport, electron donor-acceptor interactions, the distribution of molecular charge, and the timescales for each of these are of paramount importance in describing physical phenomena and getting them to go your way.

This thesis is primarily concerned with the intersections of electron transfer with other areas of research. The first section explores mixed valency in self-assembled monolayers (SAMs) of alkyl thiols on gold surfaces. The second describes the effects of electronic structure on electron self-exchange reactions in solution. The third attempts a foray into a dangerously overpopulated field: proton-coupled electron transfer, or PCET. While many researchers focus on photochemically induced PCET, we chose to focus on ground state mixed valency across a hydrogen bonded assembly. That choice brought with it its own set of challenges, but allowed us to plant a flag on a small peak where only one flag had been previously planted, and it had already all but blown away.

1.2 Mixed valence self-assembled monolayers

Self-assembled monolayers of thiols and isocyanides on gold (111) surfaces have been explored fundamentally,[8-10] for charge transport,[11] for sensing applications,[12-14] and for molecular

computing.[15] While our lab has made contributions in each of these areas, it is the last in particular that is described in this thesis.

Dr. John C. Stires IV found that charge transfer (CT) complexes of arene electron donors with the electron acceptor tetracyanoethylene displayed vastly increased conductance relative to the arenes themselves,[16] and we speculated that devices could be made by patterning areas of high and low conductance in a monolayer. We considered various masking and dip-pen nanolithography schemes based on forming a monolayer of aryl thiol on gold, then selectively adding tetracyanoethylene. This is still open to investigation as we chose instead to explore bistable mixed valence molecules as precursors to molecular computing.

If the essence of computing is bits of information, ones and zeroes, then a bistable molecule possesses the proper number of states to function as a bit. By orienting a mixed valence molecule vertically in a monolayer, a chemist might switch between the two possible electronic occupancies, the "up" and "down" states, by applying an electric field. A simple version is depicted in Figure 1-1.

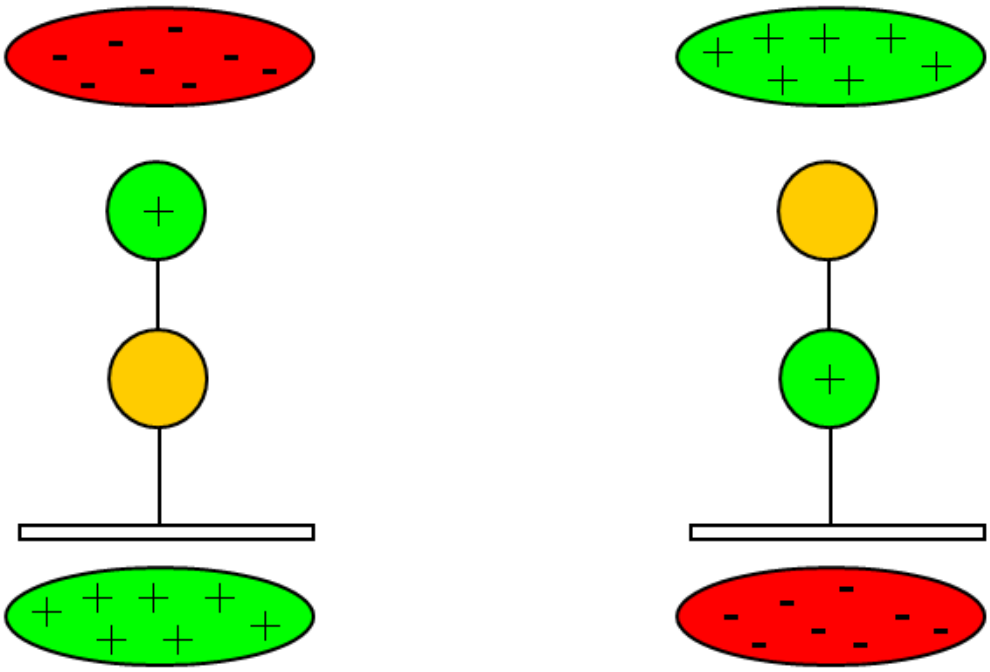

Figure 1-1. Simplified depiction of mixed valence SAM acting as a switchable bit with an electric field as the actuator.

Functional computing involves not only switching but readout in an appropriate form and high levels of gain.[17] A bistable surface-bound molecule could be envisaged as a bit for memory, with a large applied DC electric field "writing" the bit to an up or down state and a small AC field "reading" the state of the bit, though the thermal barrier for equilibration is a natural concern.

We succeeded in demonstrating differences in polarizability in different oxidation states of mixed valence SAMs.[18] The tetrathiafulvalene (TTF) molecule chosen for the study has a delocalized charge in the mixed valence state, depicted in Figure 1-2. This precluded studies of bistability, but allowed us to explore electric field-based atomic force microscope techniques with an air-stable SAM.

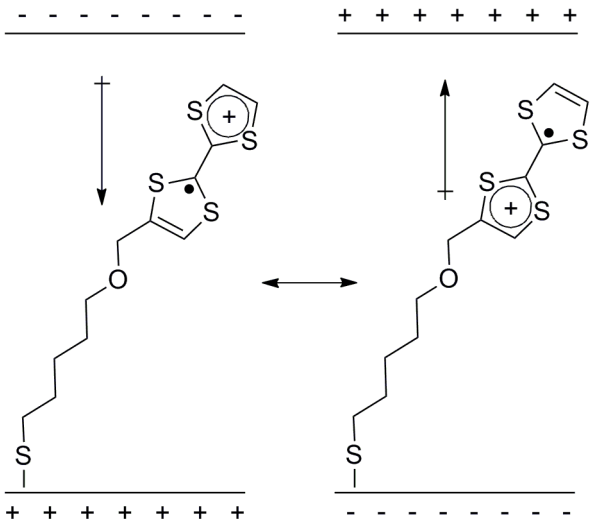

Figure 1-2. Monocationic tetrathiafulvalene SAM, showing delocalized charge. Note that the double sided arrow indicates resonance and not exchange.

Biferrocene-based monolayers were also synthesized to allow access to bistable mixed valence cations, but met with no demonstration of bistability or polarizability in Kelvin probe force microscopy (KFM) or electric force microscopy (EFM) techniques. Engineers at the AFM company Veeco also tried scanning capacitance microscopy (SCM), but were unable to see any nonlinear capacitance. It was never clear whether the issue was signal-to-noise, switching and sensing

timescales, stability, inappropriate applied AC or DC electric fields, some combination, or simply something of which we never thought.

Work reported by the Lent and Fehlner laboratories at Notre Dame describing quantum cellular automata (QCA) comes closest to this type of molecular dipolar switching, though their nomenclature sells their work short.[19-21] They performed a macroscale AC capacitance measurement with a mixed valence monolayer sandwiched between a mercury electrode and a highly doped silicon substrate. Upon sweeping an applied DC field between the electrodes, they found capacitive switching behavior that varied widely with the counterions used to balance the charge in their silicon-bound molecular dipoles. They published two derivatives of their first molecule, a thiol bound to gold and an alkyl bound to silicon via Grignard chemistry, but only reported switching behavior in the silicon monolayers. Incidentally, Benjamin J. Lear told me at the beginning of my work in this area he thought my experiments would only work on silicon. I asked him why, and he responded that he did not know why, it was just a feeling. It is possible that the biferrocenium monolayers would respond to this type of capacitive measurement, which is essentially just impedance spectroscopy. With a tunable frequency, one might even be able to tease out the rate constant for intramolecular electron transfer.

1.3 Self-exchange in solution: electronic structure can be the key to electron self-exchange reactions

Christina Hanson, a very talented UCSD undergraduate, developed an experimental NMR protocol for studying electron self-exchange between oxo-centered ruthenium clusters in different oxidation states. Using this method, we found that for clusters of the type $Ru_3O(OAc)_6(CO)(L)_2^{0/-}$ where L is a pyridyl ligand, the rate of self-exchange was fast (10^6-10^8 M^{-1} s^{-1}) but highly dependent on the electron donating ability of the ligand.[22] We later found that exchange between clusters of the type $Ru_3O(OAc)_6(L)_3^{+/0}$ where L is again a pyridyl ligand was also fast (10^7-10^9 M^{-1} s^{-1}), but was *not* determined by the donor ability of the ligand.[23]

Eric E. Benson was able to crystallize $Ru_3O(OAc)_6(py)_3^+PF_6^-$ where py is pyridine. Comparison with the reported structure of $Ru_3O(OAc)_6(py)_3$ and vibrational data allowed the direct calculation of the reorganization energy λ. Figure 1-3 shows an overlay of the two structures. The total reorganization energy was found to be 3320 – 5120 cm^{-1}, depending on the nigh unknowable electron transfer distance, r. This energy is actually quite small for such a large cluster, and is in agreement with oxidation/reduction of the Ru_3O core and not the peripheral ligands.

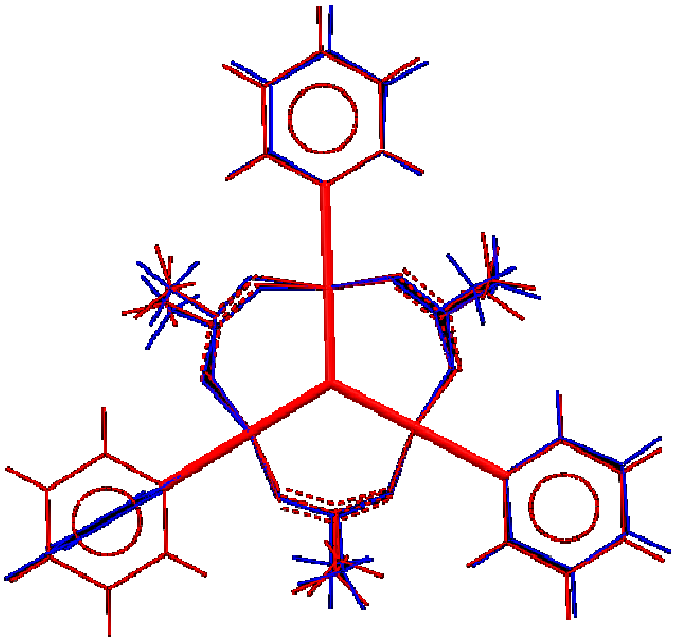

Figure 1-3. Overlay of the crystal structures of $Ru_3O(OAc)_6(py)_3$ (red) and $Ru_3O(OAc)_6(py)_3^+PF_6^-$ (blue). One pyridine ring is out of plane in the oxidized cluster.

The reorganization energies of the $Ru_3O(OAc)_6(CO)(L)_2^{0/-}$ clusters have been estimated at 11000 cm^{-1}.[24] It might be expected to be larger than the reorganization energy for the trispyridyl cluster 0/+ exchange, as the electron density delocalizes onto the pyridine π* orbitals in the reduced states of the former and not of the latter.[25] It is also instructive to examine the Marcus-Hush rate

expression and the electronic coupling[26-27] in the face of the experimentally determined rate constants and reorganization energies discussed in detail in chapters 3 and 4.

$$k_{ET} = \left(2H_{ab}{}^{2} / h\right)\left(\pi^{3} / \lambda RT^{1/2}\right)\exp\left[-\frac{(\lambda - 2H_{ab})^{2}}{4\lambda RT}\right] \quad (1)$$

Equation 1 describes the predicted electron transfer rate constant k_{ET} and allows us to examine the electronic coupling required to achieve certain rate constants given different reorganization energies though some assumptions must be made about the pre-exponential factor. H_{ab} is the electronic coupling in cm^{-1}, h is Planck's constant, λ is the reorganization energy in cm^{-1}, and R is the gas constant. Care must be taken to ensure all physical constants use energy units of cm^{-1}. In short, a smaller coupling is required to achieve similar rate constants in the trispyridyl systems because the reorganization energy (and thus the activation barrier) is smaller. Figure 1-4 depicts this graphically, though admittedly the first order rate constants plotted assume very concentrated solutions of intermolecularly exchanging species. The basic conclusions would be the same at nearly any set of rates (or lifetimes) for ET. The coupling is much more important to the exchange between the anionic and neutral clusters than it is to the exchange between neutral and cationic clusters.

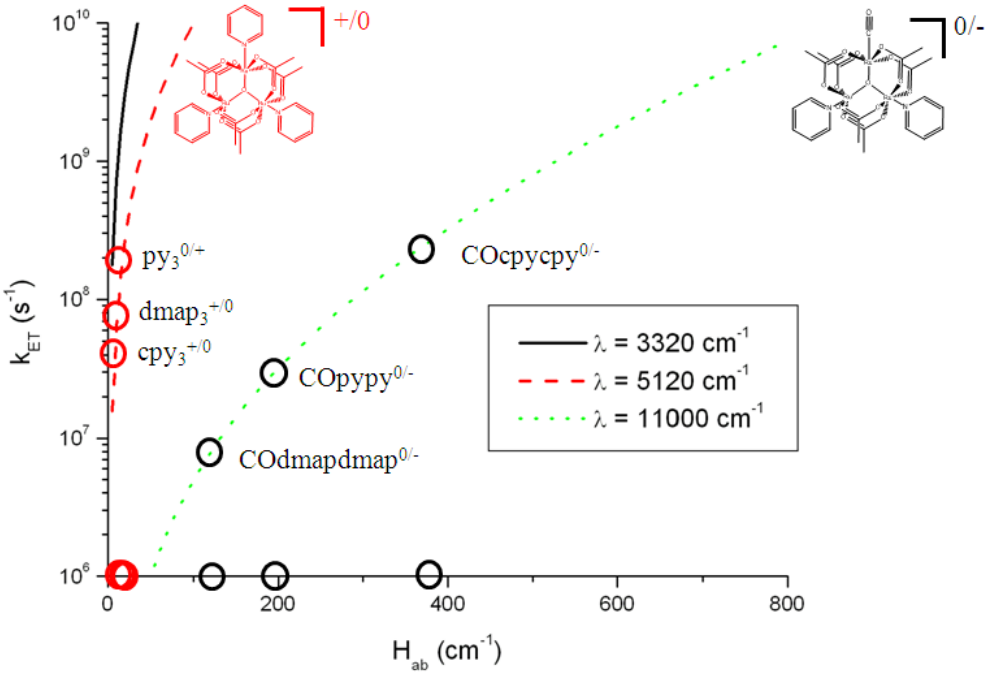

Figure 1-4. Plot of predicted k_{ET} vs. H_{ab} for the appropriate values of the reorganization energy λ. Circles indicate observed rate constants and calculated couplings.

In spite of, or perhaps because of its simplicity, this study ended up being the most gratifying of the three described in this thesis. Reorganization energies are often discussed, but almost never calculated from structural data. In this case the ability to compare directly reorganization energies and rate constants for two exchange reactions demanded a consistent framework as well as a full description of the orbitals involved in exchange. Those of us who study electron transfer sometimes neglect to visualize the orbitals in favor of thinking about the myriad other parameters that can describe the exchange. We often ask "where are the electrons?" but the answer is always the same, no matter the system: the orbitals.

1.4 Mixed valency across hydrogen bonds

To say that mixed valency and proton-coupled electron transfer (PCET) have been explored fully would be wrong. To say they have been explored *ad nausuem* would indicate a jaded

commentator. But even the most jaded[28] would agree that the intersection of the two, ground state mixed valency across hydrogen bonds has barely had its surface scratched.[29] Proton-coupled mixed valency could give insight into the interplay of hydrogen bonding and electronic structure, the "burn-out" rate for hydrogen bonds in the face of electron density, and possibly even a thermodynamic measure of electronic coupling by comparison of dimerization constants in isovalence and mixed valence states.

We envisioned several options for linking the $Ru_3O(OAc)_6(CO)(L)_2$ clusters through non-covalent interactions, with a few shown in Figure 1-5. In the end we selected the simplest option that would give access to a hydrogen bonded interface, the commercially available ligand isonicotinic acid, or 4-pyridine carboxylic acid. This choice was in part due to the many experimental and theoretical studies of photoinduced electron transfer across carboxylic acid based hydrogen bonds, exemplified by the work of Therien,[30] Nocera,[31-33] and Cukier.[34] These researchers found an unsatisfyingly wide variety of kinetic isotope effects with k_H/k_D ranging from 1-2, but in general found that hydrogen bonds were as good for electron transfer as unsaturated bridges, and were typically better than saturated bridges.

The term proton-coupled mixed valency requires that the electron transfer be coupled to the proton coordinate. In the two proton symmetric system at the bottom of Figure 1-5, that may or may not be the case. To stay on the safe side of those in the field for whom nomenclature is the name of the game,[32, 35-36] we opted for the phrase "mixed valency across hydrogen bonds."

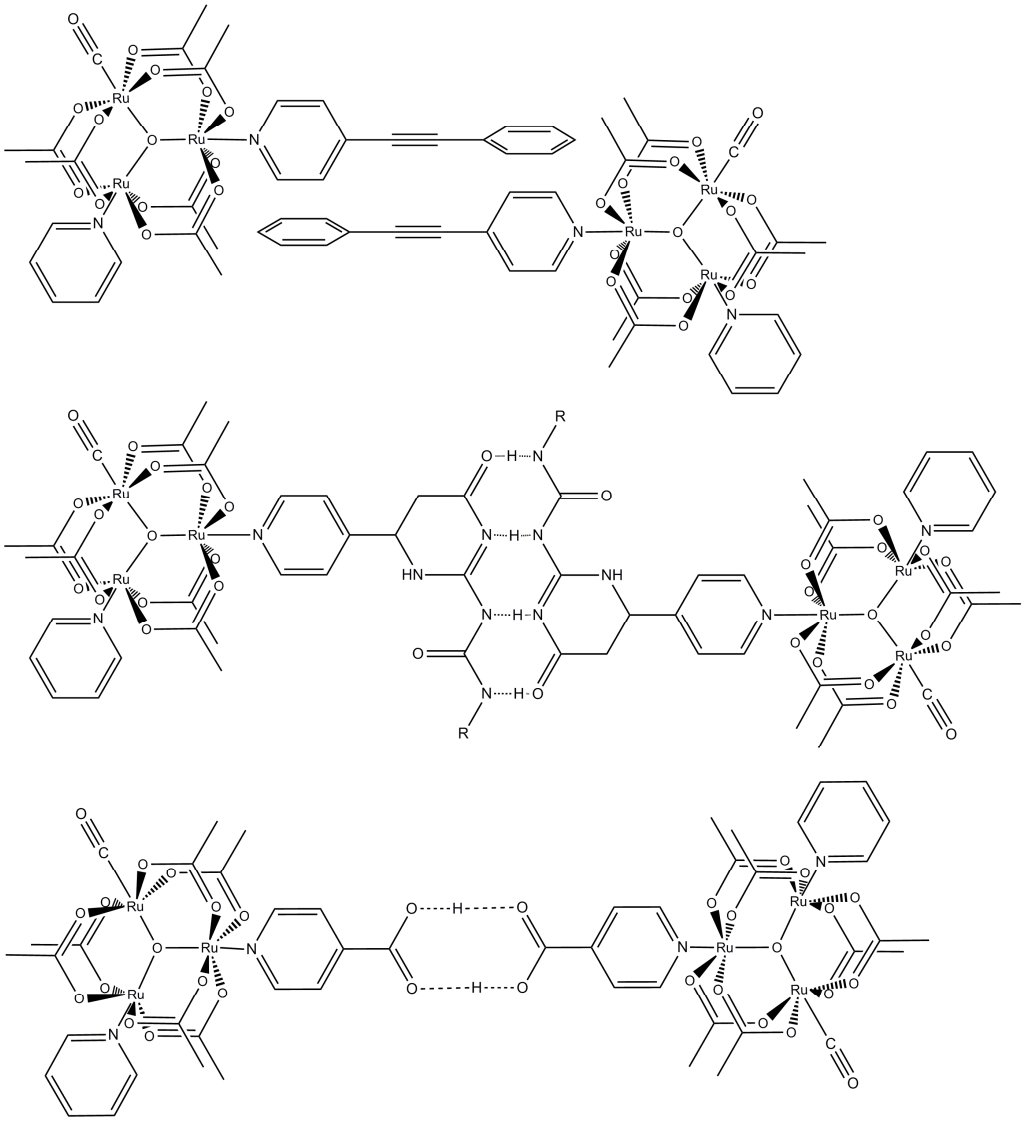

Figure 1-5. Proposed structures for noncovalent interactions between oxo-centered ruthenium clusters.

The obvious questions for such an assembly concern the electronic coupling, the electrochemical splitting, the electron transfer rate constant, dimerization equilibria, the kinetic isotope effect, and intervalence charge transfer bands. The oxo-centered ruthenium clusters have many things in their favor in such a study, most importantly a wide variety of spectroscopic handles. The carbonyl and carboxylic acid group are good infrared reporters. The proton resonances tend to be discernable in ^{1}H NMR spectra in all oxidation states. Electrochemistry is typically well behaved

and reversible. Intervalence and intracluster charge transfer bands are often convoluted, but can yield quite a bit of physical insight.

As it turned out, the stability of the hydrogen bonded clusters in reduced states was a major experimental issue. The entire study hinged on the electronic spectroscopy, as no reviewer in his or her right mind would look favorably on such a piece of work without a cogent explanation of the optical charge transfer phenomena.

Low temperature air-free UV/vis/near IR spectroelectrochemistry was the obvious answer, but it turned out that those who regularly report such experiments rarely actually fulfill all those requirements at the same time.[37-41] The published cell designs functioned well enough with platinum electrodes, but preclusion of proton reduction in these systems required gold mesh working and counter electrodes. Simply because gold is softer, the cells broke frequently and were not reliable. Finally some measure of success was had, and spectra for several oxidation states of two compounds were obtained in two solvents.

In the most frequently successful experiment, a 1 mm pathlength quartz cuvette was sealed with a 19/22 septum in a glove box after being charged with a known volume of solution of known concentration of the neutral species of interest. An airtight syringe with a solution of the reducing agent decamethylcobaltocene was inserted into the top of the syringe. The assembly was brought out and chilled to -20 ºC in a temperature controlled sample holder in the instrument. When the interlock disabling switch was in an appropriate mood, the sample compartment could be covered with a black cloth with the syringe sticking up out of the instrument, and spectra could be taken after injecting small amounts of reductant and briefly mixing the resulting solution. The concentration of analyte in each spectrum could be calculated from the initial concentration and volume and the volume of reductant solution added. A nitrogen flush was maintained in the instrument whenever the compartment was cooled to preclude excess water condensation and light scattering in the sample chamber.

When the interlock disabling switch was behaving badly, a piece of PTFE tubing was threaded through the septum before assembly, and the syringe was stuck in the end of the tube before

removal from the glove box. Then the tubing was run out the door of the instrument so that the compartment could remain closed. This setup did not perform as well as the aforementioned syringe-septum experiment, perhaps due to diffusion of oxygen through the walls of the PTFE tubing.

Once electronic spectra were obtained for several hydrogen bonded mixed valence dimers in several solvents, analysis could progress with more confidence. A molecular orbital (MO) approach once proved instructive, especially in comparison with the MO description of the intermolecular self-exchange. Both are detailed in chapter 6 and aid in explaining the electronic spectra of many a reduced ruthenium cluster.

The dimer shown at the bottom of Figure 1-5 ended up as the best understood system reported at the time for studying mixed valency across hydrogen bonds,[42] and still it begs for further characterization. Perhaps the dimerization equilibrium constants could be teased out in some way not yet thought of, yielding a true measure of the combined strength of electron delocalization and hydrogen bonds. Perhaps the rate of decomposition could be accurately measured, giving an estimate of the burn-out rate for hydrogen bonds in proteins or other natural systems where electron transfer may have necessitated the evolution of a repair mechanism. Or perhaps the two electron, two proton laden fully reduced dimer could be used as a PCET catalyst.

1.5 References

1. Dibrov, S., *private communication* **2008**.
2. Kubiak, C. P., *private communication* **2008**.
3. Srinivasan, K.; Michaud, P.; Kochi, J. K., *J. Am. Chem. Soc.* **1986,** *108*, 2309-2320.
4. Tamura, M.; Kochi, J., *Synthesis* **1971**, 303-&.
5. Howell, J. O.; Goncalves, J. M.; Amatore, C.; Klasinc, L.; Wightman, R. M.; Kochi, J. K., *J. Am. Chem. Soc.* **1984,** *106*, 3968-3976.
6. Kochi, J. K., *Acc. Chem. Res.* **1974,** *7*, 351-360.
7. Kochi, J. K., *Angew. Chem. Int. Ed.* **1988,** *27*, 1227-1266.

8. Bain, C. D.; Troughton, E. B.; Tao, Y. T.; Evall, J.; Whitesides, G. M.; Nuzzo, R. G., *J. Am. Chem. Soc.* **1989,** *111*, 321-335.
9. Bain, C. D.; Whitesides, G. M., *Science* **1988,** *240*, 62-63.

10. Troughton, E. B.; Bain, C. D.; Whitesides, G. M.; Nuzzo, R. G.; Allara, D. L.; Porter, M. D., *Langmuir* **1988,** *4*, 365-385.

11. Adams, D. M.; Brus, L.; Chidsey, C. E. D.; Creager, S.; Creutz, C.; Kagan, C. R.; Kamat, P. V.; Lieberman, M.; Lindsay, S.; Marcus, R. A.; Metzger, R. M.; Michel-Beyerle, M. E.; Miller, J. R.; Newton, M. D.; Rolison, D. R.; Sankey, O.; Schanze, K. S.; Yardley, J.; Zhu, X. Y., *J. Phys. Chem. B* **2003,** *107*, 6668-6697.

12. Chhabra, R.; Sharma, J.; Ke, Y.; Liu, Y.; Rinker, S.; Lindsay, S.; Yan, H., *J. Am. Chem. Soc.* **2007,** *129*, 10304-10305.

13. Xiao, Y.; Piorek, B. D.; Plaxco, K. W.; Heeger, A. J., *J. Am. Chem. Soc.* **2005,** *127*, 17990-17991.

14. Zayats, M.; Huang, Y.; Gill, R.; Ma, C.-a.; Willner, I., *J. Am. Chem. Soc.* **2006,** *128*, 13666-13667.

15. Emerging Research Devices. In *International Technology Roadmap for Semiconductors*, 2005; pp 27-28.

16. Stires, J. C.; Kubiak, C. P.; Tao, N. J., *unpublished results*.

17. Keyes, R. W., *Science* **1985,** *11*, 138-144.

18. Goeltz, J. C.; Kubiak, C. P., *J. Phys. Chem. C* **2008,** *112*, 8114-8116.

19. Li, Z.; Beatty, A. M.; Fehlner, T. P., *Inorg. Chem.* **2003,** *42*, 5707-5714.

20. Li, Z.; Fehlner, T. P., *Inorg. Chem.* **2003,** *42*, 5715-5721.

21. Qi, H.; Gupta, A.; Noll, B. C.; Snider, G. L.; Lu, Y.; Lent, C.; Fehlner, T. P., *J. Am. Chem. Soc.* **2005,** *127*, 15218-15227.

22. Goeltz, J. C.; Hanson, C. J.; Kubiak, C. P., *Inorg. Chem.* **2009,** *48*, 4763-4767.

23. Goeltz, J. C.; Benson, E. E.; Kubiak, C. P., *J. Phys. Chem. B* **2010**, ASAP.

24. Londergan, C. H.; Salsman, J. C.; Lear, B. J.; Kubiak, C. P., *Chem. Phys.* **2006,** *324*, 57-62.

25. Goeltz, J. C.; Benson, E. E.; Kubiak, C. P., *J. Phys. Chem. B* **2010,** *114*, 14729-14734.

26. Brunschwig, B. S.; Creutz, C.; Sutin, N., *Chemical Society Reviews* **2002,** *31*, 168-184.

27. Sutin, N., *Prog. Inorg. Chem.* **1983,** *30*, 441-498.

28. Smieja, J. M.; Kubiak, C. P., *Inorg. Chem.* **2010,** *49*, 9283-9289.

29. Sun, H.; Steeb, J.; Kaifer, A. E., *J. Am. Chem. Soc.* **2006,** *128*, 2820-2821.

30. Derege, P. J. F.; Williams, S. A.; Therien, M. J., *Science* **1995,** *269*, 1409-1413.

31. Hsu, T. L. C.; Engebretson, D. S.; Helvoigt, S. A.; Nocera, D. G., *Inorg. Chim. Acta* **1995,** *240*, 551-557.

32. Irebo, T.; Reece, S. Y.; Sjödin, M.; Nocera, D. G.; Hammarström, L., *J. Am. Chem. Soc.* **2007,** *129*, 15462-15464.

33. Papoutsakis, D.; Kirby, J. P.; Jackson, J. E.; Nocera, D. G., *Chem. Eur. J.* **1999,** *5*, 1474-1480.

34. Cukier, R. I.; Nocera, D. G., *Annu. Rev. Phys. Chem.* **1998,** *49*, 337-369.

35. Sjodin, M.; Styring, S.; Akermark, B.; Sun, L. C.; Hammarstrom, L., *J. Am. Chem. Soc.* **2000,** *122*, 3932-3936.

36. Mayer, J. M., *Annu. Rev. Phys. Chem.* **2004,** *55*, 363-390.

37. Roy, S., *private communication*.

38. Ito, T.; Hamaguchi, T.; Nagino, H.; Yamaguchi, T.; Kido, H.; Zavarine, I. S.; Richmond, T.; Washington, J.; Kubiak, C. P., *J. Am. Chem. Soc.* **1999,** *121*, 4625-4632.

39. Kaim, W.; Fiedler, J., *Chem. Soc. Rev.* **2009,** *38*, 3373-3382.

40. Hartl, F., *Inorg. Chim. Acta* **1995,** *232*, 99-108.

41. Vanoutersterp, J. W. M.; Hartl, F.; Stufkens, D. J., *Inorg. Chem.* **1994,** *33*, 2711-2712.

42. Goeltz, J. C.; Kubiak, C. P., *J. Am. Chem. Soc* **2010,** *132*, 17390-17392.

Chapter 2

Mixed valence self-assembled monolayers: electrostatic polarizabilities of the mixed valence states

2.1 Introduction

The transfer of information to and from single molecules *via* external physical probes remains the key challenge to realization of functional molecular devices.[1] This chapter describes studies of the electronic delocalization of mixed valence ions organized in self assembled monolayers (SAMs) and probed by Kelvin probe force microscopy (KFM). Mixed valency and electronic delocalization in small molecules have been the subjects of considerable theoretical and experimental work.[2-6] Despite the many proposed applications of the electronic bistability and potentially very fast exchange times of mixed valence ions, little has been reported about their response to an applied electric field in oriented monolayers.[7-9]

In general, mixed valence ions are classified in the Robin-Day scheme.[10] The electric polarizability (i.e. response to an electric field) is expected to be greatest in a Robin-Day class III (delocalized) system. The mixed valence ion TTF^+ has been assigned as a Robin-Day class III system,[3-4] and partially oxidized charge transfer complexes of TTF with π-acceptors such as tetracyanoquinodimethane (TCNQ) and tetracyanoethylene (TCNE) have been studied.[11] Such TTF mixed valence complexes are relatively air-stable, and surface bound species have been reported,[12-13] making compound **1** (Figure 2-1) a good system for atomic force microscopy in air. This chapter discusses the polarizabilities of **1** in various oxidation states, quantified as the ability of the molecular dipole to respond to an external electric field.

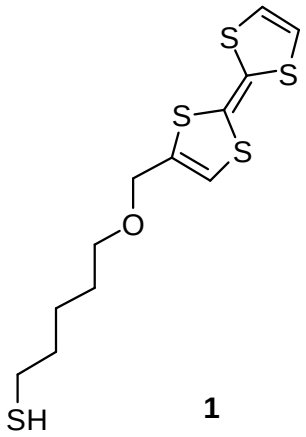

1

Figure 2-1. Tetrathiafulvalene derivitized for binding to Au.

2.2 Results and discussion

The neutral molecule **1** (Figure 2-1) was synthesized according to literature procedures[12-13] and deposited as a SAM on flame annealed Au surfaces from 0.1 mM MeCN solutions over >48 hours. The mixed valence ion $\mathbf{1}^+$ was then prepared from SAMs of neutral **1** by exposing the surface to ~10 mM ferrocenium hexafluorophosphate in CH_2Cl_2. The partially charge separated (charge transfer) complex, **1**-TCNE, was co-deposited from 0.1 mM **1**, 1mM TCNE MeCN solution.

Electrochemical measurements of SAMs of **1** confirm surface-bound species and a stable mixed valence ion. The cyclic voltammetric response of SAMs of **1** displays two reversible one-electron oxidations corresponding to the $\mathbf{1}/\mathbf{1}^+$ and $\mathbf{1}^+/\mathbf{1}^{2+}$ couples, $E_{1/2}(0/+)$ = -0.003 V, $E_{1/2}(+/2+)$ = +0.400 V vs. ferrocene/ferrocenium in acetonitrile, and persists without loss after repeated scanning. The peak current of each wave is proportional to scan rate (see Figure 2-2).

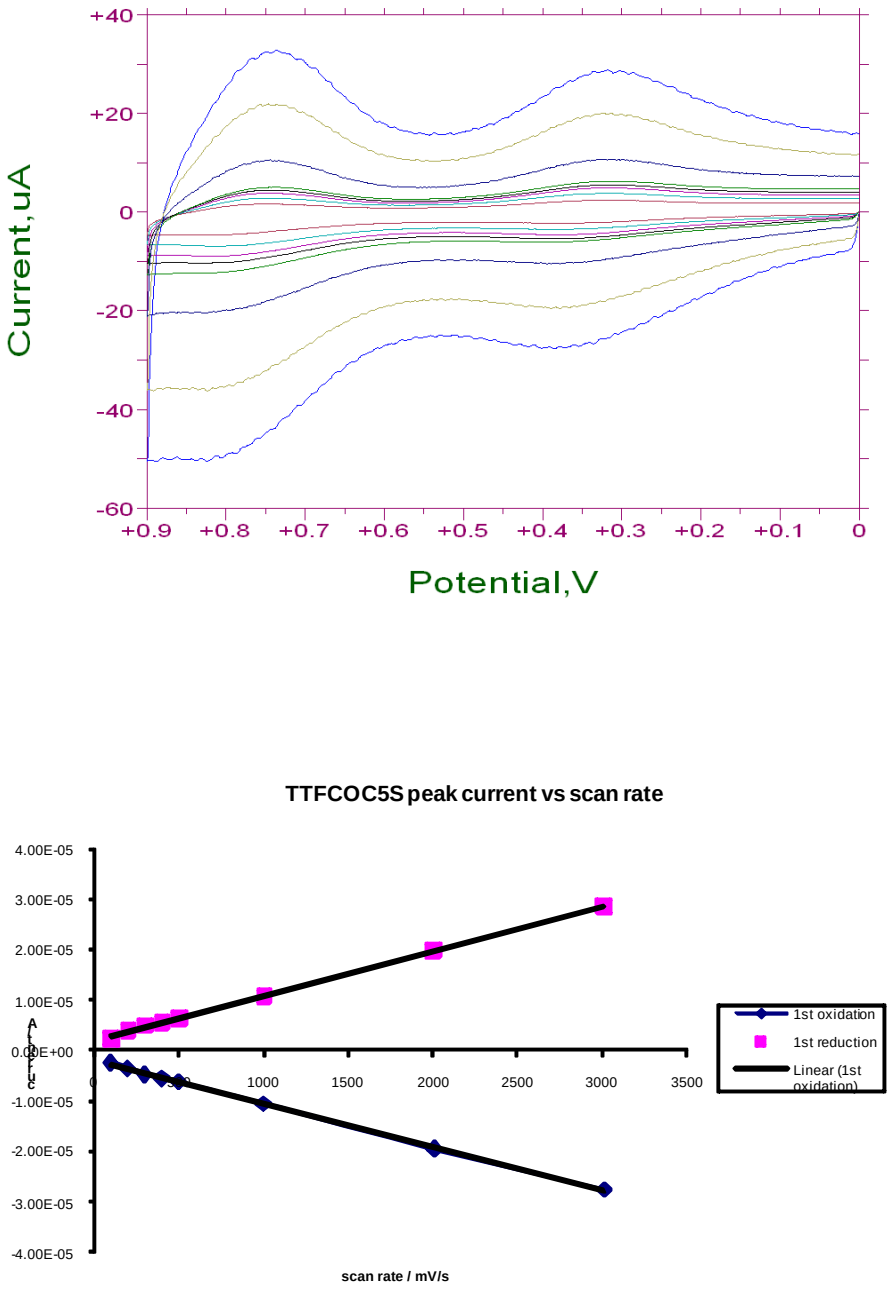

Figure 2-2. Electrochemistry of a SAM of **1** on Au in acetonitrile (vs. Ag wire) and a plot of peak current versus scan rate for the **1**/**1**$^{+}$ couple.

Surface infrared (PM-IRRAS) analysis of **1** confirms its presence on the surface of Au, and the narrow bandshapes observed qualitatively demonstrate good monolayer ordering (Figure 2-3). PM-IRRAS also was used to characterize the mixed valence state, **1**$^{+}$. A strong ν(PF) band of PF_6^- at

862 cm^{-1}, and new broad bands *ca*. 3500, 3200, and 1500 cm^{-1} correspond closely to bands observed in the liquid phase IR spectrum of TTF^+ (Figure 2-4). Significant enhancement of the ether C-O stretch at 1125 cm^{-1} is also characteristic of oxidation to $\mathbf{1}^+PF_6^-$. The PM-IRRAS of a SAM of the charge transfer complex **1**-TCNE reveals that the ν(CN) stretch of TCNE is shifted to 2201 cm^{-1} (compared to 2257 cm^{-1} for the free molecule). Good correlations between ν(CN) and the degree of partial charge transfer, δ^-, to TCNE exist,[14] and we conclude that $\delta = 0.85$ for the SAM of **1**-TCNE

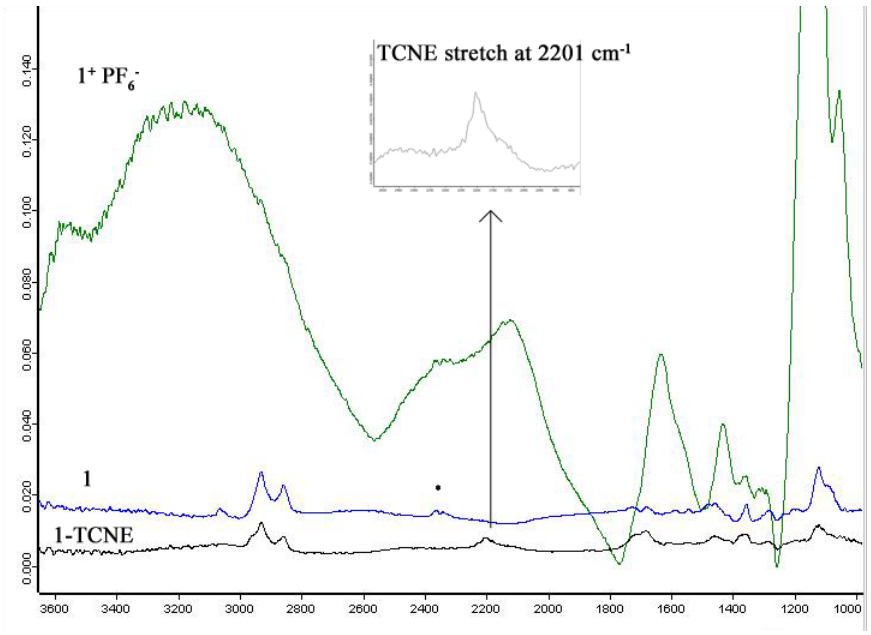

Figure 2-3. Surface infrared spectra of **1**, $\mathbf{1}^+$, and **1**-TCNE, with inset of shifted TCNE stretch at 2201 cm^{-1}. The * denotes CO_2 that was incompletely purged from the sample chamber.

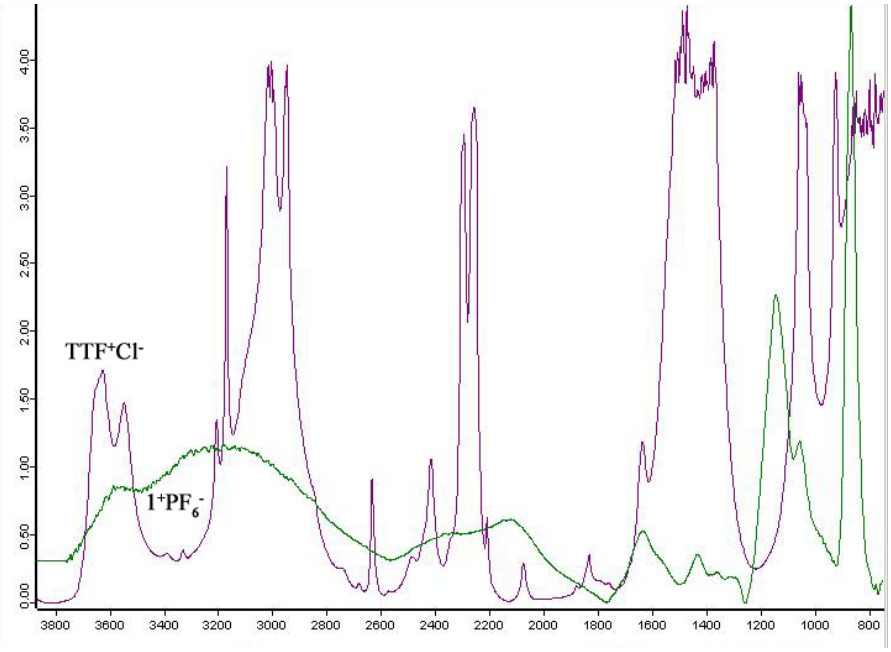

Figure 2-4. IR of TTF^+Cl^- in acetonitrile in purple and IRRAS of a SAM of $\mathbf{1}^+PF_6^-$ in green.

Kelvin probe force microscopy (KFM) is often used to determine electric fields (surface potentials or contact potential differences) due to trapped charges, voltages applied to conducting substrates, or permanent dipoles of the molecular components of SAMs.[15-18] In the most common KFM experiment, an AC voltage is applied to the tip at its resonant frequency causing an oscillation as the tip becomes charged and is alternately attracted and repulsed by a static electric field emanating from the substrate. As a DC voltage between the tip and the substrate is swept, the amplitude of the oscillation changes according to the following proportionality.

$$A_{RMS} \propto \frac{dC}{dz} \Delta V_{DC} V_{AC,RMS} \tag{1}$$

Here, dC/dz is the capacitance (expressed as a gradient because it is dependent on the separation between electrodes), ΔV_{DC} is the difference between the applied voltage and the surface potential, and V_{AC} is the AC voltage.[19] The amplitude is minimized when the field from the applied

DC voltage nullifies the electric field from the sample, eliminating electrostatic forces felt by the tip. This DC voltage is taken to be the negative of the surface potential.

While usually the important result in the KFM experiment is the surface potential, in this study it is the *slope of the amplitude response* that gives information about the relative capacitances of the SAMs of **1**, **1**$^{+}PF_6^{-}$, and **1**-TCNE. As the monolayer becomes more polarizable, the positive charge delocalized on the TTF^{+} group responds to the AC field as depicted in Figure 2-5, creating an induced dipolar field in the monolayer, and decreasing the capacitance of the system. Representative plots of KFM results for SAMs of **1**, **1**$^{+}$, and **1**-TCNE are shown in Figure 2-6.

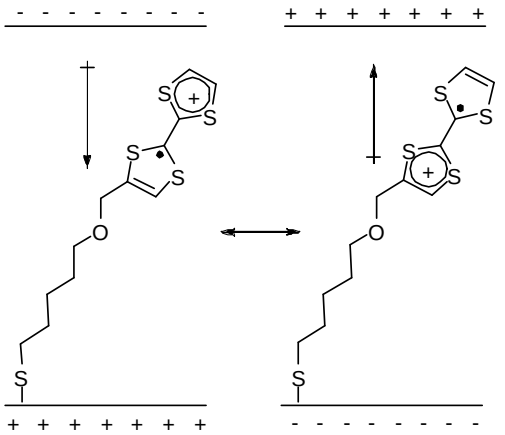

Figure 2-5. Depiction of **1**$^{+}$ opposing an applied electric field.

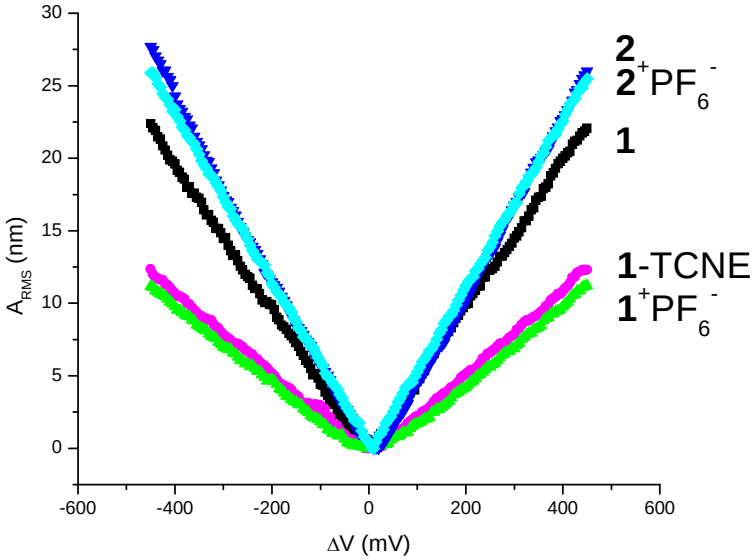

Figure 2-6. Representative KFM amplitude responses of **1**, **1**-TCNE, **1**$^{+}$PF$_6^{-}$, **2**, and **2**$^{+}$PF$_6^{-}$.

These plots depict the amplitude of the KFM tip vibration versus ΔV_{DC} normalized to an arbitrary surface potential of 0. The relative slopes (each reported value is the average of 100 measurements of the capacitive slope) reflect the relative SAM capacititances and are summarized in Table 2-1. These data show that the capacitance of **1**$^{+}$PF$_6^{-}$ is reduced to 61 % of the neutral species, and that of **1**-TCNE is reduced to 63%. Because the delocalized mixed valence TTF^{+} state and charge transfer TTF$^{+0.85}$ state are highly polarizable, the induced field in the molecule opposes the applied field, the tip feels a smaller field, and the tip oscillation at a given ΔV_{DC} is diminished. It is important to separate how much of the electrostatic polarizability of **1**$^{+}$PF$_6^{-}$ and **1**-TCNE arises from their mixed valence character, and how much from their charge separated ionic character. We therefore performed control experiments with SAMs of ferrocenepentanethiol, **2**, and the corresponding ferroceniumpentanethiol, **2**$^{+}$PF$_6^{-}$. The SAM of **2**$^{+}$PF$_6^{-}$ displayed 92±2% of the capacitance of a neutral SAM of **2**. This is far less than the differences in capacitance of 61% and 63% for SAMs of **1**$^{+}$PF$_6^{-}$ and **1**-TCNE respectively compared to neutral SAMs of **1**. These data show

that the major contribution to the electrostatic polarizability of a mixed valence ion is its delocalized electronic structure, and not its charge separated ionic state.

Table 2-1. KFM amplitude slopes with ESDs, and relative capacitances of each SAM.

monolayer	KFM response slope (nm/mV)	Relative capacitance
1	0.045(3)	1.00
1-TCNE	0.0284(4)	0.63
$\mathbf{1}^{+}PF_6^{-}$	0.0274(5)	0.61
2	0.063(2)	1.00
$\mathbf{2}^{+}PF_6^{-}$	0.058(1)	0.92

2.3 Conclusions

This chapter describes the first analysis of the polarizability of delocalized mixed valence molecules organized in SAMs. The polarizability increases in the order TTF, $TTF^{+0.85}$, TTF^{+}. This work demonstrates that the delocalized charge dominates the electrical response in a SAM comprised of mixed valence ions or charge transfer complexes.

2.4 Experimental

Deposition of monolayers. Gold on chromium on borosilicate glass slides were purchased from Arrandee (Werther, Germany), and annealed with 15 one second passes from a hydrogen flame immediately before use. After cooling to room temperature, the slides were immersed in 0.1 mM acetonitrile (dried and degassed) solutions of **1** for >48 hours, rinsed with acetonitrile and hexanes and blown dry with nitrogen. **1**-TCNE charge transfer monolayers were codeposited from 0.1 mM **1**, 1mM TCNE in acetonitrile, rinsed only with hexanes to avoid stripping the electron acceptor off, and blown dry with nitrogen. $\mathbf{1}^{+}PF_6^{-}$ SAMs were formed by immersing slides with monolayers of neutral

1 in a ~10 mM CH_2Cl_2 solution of ferrocenium hexafluorophosphate blanketed with argon for 45 minutes, briefly rinsing with CH_2Cl_2, then hexanes, and blowing dry with nitrogen. Infrared, electrochemical, and Kelvin probe measurements were taken immediately after rinsing and drying.

Infrared spectroscopy. Infrared spectra were taken on a Bruker Equinox 55 spectrometer. PM-IRRAS surface infrared spectra were taken with a PMA 37 photoelastic modulator (PEM) fitted with a nitrogen cooled MCT detector and a resolution of 4 cm^{-1}. The PEM was set to 2500 cm^{-1} and the detector was set at an angle of 84°. The liquid IR spectrum of tetrathiafulvalene monochloride shown with the IRRAS of $\mathbf{1}^+PF_6^-$ in Figure 2-4 was obtained by oxidizing TTF with excess $FeCl_3$ in acetonitrile in a liquid cell with CaF_2 windows. The UV-vis spectrum for TTF^+ obtained in this manner is in agreement with that in the literature, with bands at 581, 434, and 340 nm.[20]

Electrochemistry. Electrochemical measurements were made with a BAS CV-50W potentiostat and a standard three electrode cell with a platinum counter electrode, silver wire pseudo-reference and either glassy carbon or an alligator clipped gold coated glass slide with the desired monolayer serving as the working electrode. Scans were taken in 0.1 M tetrabutylammonium hexafluorophosphate in acetonitrile at 100 mV/s unless otherwise noted, and potentials are reported versus the ferrocene/ferrocenium couple measured at the same conditions (1 mM in the same electrolyte solution with a clean electrode, immediately after measurements of interest).

Kelvin probe force microscopy (KFM). KFM measurements were taken on a Veeco Multimode AFM with a Nanoscope IIIa controller, an EX-1 extender box, and software version 4.43r8, with the AFM cover on and the sample area flushed with nitrogen run through a 0.22 um filter. Veeco OSCM-PT7 platinum coated silicon tips with resonant frequencies of about 60 kHz and spring constants of about 3 N/m were used. All TTF monolayer capacitance measurements shown in this publication were made with one tip, and the measurements were all made in one day.

Gold coated glass slides with SAMs were taped to steel pucks and electrically contacted with silver paint. After a satisfactory surface potential scan (10 um area, 1 Hz scan rate) was obtained in the turn-key KFM mode, the feedback loop was turned off and the tip was held at a constant DC potential. The real-time and offline plane fits for phase and amplitude data of the lift

scans were set to “none” and the slow scan axis was disabled so that the tip traced a single 10 um line on the sample repeatedly. A DC potential was applied to the sample puck with a Pine AFCBP1 Bipotentiostat through a current limiting resistor and low pass circuit, and the AFM lock-in signal available under “phase” in the software was monitored. Voltage was applied to the sample such that the lock-in signal (and thus the electric field between the tip and the sample) was equal to 0. The sample potential was then swept from –500 mV to +500 mV relative to this potential at 5 mV/s and a KFM scan was recorded. The x-axis is distance on the surface, and the y-axis represents the changing potential over time. Data were obtained at a lift height of 0 nm so that very little air is included in the “dielectric” of the parallel plate capacitor approximation, and the relative capacitances measured are largely those of the SAMs between the tip and the gold slide. Measurements were also obtained at a lift height of 15 nm. The trends are the same, but as expected the effect was diminished since the capacitance of the air was a large part of the sample (relative to the ~1.5 nm SAM). Representative raw data scans and amplitude curves for 15 nm lift height scans are shown in Figure 2-7 and Figure 2-8.

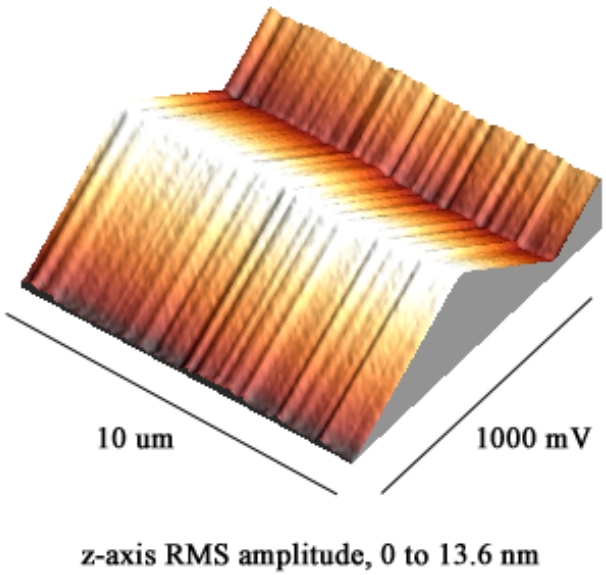

Figure 2-7. Raw KFM data for **1** at a 15 nm lift height.

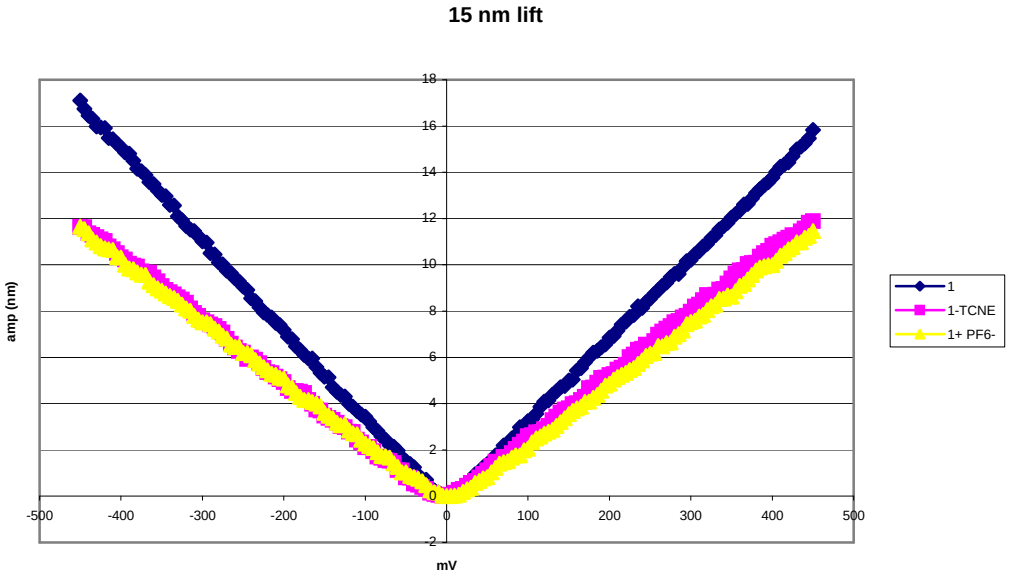

Figure 2-8. Representative KFM curves at a lift height of 15 nm.

The amplitude versus voltage curves were obtained by opening the files in WSxM 2.1 (Nanotec Electronica S.L.) and saving profile traces for the amplitude data. It should be noted that the Veeco software records the RMS tip vibration amplitude in lift mode as the measured amplitude subtracted from the amplitude setpoint for that scan, as shown in Veeco Support Note 231, Revision E. The maximum in the trace is actually a minimum in the vibration due to electrostatic forces, and the actual quantity of the recorded maximum is irrelevant to this experiment. Data shown has been inverted and normalized to a minimum of 0 nm amplitude, because only the slopes and shapes of the curves are of interest here and such a plot allows for easier comparison with other data and with defining equations.

Many calibration experiments were done to ensure confidence in the KFM measurements. The standard force calibration in the AFM software was performed for each tip used so that amplitude data would be quantitative. The potential sensitivity was calibrated by applying 100 mV to a bare gold sample with the KFM feedback loop on, and confirming that the instrument registered a surface potential difference of 100 mV. The dC/dz sensitivity was calibrated by measuring the

surface potential of decanethiol and octadecanethiol SAMs. The dependence of 18 mV per CH_2 unit found is within the accepted range of 10 to 20 mV per CH_2.[16]

Note: Much of the material for this chapter comes directly from a manuscript entitled "Mixed valence self-assembled monolayers: polarizabilities of the mixed valence states" by John C. Goeltz and Clifford P. Kubiak, which has been published in *Journal of Physical Chemistry C*, **2008**, *112* (22), 8114-8116. http://dx.doi.org/10.1021/jp802209u The dissertation author is the primary author of this manuscript.

2.5 References

1. Rocha, R. C.; Brown, M. G.; Londergan, C. H.; Salsman, J. C.; Kubiak, C. P.; Shreve, A. P., *J. Phys. Chem. A.* **2005,** *109*, 9006-9012.

2. Brunschwig, B. S.; Creutz, C.; Sutin, N., *Chem Soc Rev* **2002,** *31*, 168-184.

3. Cowan, D. O.; LeVanda, C.; Park, J.; Kaufman, F., *Acc. Chem. Res.* **1973,** *6*, 1-7.

4. Prassides, K., *Mixed Valency Systems: Applications in Chemistry, Physics, and Biology*. Kluwer Academic Publishers: Dordrecht, 1990; Vol. C343, p 451.

5. Nelsen, S. F., *Chem. Eur. J.* **2000,** *6*, 581-588.

6. Sutin, N., *Electron Transfer-from Isolated Molecules to Biomolecules, Pt 1* **1999,** *106*, 7-33.

7. Li, Z.; Beatty, A. M.; Fehlner, T. P., *Inorg. Chem.* **2003,** *42*, 5707-5714.

8. Li, Z.; Fehlner, T. P., *Inorg. Chem.* **2003,** *42*, 5715-5721.

9. Qi, H.; Gupta, A.; Noll, B. C.; Snider, G. L.; Lu, Y.; Lent, C.; Fehlner, T. P., *J. Am. Chem. Soc.* **2005,** *127*, 15218-15227.

10. Robin, M. D., P, *Adv. Inorg. Chem. Radiochem.* **1967,** *10*, 247.

11. Yuge, R.; Miyazaki, A.; Enoki, T.; Tamada, K.; Nakamura, F.; Hara, M., *J. Phys. Chem. B* **2002,** *106*, 6894-6901.

12. Garin, J.; Orduna, J.; Uriel, S.; Moore, A. J.; Bryce, M. R.; Wegener, S.; Yufit, D. S.; Howard, J. A. K., *Synthesis-Stuttgart* **1994**, 489-493.

13. Herranz, M. A.; Yu, L.; Martin, N.; Echegoyen, L., *J. Org. Chem.* **2003,** *68*, 8379-8385.

14. Stires, J. C.; McLaurin, E. J.; Kubiak, C. P., *Chem. Comm.* **2005**, 3532-3534.

15. Cherniavskaya, O.; Chen, L.; Weng, V.; Yuditsky, L.; Brus, L. E., *J. Phys. Chem. B* **2003,** *107*, 1525-1531.

16. Howell, S.; Kuila, D.; Kasibhatla, B.; Kubiak, C. P.; Janes, D.; Reifenberger, R., *Langmuir* **2002,** *18*, 5120-5125.

17. Nakamura, T.; Koyama, E.; Shimoi, Y.; Abe, S.; Ishida, T.; Tsukagoshi, K.; Mizutani, W.; Tokuhisa, H.; Kanesato, M.; Nakai, I.; Kondoh, H.; Ohta, T., *J. Phys. Chem. B* **2006,** *110*, 9195-9203.

18. Saito, N.; Lee, S.-H.; Takahiro, I.; Hieda, J.; Sugimura, H.; Takai, O., *J. Phys. Chem. B* **2005,** *109*, 11602-11605.

19. Sarid, D., *Scanning Force Microscopy*. Revised Edition ed.; Oxford University Press: New York, 1994; p 263.

20. Torrance, J. B.; Scott, B. A.; Welber, B.; Kaufman, F. B.; Seiden, P. E., *Phys. Rev. B* **1979,** *19*, 730-741.

Chapter 3

Rates of electron self-exchange reactions between neutral and reduced oxo-centered ruthenium clusters are determined by orbital overlap

3.1 Introduction

Electron self-exchange is one of the simplest chemical reactions, but also one of the most revealing. Within the context of the Marcus-Hush theory of electron transfer[1-2] (ET), rates of electron self-exchange can be related directly to the total reorganization energy for ET, λ, and by the Marcus cross relation, to rates of intermolecular ET with other redox agents.[3-4] The mixed valence states of the "dimer-of-trimer" complexes of the general type $[Ru_3O(OAc)_6(L)(CO)(\mu\text{-}BL)Ru_3O(OAc)_6(L)(CO)]^-$ (where BL = bridging ligand) have been the subject of considerable study.[5-9] Several aspects of the ET chemistry of these mixed valence ions, notably ET rates on the vibrational time scale that give rise to coalescence of infrared (IR) spectral lineshapes,[5-6] dependence of ground state ET rates on solvent dynamics,[7, 10] appearance of totally symmetric bridging ligand modes of vibration in the resonance Raman spectra measured within the intervalence charge transfer (IVCT) bands,[11] and non-Arrhenius kinetic behavior in freezing solvents[7] challenge normal two-state ET theoretical models. Here, we examine the self-exchange ET reactions of ruthenium clusters of the type $[Ru_3O(OAc)_6(CO)(L)_2]$ (Figure 3-1) which constitute "half" of the dimer of trimer mixed valence ions. The three different ancillary pyridine ligands used dictate the redox potentials of the clusters, as shown in Figure 3-2. Our intent is to determine the rates of self-exchange, individual cluster reorganization energies, and general features that will shed light on the unusual intramolecular ET properties of the pyrazine-bridged mixed valence ions that are based on the isostructural redox unit.

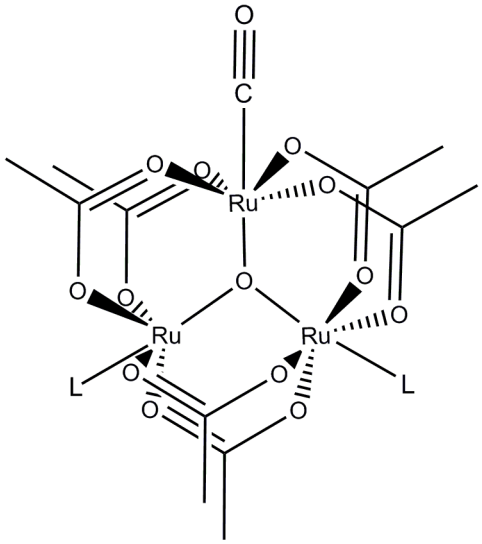

Figure 3-1. The three clusters discussed in this chapter: **1**, L = 4-cyanopyridine (cpy); **2**, L = pyridine (py); and **3**, L = 4-(dimethyl)aminopyridine (dmap).

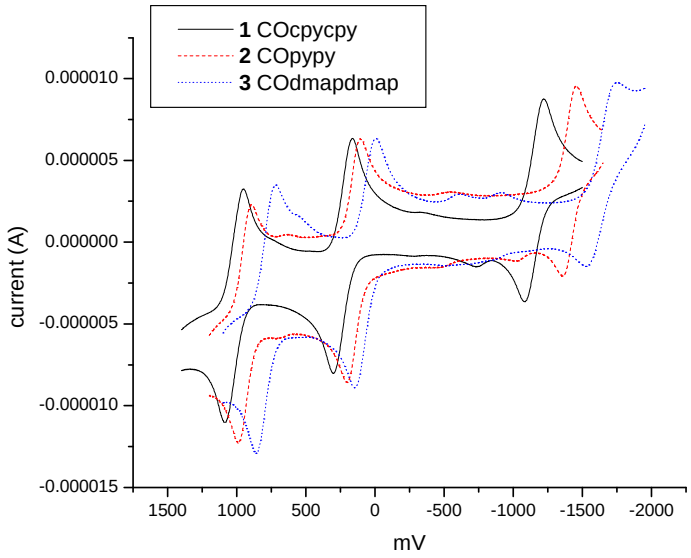

Figure 3-2. Electrochemistry of ruthenium trimers with different pyridyl ligands in CH_2Cl_2 with 0.1 M TBAH, glassy carbon working, platinum wire counter, and Fc/Fc^+ reference electrodes.

3.2 Results and Discussion

The mole fractions of diamagnetic neutral clusters and paramagnetic singly reduced clusters in a mixed solution were initially determined by IR spectroscopy. Spectra for **1** in CD_2Cl_2 are shown in Figure 3-3(a). Ratios were determined by integration of the ν(CO) bands for the neutral cluster (~1940 cm^{-1}) and the singly reduced cluster (~1900 cm^{-1}). The ν(CO) region for each mixed solution was not coalesced and could be fit to two well resolved peaks, giving an upper bound to k_{ET} of ~10^{10} – 10^{11} s^{-1} M^{-1}.[6] The exchange was in the fast regime (where $k(C_{tot}) >> 2\pi(\Delta\nu)$ on the NMR timescale, as the chemical shifts for exchanging species were averages of the diamagnetic and paramagnetic chemical shifts, weighted by their respective mole fractions. This is shown in the linear relationship in the mole fraction of reduced complex vs. acetate chemical shift in Figure 3-3(b).

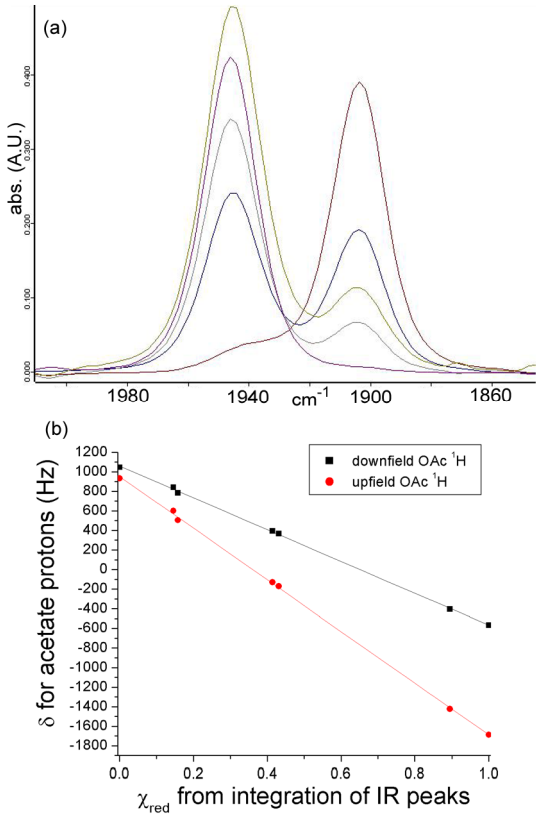

Figure 3-3. (a) IR spectra of the ν(CO) region for **1** in CD_2Cl_2, with varying mole fractions of [red]/[ox]. (b) Plot of χ_{red} determined from integration of IR peaks vs. chemical shift of acetate protons. The linear relationship confirms fast exchange on the NMR timescale.

Rate constants were determined using the equation

$$k_{ET} = \frac{4\pi\chi_d\chi_p(\Delta\nu)^2}{(W_{dp} - \chi_p W_p - \chi_d W_d)C_{tot}} \quad (1)$$

where χ_d and χ_p are the mole fractions of diamagnetic and paramagnetic species, $\Delta\nu$ is the difference in chemical shift between diamagnetic and paramagnetic species in Hz, W_{dp} is the peak width at half maximum for the mixture in question, W_d and W_p are the widths for the pure diamagnetic and paramagnetic species, and C_{tot} is the total concentration in mol L^{-1}.[12] Representative NMR spectra for **1** in CD_3CN are shown in Figure 3-4. The rate constants measured range from 10^6 to 10^8 s^{-1} M^{-1} and are shown in Table 3-1. These rate constants are comparable in magnitude to those found by

NMR for many other 0/+ and 0/- couples, though the range is remarkable for a set of analogous self-exchange couples.[13-18] In a particularly relevant study reported by Meyer, the $[Ru_3O(OAc)_6(py)3]^{0/+}$ pair exhibited $k_{ET} = 1.1x10^8\ s^{-1}\ M^{-1}$ in CD_2Cl_2.

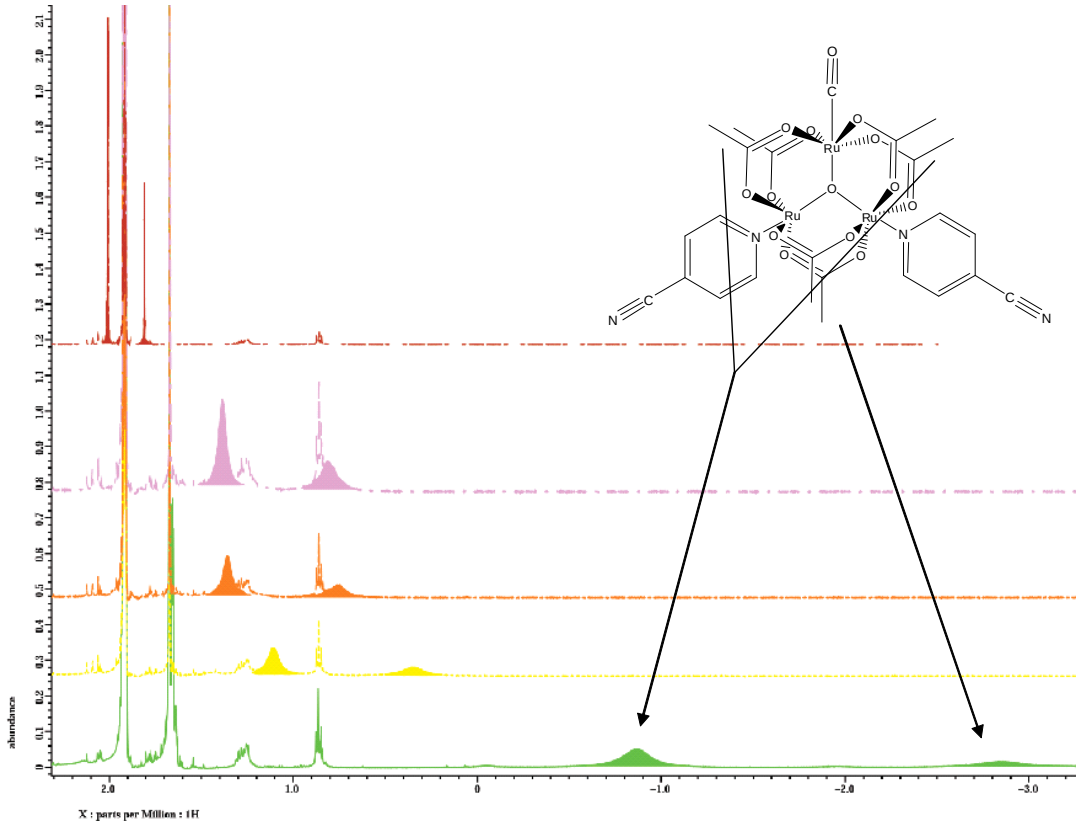

Figure 3-4. Representative ^1H NMR spectra with varying mole fractions of diamagnetic and paramagnetic **1** in CD_3CN.

Table 3-1. Electron transfer rate constants for $[Ru_3O(OAc)_6(CO)(L)_2]^{0/-}$ self-exchange reactions (x $10^7\ s^{-1}\ M^{-1}$).

	CD_3CN	THF-d_8	CD_2Cl_2
1 COcpycpy	13.	20	30
2 COpypy	1.8	20	7
3 COdmapdmap	0.7	2	-

Looking at the observed k_{ET} for complexes **1**-**3**, one trend is immediately clear: more electron withdrawing substituents on the ancillary pyridine ligands lead to faster self-exchange in all three solvents. We attribute this to increasing donor-acceptor orbital overlap, or "contact area," as more electron density is drawn onto the pyridine ligands of the $[Ru_3O(OAc)_6(CO)(L)_2]^-$ donor.

The increasing effective contact area is also clearly apparent in the increasing paramagnetic contact shift for the pyridyl protons with more electron withdrawing groups at the pyridine para position. Average $\Delta\delta$s for pyridyl protons in the three complexes and their reduced counterparts in CD_3CN are shown in Figure 3-5. As the pyridine ligand becomes less basic (lower pK_a) more electron density is drawn onto the ring in the reduced cluster, and the contact shift is greater.

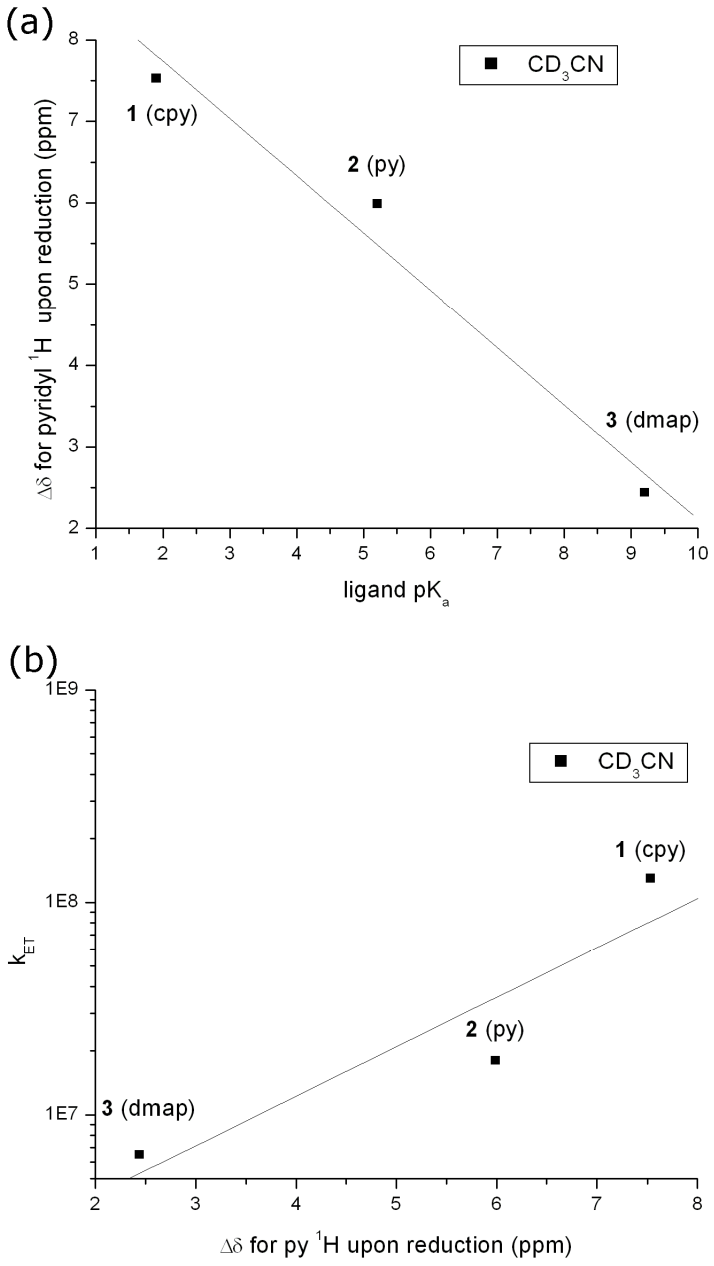

Figure 3-5. (a) Plot of ligand pK_a vs. the average change in chemical shift ($\Delta\delta$) for the pyridyl protons upon reduction of the neutral cluster in CD_3CN. (b) Plot of $\Delta\delta$ vs. k_{ET} (s^{-1} M^{-1}) illustrating that increased electron density on peripheral ligands corresponds to faster rates of ET.

A logarithmic plot of k_{ET} vs. ligand pK_a is linear (Figure 3-6), suggesting that the electron withdrawing nature of the ligands and thus the effective contact area factors into the activation energy for ET. To the best of our knowledge, a simple quantitative proxy for orbital overlap has

never before been correlated with observed rates of electron self-exchange, though orbital overlap has previously been invoked to explain the difference in self-exchange rate constants for the ferrocene/ferrocenium ($Fc^{0/+}$) and cobaltocene/cobaltocenium ($Cc^{0/+}$) couples.[15] In short, the Fc orbital in question is iron-based, whereas in Cc the orbital is spread over more of the molecule.

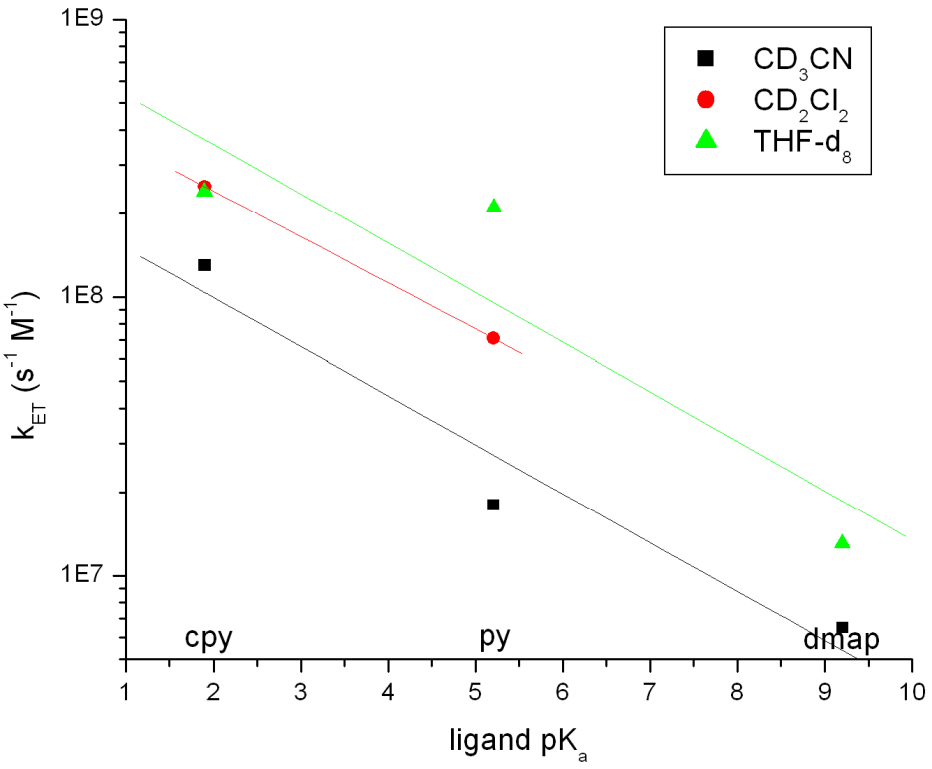

Figure 3-6. Plot of k_{ET} (s^{-1} M^{-1}) vs. ligand pK_a with linear fits. The linear relationship indicates that pK_a is a good proxy for the amount of electron density on the pyridine ligand in the reduced state and thus the donor acceptor orbital overlap, which figures into the activation barrier to ET.

It is unlikely that nuclear reorganization factors and inner shell barriers play large roles in determining the differences in rate constants for **1**-**3**. The shift in ν(CO) stretching frequency is about the same (~40 cm^{-1}) upon reduction of each cluster, suggesting that the inner sphere reorganization energies are comparable. We use the shift in ν(CO) here not as a direct marker for low frequency modes that make up the reorganization barrier, only for what it is: the best infrared probe of electronic redistribution in the cluster. The pre-exponential frequency factor ν_n is not likely

important either, as pyridine skeletal modes change by less than 1.5% from 4-cyanopyridine to 4-(dimethylamino)pyridine. Cluster skeletal modes in the vicinity of the point of substitution are expected to change by no more than this, and a change in the pre-exponential of a few percent cannot explain observed rate constants differing by more than an order of magnitude. Monoanionic pyrazine bridged dimers of these clusters exhibit picosecond ground state ET, and the reorganization energy, λ, for the pair of exchanging clusters has been estimated at 1.25 eV, or 10000 cm^{-1}.[7, 19] The intermolecular electron transfer studied here must be in the adiabatic regime with H_{AB} on the order of 10 to 20% of the reorganization energy λ to achieve the observed rates on the order of 10^8 s^{-1}. While low frequency skeletal modes and local solvent modes are expected to contribute to lamda,[20] there is no spectroscopic evidence to support this as the main factor in determining rate constants, nor any reason why these modes should make the barrier for **3** so much larger than for **1** that k_{ET} is more than an order of magnitude slower. Essentially, the clear evidence of significant and increasing unpaired electron spin density on the peripheral pyridine ligands of the anions of **1**, **2**, and **3** as the rate of ET increases (Figure 3-5), combined with the fact that replacing one of the pyridine ligands with a bridging pyrazine produces strongly delocalized mixed valence ions,[5] provides a consistent physical model for explaining rates of ET in both systems.

With respect to outer sphere thermodynamic solvent parameters, **1**-**3** behave normally. A log plot of k_{ET} vs. the solvent variable portion of the outer sphere reorganization energy[7] $(1/\varepsilon_{op} - 1/\varepsilon_s)$ shows that self-exchange is slower with increasing outer sphere solvent reorganization energy (Figure 3-7). The observed rate constants also correlate well with solvent microscopic polarities[7] (Figure 3-8). Here the reaction slows with increasing E_T.

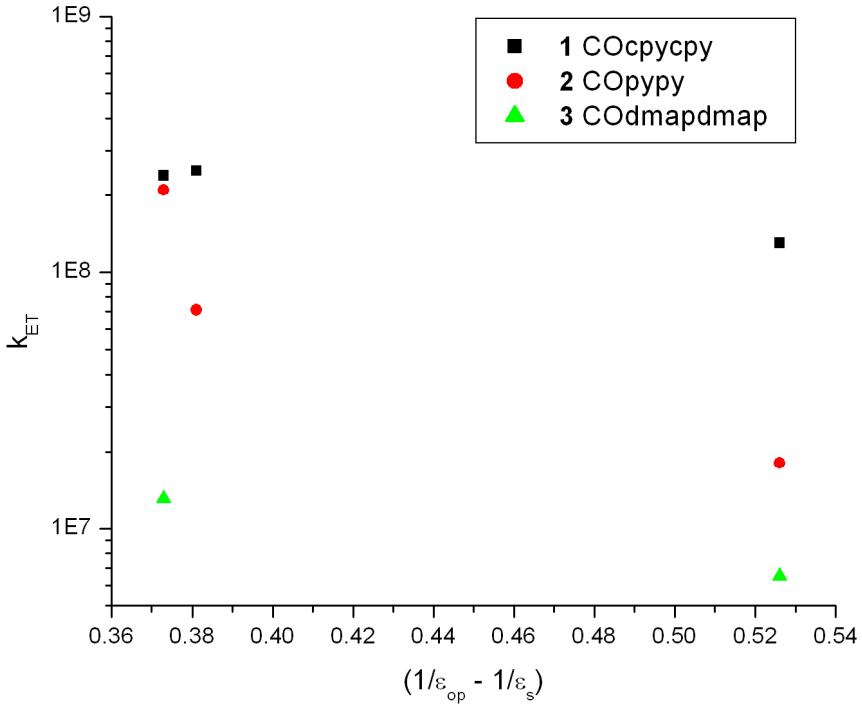

Figure 3-7. Plot of k_{ET} (s^{-1} M^{-1}) vs. $(1/\varepsilon_{op} - 1/\varepsilon_{s})$. The rate constant decreases with increasing outer sphere solvent reorganization energy.

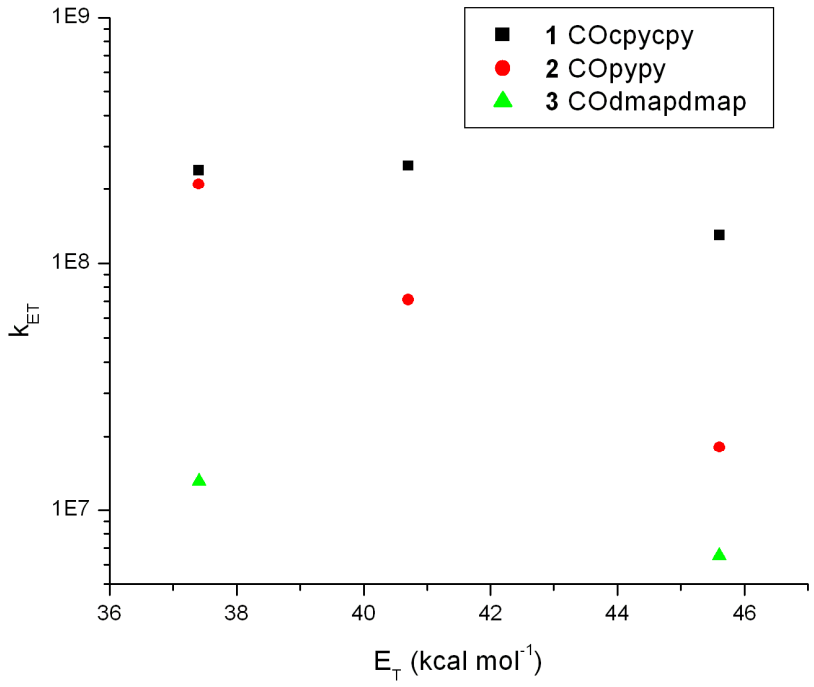

Figure 3-8. Plot of k_{ET} (s^{-1} M^{-1}) vs. solvent microscopic polarity.

3.3 Conclusions

The present results add to the quantitative understanding of electron self-exchange reactions. We were able to correlate the electron withdrawing ability of ancillary ligands to intermolecular electron transfer rate constants. A log plot of k_{ET} vs. the pyridine ligand pK_a is linear, suggesting that donor-acceptor orbital overlap is a major contributor to the ET activation barrier. A greater ^1H NMR contact shift for the pyridyl protons indicates increased electron density on ancillary pyridine ligands with more electron withdrawing groups. This leads to an increase in H_{AB}, the matrix element that describes the mixing of the two wavefunctions involved in electron exchange. The increased overlap decreases the activation energy for electron transfer.

This work also underscores the general importance of metal cluster orbital extension onto ligands. Often it is assumed that an oxidation state or a redox event is localized on a metal center or cluster. On the contrary, the delocalization of charge onto peripheral ligands is shown in this work to

play an important role in ET. The effect here is so strong that by simple variation of the pyridine ligands, rate constants can be varied by almost two orders of magnitude for a reaction with zero thermodynamic driving force.

Finally, the delocalization of the electron density onto the pyridine ligands illustrates how the $[Ru_3O(AcO)_6(CO)(L)_2]$ units contribute to such strongly interacting mixed valence ions when they are bridged by pyrazine.[21] Pyrazine is an even more effective electron withdrawing pyridyl ligand (pK ~ 1) than the three pyridines employed in this study. It would be expected then that delocalization onto the pyrazine bridge would be preferred, promoting electron transfer to the other Ru_3 cluster, and contributing to inter-cluster electron transfer and delocalization. This also helps explain why the fastest exchange times are observed for dimers with electron donating and aliphatic ancillary ligands, which do not have low lying π^* orbitals to accept electron density from the reduced cluster in the ancillary positions.[22]

3.4 Experimental

Preparation and Purification of Chemicals. The complexes **1**, $[Ru_3O(OAc)_6(CO)(cpy)_2]$, **2**, $[Ru_3O(OAc)_6(CO)(py)_2]$, and **3**, $[Ru_3O(OAc)_6(CO)(dmap)_2]$ were isolated as byproducts during previously reported preparations.[23] CD_3CN (D, 99.8%) and CD_2Cl_2 (D, 99.9%) were obtained from Cambridge Isotope Labs (CIL) and distilled under argon from calcium hydride before use. THF-d_8 (D, 99.5%) was obtained from CIL in ampoules and used as received. Decamethylcobaltocene was obtained from Aldrich, stored at -20 °C in a glove box, and used without purification.

Sample Preparation. Samples for NMR and IR experiments were prepared in a nitrogen-filled glove box. 7.0 mM solutions were prepared in the appropriate dried deuterated solvent, and approximately half of the solution was added to a small excess (1.2 – 1.5 equiv.) of decamethylcobaltocene. The reduced sample was filtered through glass wool to remove small amounts of impurities from the reductant. The fully oxidized and reduced solutions were mixed in varying proportions to prepare samples for NMR. 0.6 mL was added to either J-Young tubes (800

MHz, Wilmad) or sealed standard tubes (500 MHz, Wilmad) with no difference in the spectra obtained. Samples for IR were injected into liquid IR cells with CaF_2 windows and ~0.5 mm Teflon spacers and sealed in the glove box. All samples were analyzed immediately, though CD_3CN and THF solutions were stable for days unless opened to atmosphere. Singly reduced **3** was unstable in CD_2Cl_2, degrading in less than one minute.

NMR data collection and analysis. ^1H spectra were collected on a JEOL 500 MHz NMR and analyzed using JEOL Delta software. 64 scans of 131072 data points (0.15 Hz resolution) were collected from 25 to -15 ppm. Peak positions were used to determine the ratio of oxidized to reduced sample after a linear relationship was confirmed by infrared measurements, as described below. Peak widths at half height were measured in Delta. Each reported rate constant is an average of at least four values calculated from Equation 1. All spectra were recorded at the ambient temperature of the instrument (18 – 20 °C).

Infrared data collection and analysis. Infrared spectra were collected on a Bruker Equinox 55 FTIR spectrometer. After solvent subtraction, CO peaks were fit to mixed Gaussian/Lorentzian lineshapes using Bruker OPUS software. Suitably enlarged printouts were cut along the peak fit lines and weighed to give ratios of oxidized to reduced species.

Electrochemical measurements. Electrochemistry was performed on a BAS CV-50W in dried degassed CH_2Cl_2 with 0.1 M tetrabutylammonium hexafluorophosphate (TBAH, recrystallized from MeOH and dried under vacuum at 80 °C) and ~5 mM sample at a scan rate of 100 mV/s in a dedicated glovebox. The working electrode was a glassy carbon disk (0.3 cm diameter), the counter electrode was a platinum wire, and the reference was ferrocene/ferrocenium.

Note: Much of the material for this chapter comes directly from a manuscript entitled “Rates of electron self-exchange between oxo-centered ruthenium clusters are determined by orbital overlap” by John C. Goeltz, Christina J. Hanson, and Clifford P. Kubiak, which has been published in *Inorganic Chemistry*, **2009**, *48*, 4763-4767. http://dx.doi.org/10.1021/ic8022024 The dissertation author is the primary author of this manuscript.

3.5 References

1. Hush, N. S., *Prog. Inorg. Chem.* **1967,** *8*, 391.

2. Marcus, R. A., *Annu. Rev. Phys. Chem.* **1964,** *15*, 155.

3. Stanbury, D. M., *Nuclear factors in main-group electron transfer reactions*. 1997; Vol. 253, p 165-182.

4. Nelsen, S. F.; Ismagilov, R. F.; Gentile, K. E.; Nagy, M. A.; Tran, H. Q.; Qu, Q. L.; Halfen, D. T.; Odegard, A. L.; Pladziewicz, J. R., *J. Am. Chem. Soc.* **1998,** *120*, 8230-8240.

5. Ito, T.; Hamaguchi, T.; Nagino, H.; Yamaguchi, T.; Kido, H.; Zavarine, I. S.; Richmond, T.; Washington, J.; Kubiak, C. P., *J. Am. Chem. Soc.* **1999,** *121*, 4625-4632.

6. Ito, T.; Hamaguchi, T.; Nagino, H.; Yamaguchi, T.; Washington, J.; Kubiak, C. P., *Science (USA)* **1997,** *277*, 660-3.

7. Lear, B. J.; Glover, S. D.; Salsman, J. C.; Londergan, C. H.; Kubiak, C. P., *J. Am. Chem. Soc.* **2007,** *129*, 12772-12779.

8. Londergan, C. H.; Kubiak, C. P., *Chem. Eur. J.* **2003,** *9*, 5962-5969.

9. Salsman, J. C.; Kubiak, C. P.; Ito, T., *J. Am. Chem. Soc.* **2005,** *127*, 2382-2383.

10. Londergan, C. H.; Salsman, J. C.; Ronco, S.; Dolkas, L. M.; Kubiak, C. P., *J. Am. Chem. Soc.* **2002,** *124*, 6236-6237.

11. Rocha, R. C.; Brown, M. G.; Londergan, C. H.; Salsman, J. C.; Kubiak, C. P.; Shreve, A. P., *J. Phys. Chem. A.* **2005,** *109*, 9006-9012.

12. Chan, M.-S.; DeRoos, J. B.; Wahl, A. C., *J. Phys. Chem.* **1973,** *77*, 2163-2165.

13. Coddington, J.; Wherland, S., *Inorg. Chem.* **1997,** *36*, 6235-6237.

14. Walsh, J. L.; Baumann, J. A.; Meyer, T. J., *Inorg. Chem.* **1980,** *19*, 2145-2151.

15. Nielson, R. M.; Golovin, M. N.; McManis, G. E.; Weaver, M. J., *J. Am. Chem. Soc.* **1988,** *110*, 1745-1749.

16. Nielson, R. M.; McManis, G. E.; Golovin, M. N.; Weaver, M. J., *J. Phys. Chem.* **1988,** *92*, 3441-3450.

17. Kowert, B. A.; Fehr, M. J.; Sheaff, P. J., *Inorg. Chem.* **2008,** *47*, 5696-5701.

18. Yang, E. S.; Chan, M. S.; Wahl, A. C., *J. Phys. Chem.* **1975,** *79*, 2049-2052.

19. Londergan, C. H.; Salsman, J. C.; Lear, B. J.; Kubiak, C. P., *Chem. Phys.* **2006,** *324*, 57-62.

20. Endicott, J. F.; Uddin, M. J., *Coord. Chem. Rev.* **2001,** *219*, 687-712.

21. Salsman, J. C.; Ronco, S.; Londergan, C. H.; Kubiak, C. P., *Inorg. Chem.* **2006,** *45*, 547-554.

22. Yamaguchi, T.; Imai, N.; Ito, T.; Kubiak, C. P., *Bull. Chem. Soc. Jpn.* **2000,** *73*, 1205-1212.

23. Ota, K.; Sasaki, H.; Matsui, T.; Hamaguchi, T.; Yamaguchi, T.; Ito, T.; Kido, H.; Kubiak, C. P., *Inorg. Chem.* **1999,** *38*, 4070-4078.

Chapter 4

Electronic structural effects in self-exchange reactions

4.1 Introduction

Electron self-exchange between oxo-centered ruthenium clusters of the type $[Ru_3O(OAc)_6(L)_3]$ has been studied for both covalently bridged intramolecular mixed valence exchange[1] and freely diffusing intermolecular exchange.[2] Pioneering work by Meyer *et al.* set out to understand the intermolecular +/0 couple to better explain electronic communication evident in the voltammetric behavior and electronic spectra of cationic mixed valence clusters bridged by pyrazine.[2-5] The previous chapter details[6] studies of intermolecular self-exchange between the neutral and anionic clusters $[Ru_3O(OAc)_6(CO)(L)_2]^{0/-}$ performed to elucidate details of exchange in highly coupled anionic mixed valence complexes bridged by pyrazine.[7-14] The electronic distributions of reduced complexes $\mathbf{1}^-$-$\mathbf{3}^-$ (Figure 4-1), specifically on the pyridyl ligands, were found to be critically important in determining the coupling and the rate of electron transfer.

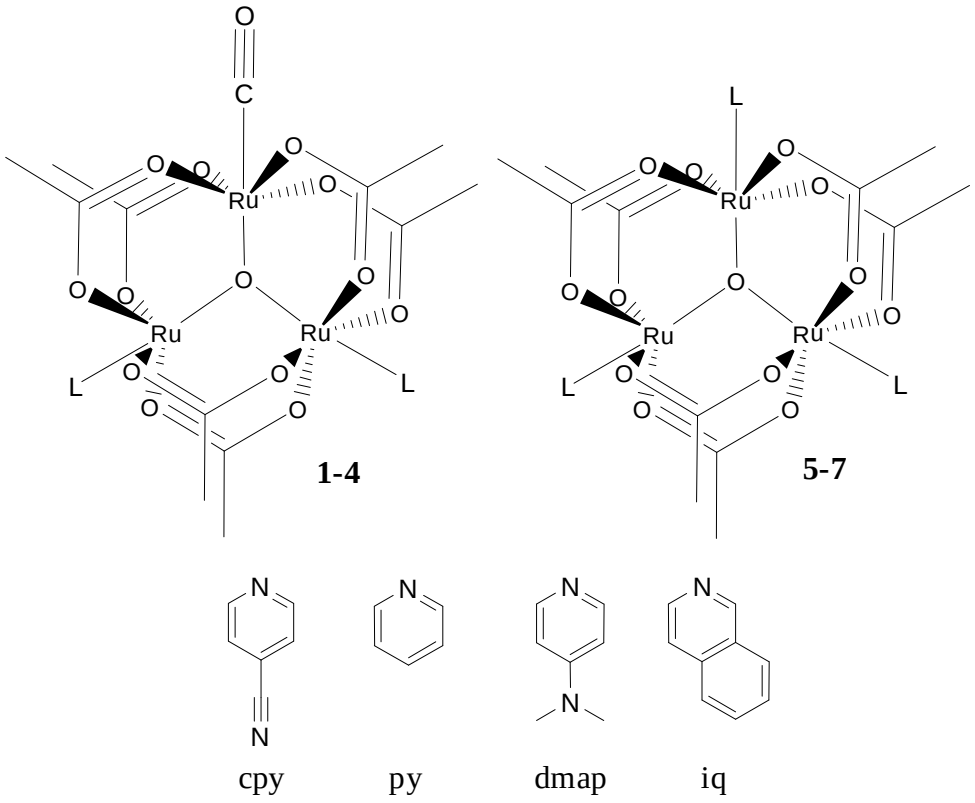

Figure 4-1. The seven clusters discussed in this chapter: **1** and **5**, L = 4-cyanopyridine (cpy); **2** and **6**, L = pyridine (py); **3** and **7**, L = 4-(dimethyl)aminopyridine (dmap); **4**, L = isoquinoline (iq).

In this chapter we explore further electronic structural effects in self-exchange reactions of oxo-centered triruthenium clusters, and compare the 0/- couple for the $[Ru_3O(OAc)_6(CO)(L)_2]$ series **1-4** and the +/0 couple for $[Ru_3O(OAc)_6(L)_3]$ series **5-7**.[15]

4.2 Overview of results

The kinetics of electron self-exchange for the $[Ru_3O(OAc)_6(CO)(L)_2]^{0/-}$ pairs for complexes **1-3** where L = 4-cyanopyridine (cpy), pyridine (py), and 4-(dimethylamino)pyridine (dmap) are described in Chapter 3.[6] Those data and the new rate constants reported here for complexes **4-7** were all determined by standard NMR line broadening experiments. Rate constants were calculated using equation 1,

$$k_{ET} = \frac{4\pi\chi_d\chi_p(\Delta\nu)^2}{(W_{dp} - \chi_p W_p - \chi_d W_d)C_{tot}} \quad (1)$$

where χ_d and χ_p are the mole fractions of diamagnetic and paramagnetic species, $\Delta\nu$ is the difference in chemical shift between diamagnetic and paramagnetic species in Hz, W_{dp} is the peak width at half maximum for the mixture in question, W_d and W_p are the widths for the pure diamagnetic and paramagnetic species, and C_{tot} is the total concentration in mol L^{-1}.[16] Equation 1 holds for this study because the exchange was in the fast regime (where $k_{ET}(C_{tot}) >> 2\pi(\Delta\nu)$ on the NMR timescale, as the chemical shifts for exchanging species were averages of the diamagnetic and paramagnetic chemical shifts, weighted by their respective mole fractions.[2, 6] Rate constants with estimated standard deviations are reported in Table 4-1 and plotted logarithmically against pyridine ligand pK_a[17] in Figure 4-2.

Table 4-1. Electron transfer rate constants (x 10^7 s^{-1} M^{-1}) with ESDs in parentheses and pK_a values for pyridine ligand conjugate acids.

complex	CD_3CN	CD_2Cl_2	ligand pK_a
1 $CO(cpy)_2^{0/-}$	13(3)		1.9
2 $CO(py)_2^{0/-}$	1.8(5)		5.1
3 $CO(dmap)_2^{0/-}$	0.7(5)		9.2
4 $CO(iq)_2^{0/-}$	5(2)		5.1
5 $(cpy)_3^{+/0}$		3.3(3)	1.9
6 $(py)_3^{+/0}$		11(1)	5.1
7 $(dmap)_3^{+/0}$		7.2(5)	9.2

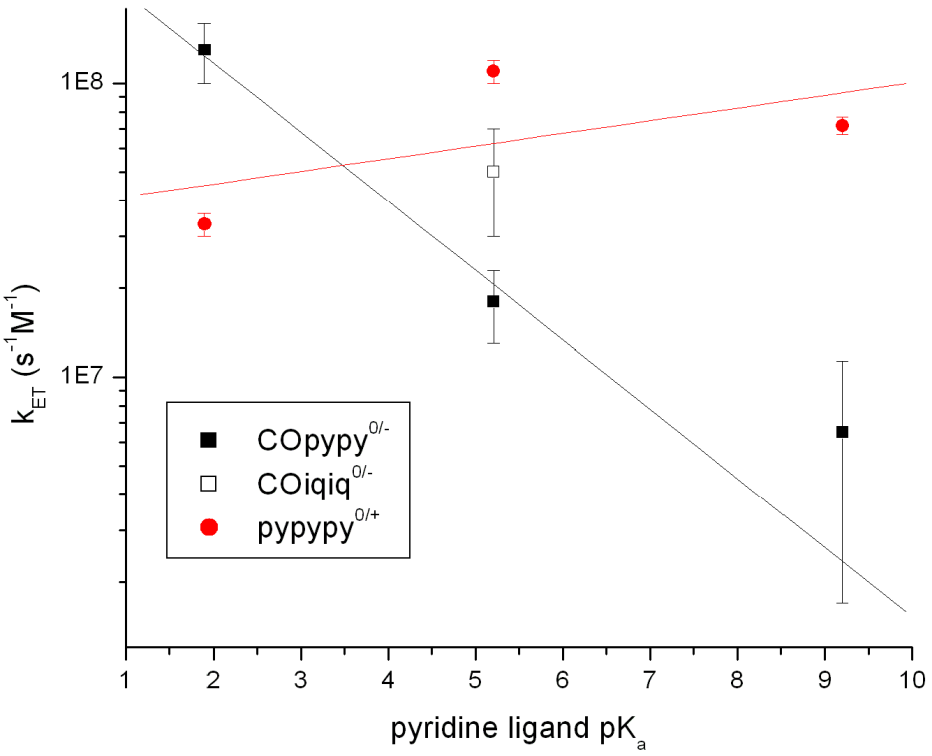

Figure 4-2. Log plot of ET rate constants vs. pyridine ligand pK_a with estimated standard deviations.

4.3 Electron self-exchange in the $[Ru_3O(OAc)_6(CO)(L)_2]^{0/-}$ system: orbital overlap determines the rate constant

First, we will consider the 0/- couple in complexes **1-4**. In our previous study of self-exchange, we found that the electronic distribution determined k_{ET} for $[Ru_3O(OAc)_6(CO)(L)_2]^{0/-}$ couples where L was a pyridine ligand, complexes **1-3**.[6] More electron withdrawing substituents on the pyridine ligands led to significantly faster self-exchange. A greater paramagnetic ^1H contact shift was also observed for pyridyl protons in reduced complexes with more electron withdrawing substituents, indicating greater electron spin density on the peripheral ligands. A log plot of rate constant vs. pyridine pK_a was nearly linear (black squares, Figure 4-2). This suggests that the

dominant effect of the electron withdrawing nature of the pyridine ligands can be found in the exponential term of the standard adiabatic Marcus-Hush formalism, equation 2.[18-19]

$$k_{ET} = \kappa\nu \exp \frac{\frac{\lambda}{4} - H_{AB} + \frac{H_{AB}^{\ 2}}{\lambda}}{RT} \qquad (2)$$

Also of note is that the reorganization energies typically observed for the pair of exchanging clusters in the 0/- couple are on the order of 10000 cm^{-1}.[10] H_{AB} need only be a few percent of λ to achieve adiabaticity[20] and make equation 2 applicable here, but this is still a respectable coupling given the large reorganization energy. In this case we forego the more commonly invoked explanation where low frequency vibrational modes describe the kinetic barrier[21-22] in favor of a Wolfsburg-Helmholtz-Mulliken approximation[23] in which orbital overlap, S_{AB}, is used as a proxy for electron exchange, H_{AB}. The good logarithmic correlation between k_{ET} and ligand pK_a is consistent with an orbital overlap description, but the paramagnetic contact shifts on the peripheral ligands (Figure 4-3) give the clearest indication that increased spin density is extended to the more electron withdrawing peripheral pyridine ligands.

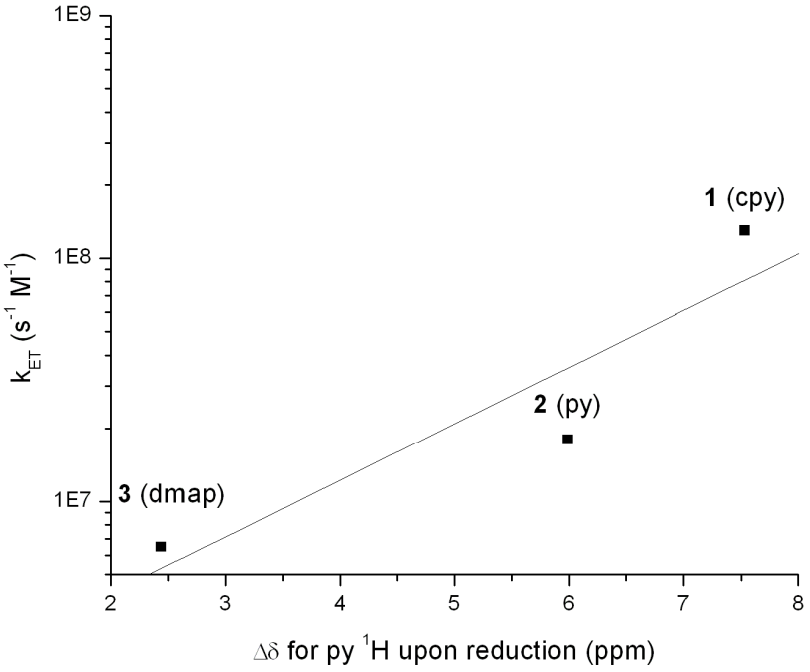

Figure 4-3. Log plot of ET rate constants vs. average paramagnetic contact shift (Δδ) for pyridine ligand protons upon reduction in CD_3CN.

To obtain further evidence for donor-acceptor overlap as the rate determining factor in the 0/- couple, we synthesized complex **4**. In **4**, L = isoquinoline (iq), a pyridine type ligand with an extended π structure (see Figure 4-1). Remarkably, the conjugate acids of py and iq both have a reported pK_a of 5.1.[17] As might then be expected, the electrochemistry of these two $[Ru_3O(OAc)_6(CO)(L)_2]$ clusters each show three couples with the same $E_{1/2}$, within 10 mV, as seen in Figure 4-4.

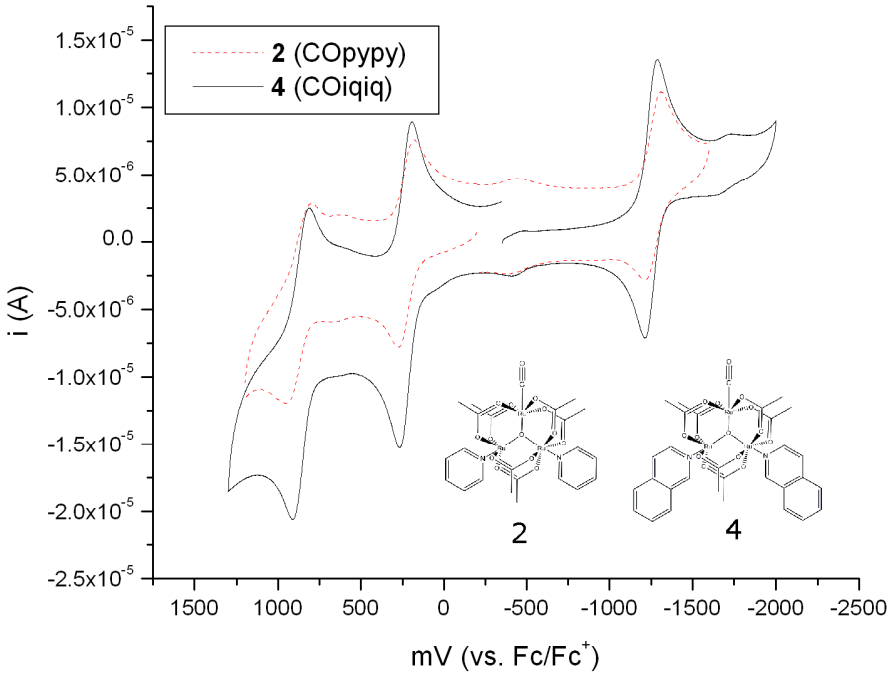

Figure 4-4. Electrochemistry for complexes **2** and **4**, ~1 mM in CH_2Cl_2 with 0.1 M Bu_4NPF_6

We were able to isolate single crystals of **4** suitable for X-ray diffraction studies. This is uncommon for $[Ru_3O(OAc)_6(CO)(L)_2]$ type complexes. An ORTEP drawing of **4** is shown in Figure 4-5. While the monoanionic decamethylcobaltocenium salt of $\mathbf{4}^-$ was readily prepared for NMR studies, single crystals were not obtained despite repeated attempts at crystallization, so a direct structural comparison and independent estimate of reorganization energy cannot be made at this time.

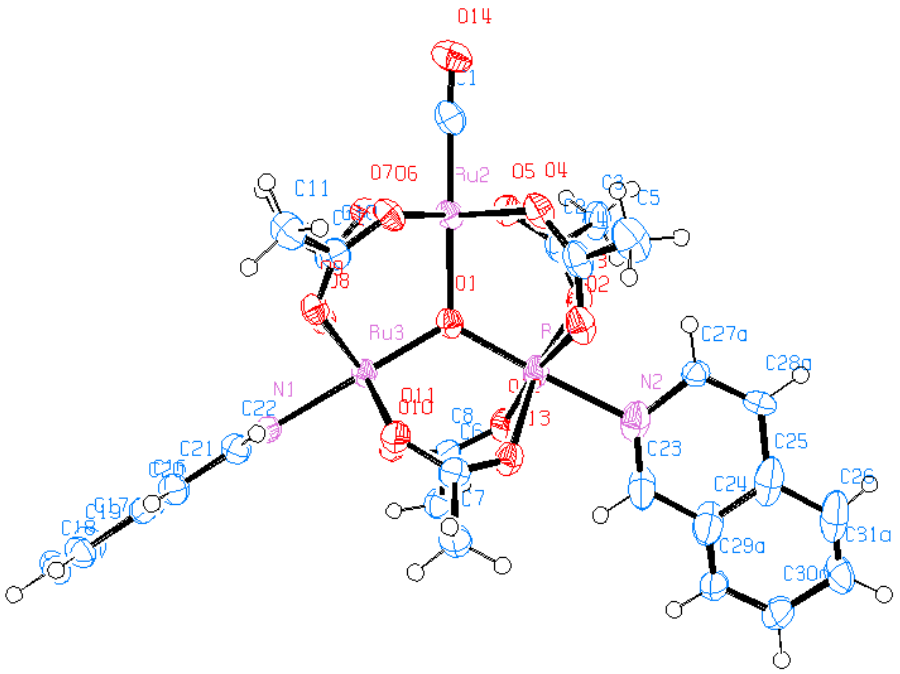

Figure 4-5. ORTEP (50% probability) plot of complex **4**. Only one of two angles for the out-of-plane isoquinoline ligand is shown.

In CD_3CN, k_{ET} for $\mathbf{4}^{0/-}$ was 5(2) x 10^7 $M^{-1}s^{-1}$, more than twice as fast as for $\mathbf{2}^{0/-}$, the $[Ru_3O(OAc)_6CO(py)_2]$ complex (see black and white squares at pK_a = 5.1 in Figure 1). This confirms that the donor-acceptor overlap is the dominant factor in determining the rate of exchange in neutral and reduced clusters $[\mathbf{1}\text{-}\mathbf{4}]^{0/-}$. It would appear that electron *density* (as in observed Fermi contact shifts) and electron *distribution* (in an areal or delocalization sense, as in extent of the π system) in the reduced species are both important. Studies are currently underway comparing pyrazine bridged systems with pyridine and isoquinoline ligands to determine the relative contributions of a larger π-system to rates of *intramolecular* ET in the respective mixed valence complexes, as in Figure 4-6. Preliminary results show that the electrochemical splittings, $\Delta E_{1/2}$, in

the cluster reductions of $\mathbf{8}^{0/-}$ and $\mathbf{9}^{0/-}$ are within 10 mV of each other, and the rate constants for intramolecular electron transfer k_{ET} are the same within the uncertainty of the ν(CO) bandshape spectral simulation. We conclude that the electronic properties of py and iq as ligands in these complexes are nearly identical. This has no influence on rates of intramolecular ET in a mixed valence ions such as $\mathbf{8}^-$ and $\mathbf{9}^-$, but all other things being about equal, the more extended π system of iq does promote faster rates of intermolecular ET by better overlap.

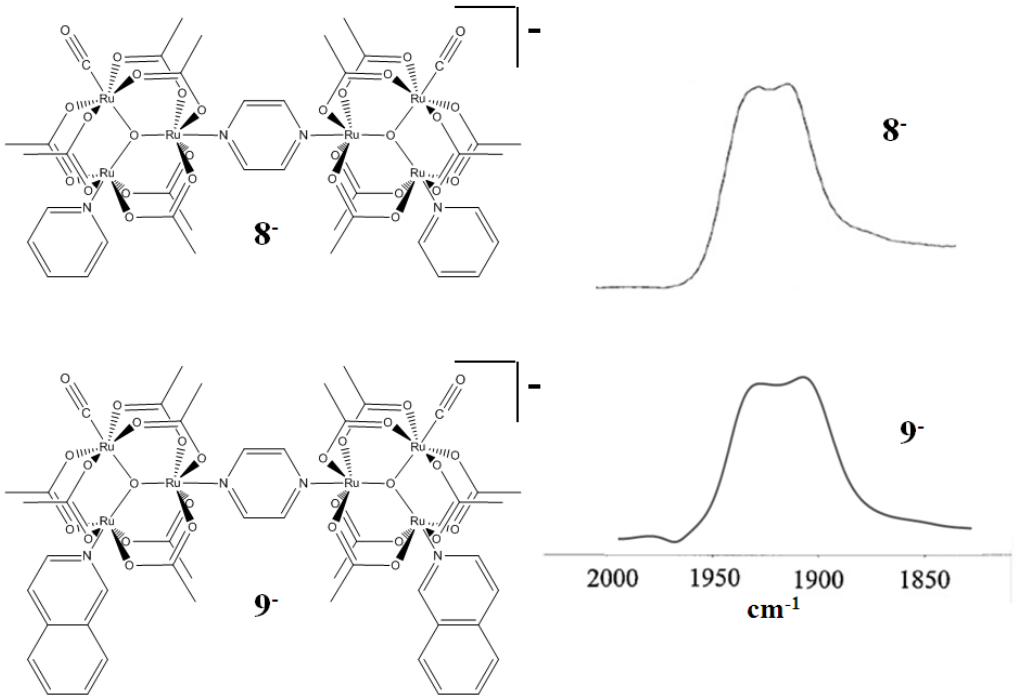

Figure 4-6. Structures of pyrazine bridged dimers with pyridyl (**8**) or isoquinoline (**9**) ligands, and infrared spectra of the ν(CO) region of singly reduced mixed valence $\mathbf{8}^-$ and $\mathbf{9}^-$, exhibiting comparable coalescence and thus comparable rates of intramolecular electron transfer.

4.4 Electron self-exchange in the $[Ru_3O(OAc)_6(py)_3]^{+/0}$ system: structural characterization of the missing side of the redox couple

We now turn to the +/0 couple in the threefold symmetric complexes **5-7**. We reproduced exactly Meyer *et al.*'s +/0 exchange rate constant for the tris-pyridyl complex **6**, and determined rates

for the tris-4-cyanopyridine complex **5** and tris-4-(dimethyl)aminopyridine complex **7**. As can be seen in Table 4-1 and Figure 4-2 (red circles), rate constants are in the same regime, but there is no visible correlation between pK_a and k_{ET}, despite a predictable dependence of the oxidation potentials on pK_a (as listed in the experimental section).

In spite of the availability of several X-ray crystal structures of Ru_3O complexes in the Cambridge Crystallographic Database, direct comparison of a single complex in two oxidation states was not possible until now. We were able to crystallize the cationic tris-pyridyl complex $\mathbf{6}^{+}PF_6^{-}$, for comparison with the known structure of neutral **6**.[24-25] An ORTEP plot of $\mathbf{6}^{+}PF_6^{-}$ is shown in Figure 4-7.

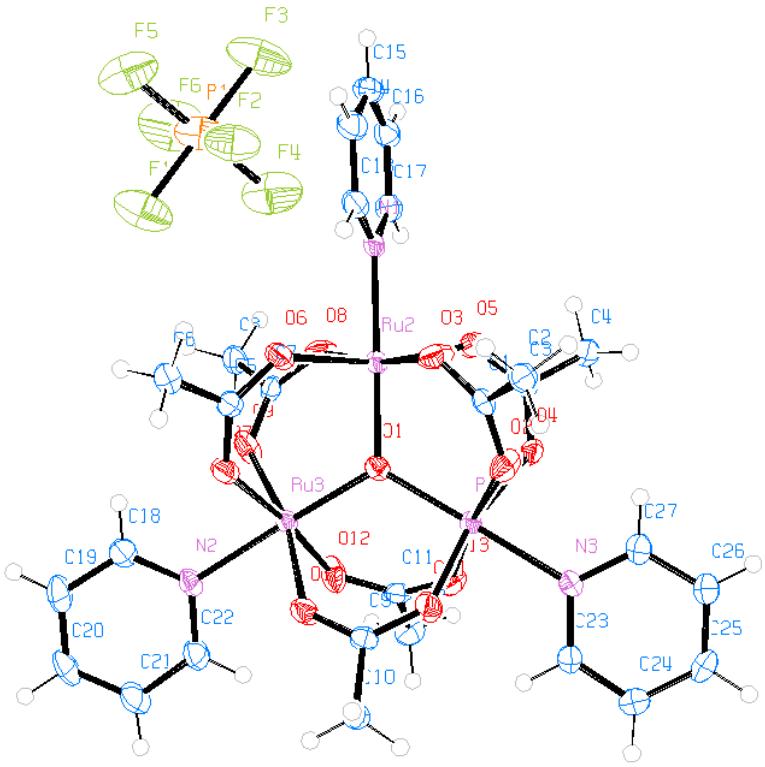

Figure 4-7. ORTEP (50% probability) plot of complex $\mathbf{6}^{+}PF_6^{-}$.

The solid state structure of $\mathbf{6}^{+}$ is remarkable only in that the 3-fold symmetry seen in the neutral (formally $Ru^{III}Ru^{III}Ru^{II}$) system is broken in the $Ru^{III}Ru^{III}Ru^{III}$ system, presumably by

counterion and packing effects. The rotation of pyridyl ligands is generally assumed to be free in solution, except in cases of electron delocalization onto the π^* system, and the structures reported here do not conflict with that notion.

The availability of structural data for both sides of the $[Ru_3O(OAc)_6(py)_3]^{+/0}$ couple provides the opportunity to estimate the inner sphere reorganization energy λ_{is} from first principles.[26-27] The inner sphere reorganization barrier λ_{is} is calculated to be 1520 cm^{-1} on the basis of the asymmetric Ru_3O (bridging oxo) mode, the Ru-N stretches, a pyridyl rocking mode, and an acetate-based Ru-O_4 mode.[26, 28-30] Given the complexity of mode mixing in cluster vibrations under 800 cm^{-1} the number should be considered an estimate, but as all significant bond distance changes have been taken into account, the order of magnitude is likely correct. For comparison, the ferrocene/ferrocenium couple has a λ_{is} of ~240 cm^{-1} calculated using only the metal ring breathing mode.

The estimated λ for the 0/- couple is 10000 cm^{-1} and includes outer sphere components, so for direct comparison λ_{os} must be added to the λ_{is} barrier calculated for the +/0 couple. The electron transfer distance is not known, but using reasonable values from crystal structures and the literature, the λ_{os} for $\mathbf{6}^{+/0}$ in methylene chloride is calculated to be between 1800 and 3600 cm^{-1} for these complexes.[26, 31] This puts the λ_{tot} for the +/0 pair at 3320-5120 cm^{-1}. Even if λ is ~5120 cm^{-1} for the +/0 couple, the λ of 10000 cm^{-1} is clearly larger for the 0/- couple, though measured self-exchange rate constants are in the same regime (10^7-10^8 $M^{-1}s^{-1}$). Taken together with the strong dependence on pyridine pK_a in the 0/- couple and complete lack thereof in the +/0 couple, a consistent framework emerges for understanding electron self-exchange in both couples, in both inter- and intramolecular Ru_3O couples. Orbital overlap determines the rate constant in neutral/anionic exchanges, and is not a determining factor in neutral/cationic exchanges. Rates are in the same regime because the effective barriers and crossing/frequency factors are similar after including the large coupling in the 0/- pairs. This is depicted graphically in Figure 4-8.

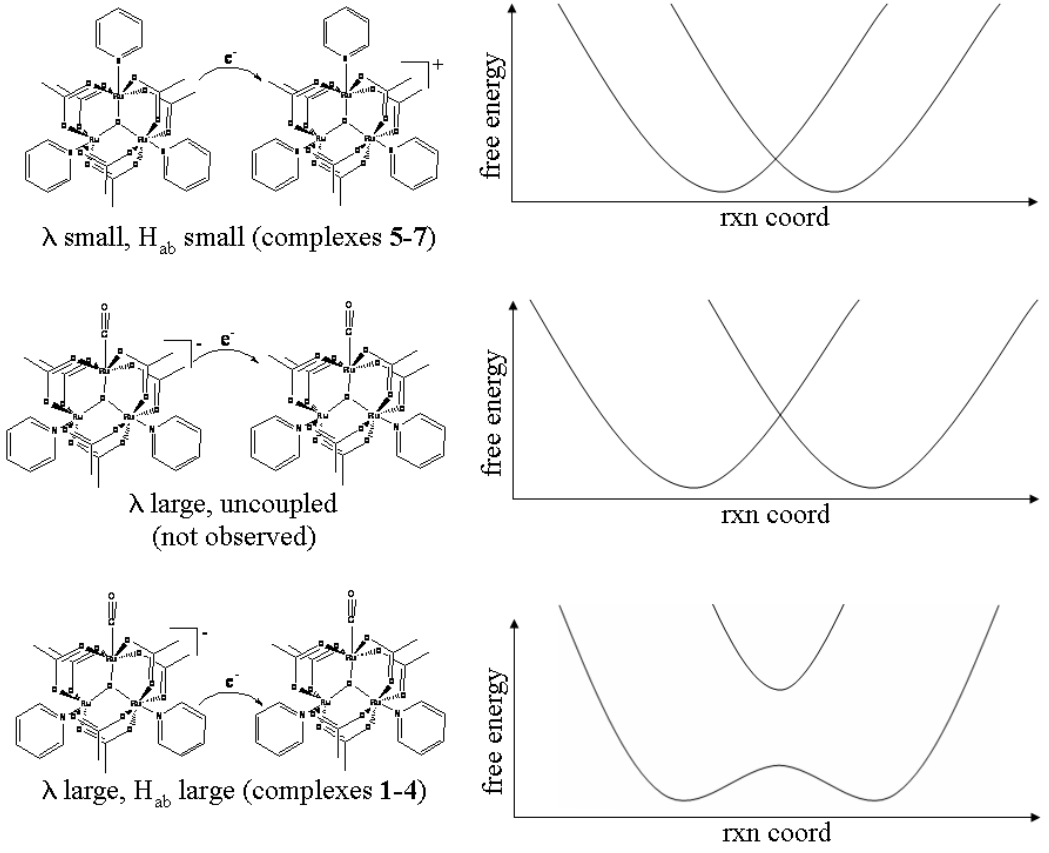

Figure 4-8. Qualitative depiction of energy surfaces for the +/0 couple (λ ~ 3320-5120 cm^{-1}, small coupling, top), 0/- couple in the absence of coupling (λ ~ 10000 cm^{-1}, small coupling, middle), and 0/- couple in the presence of coupling, as observed (λ ~ 10000 cm^{-1}, large coupling, bottom).

In any discussion of electron exchange it is necessary to examine closely the donor and acceptor orbitals. Qualitative molecular orbital diagrams (Figure 4-9) for D_{3h} symmetric clusters such as **5-7** have been invoked in several studies.[2-4, 32] It becomes clear that a +/0 pair of exchanging clusters would have a donor/acceptor orbital of A_2' symmetry. Delocalization of electron density onto the pyridyl π^* system would be symmetrically accessible if the donor/acceptor were of A_2'' symmetry, but A_2' does not allow for mixing beyond the metal orbitals. Indeed, there is no evidence in NMR spectra or kinetic trends to indicate that the pyridyl π* system is important in +/0 exchange.

On the other hand both NMR and kinetic data *do* demonstrate the importance of delocalization onto peripheral ligands in **1**-**4**$^{0/-}$, the $[Ru_3O(OAc)_6(CO)(L)_2]^{0/-}$ clusters. The A_2'' SOMO of **1**$^{-}$-**4**$^{-}$ is accessible to π* orbitals of pyridine ligands in the Ru_3O plane,[33] consistent with the experimental results. While the single carbonyl ligand lowers the overall symmetry of the complex slightly, the electronic structure analysis remains essentially the same.

Electronic structural effects explain the large difference observed in inner sphere reorganization energies for the +/0 and 0/- pairs (given that the outer sphere components will be comparable in a given solvent). A change in electronic occupancy in an orbital localized on the three ruthenium atoms is likely to induce small structural changes as compared with a change in occupancy for an orbital delocalized over the three ruthenium atoms and two or three pyridine π* systems. We continue to attempt the isolation of XRD quality single crystals of **1**-**4**$^{-}$ and are confident that structural data will validate the arguments made here.

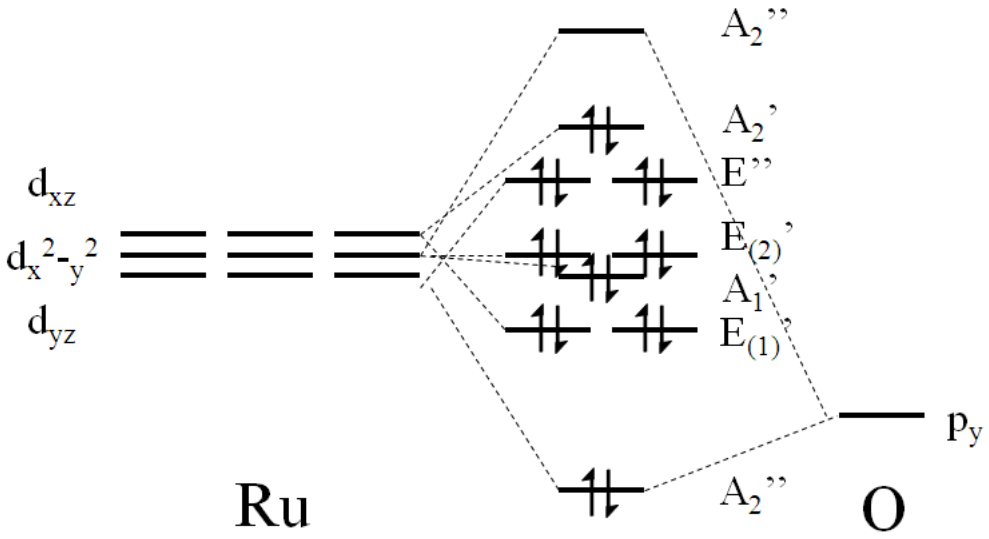

Figure 4-9. Qualitative MO scheme for cluster π system in D_{3h} symmetry for the neutral clusters **5**-**7**.

4.5 Calculation of ΔG^*_{is} for $[Ru_3O(OAc)_6(py)_3]^{+/0}$

The inner sphere reorganization energy for $\mathbf{6}^{0/+}$ couple was calculated using structural and vibrational data and methods from Sutin, N. *Prog. Inorg. Chem.* **1983,** *30,* 441 and Nielson et al. *J. Am. Chem. Soc*. **1988,** *110,* 1745-1749.

The inner sphere reorganization barrier is given by

$$\Delta G^*_{is} = 0.5 n f_{is}{}^{r} (\Delta a / 2)^2 \quad (3)$$

where n is the number of bonds undergoing distortion (including *both* molecules in the couple), Δa is the change in bond distance between the oxidized and reduced forms (in meters), and f_{is}^{r} is the "reduced" force constant for each bond (in g s^{-2} mol^{-1}) obtained from the individual force constants for the reduced and oxidized species using

$$f_{is}{}^{r} = 2 f_{is}{}^{ox} f_{is}{}^{red} / (f_{is}{}^{ox} + f_{is}{}^{red}) \quad (4)$$

and

$$f_{is} = 4\pi^2 \nu_{is}{}^{2} \mu \quad (5)$$

where ν_{is} is the frequency in s^{-1} and μ is the reduced mass in g mol^{-1}.[26]

First we will reproduce the calculation from Nielson *et al.* for ferrocene.[30] The only mode analyzed is the Cp ring breathing mode, with a Δa of 0.035 Å and Raman frequencies of 310 and 315 cm^{-1} for ferrocene and ferrocenium, respectively. The reduced mass of the two rings breathing with respect to the metal center is taken to be the mass of a single ring, and n = 2 because only one "bond" (ring-ring distance) is undergoing this change for the exchanging *pair*. (For example, n=12 for breathing modes of a pair of exchanging octahedral complexes.)[26]

f_{is}^{ox} = 4 * $(3.14)^2$ * (9.294 E12 s^{-1})^2 (65 g mol^{-1}) = 2.2166 E29 g mol^{-1} s^{-2}

f_{is}^{red} = 2.2882 E29 g mol^{-1} s^{-2}

The reduced force constant is then

f_{is}^{r} = 2.2518 E29 g mol^{-1} s^{-2} (or dyn mol^{-1} cm^{-1}, or 3.75 E5 dyn cm^{-1}, as reported.[30])

ΔG_{is}^{*} = 0.5 * 2 * 2.2518 E29 g mol^{-1} s^{-2} * (0.035 E-10 m / 2)^2 = 7.0 E5 g m^2 $s^{-2}$$mol^{-1}$

ΔG_{is}^{*} = 7.0 E2 kg m^2 s^{-2} mol^{-1} = 7.0 E2 J mol^{-1}

ΔG_{is}^{*} = 0.70 kJ mol^{-1} (60 cm^{-1}) for the Fc^{+}/Fc pair.

Nielson et al. report a value of 0.35 kcal mol^{-1}.[30] The use of kcal instead of kJ is likely just a typographic error, though it is propagated throughout the manuscript. The authors likely used n = 1 (i.e. one metallocene) where n = 2 is appropriate, as in Sutin's example of n = 12 for metal ligand bonds in exchanging octahedral complexes. Fortunately this error did not perturb any further quantitative analysis on their part, at least in that manuscript.

With increased confidence we turn to the basic ruthenium acetate clusters. Low energy modes will dominate ΔG_{is}^{*}, and complete assignment of low energy vibrations of tris-pyridyl ruthenium clusters is currently unavailable. Values used here are estimated from available data on pyrazine bridged clusters with CO and pyridyl ligands[29] and available data for $Fe_3O(py)_3$ clusters.[34]

Ru-N distortions

The Raman spectrum of the pyrazine bridged dmap dimer has a Ru-N stretch of 210 cm^{-1}. $Fe_3O(py)_3$ has Fe-N bands at 186 and 253 cm^{-1} for the neutral and cationic forms. This analysis will use 210 and 277 cm^{-1}, or 6.295 E12 s^{-1} and 8.304 E12 s^{-1}.

$f_{is}^{ox} = 4 * (3.14)^2 * (8.304\ E12\ s^{-1})^2\ (12.3g\ mol^{-1}) = 3.3450\ E28\ g\ mol^{-1}\ s^{-2}$

$f_{is}^{red} = 1.9246\ E28\ g\ mol^{-1}\ s^{-2}$

$f_{is}^{r} = 2.4434\ E28\ g\ mol^{-1}\ s^{-2}$

$\Delta G_{is}^{*} = 0.5 * 2 * 2.4434\ E28\ g\ mol^{-1}\ s^{-2} * (\Delta a / 2)^2\ m^2$

Δa = 0.022, 0.016, and 0.004 Å for three different changes in bond distance

$\Delta G_{is}^{*} = 2.96\ E4 + 1.56\ E4 + 9.78\ E2\ g\ m^2\ s^{-2}\ mol^{-1}$

$\Delta G_{is\ Ru\text{-}N}^{*} = 0.046$ kJ mol^{-1} or 4 cm^{-1}

Ru_3O distortions

Neither crystal structure shows significant deviation from planarity for the central oxygen, so any δ_{sym} modes below 400 cm^{-1} should not contribute significantly to the inner sphere barrier. The A_1 component of the $\nu_{as}(Ru_3O)$ mode is observed at 584 cm^{-1} in the (CO)(dmap) pyrazine bridged

dimers and at 600 and 570 cm^{-1} in oxidized and neutral $Fe_3O(py)_3$ clusters, so 614 and 584 cm^{-1} will be used here.

$f_{is}^{ox} = 4 * (3.14)^2 * (18.407\ E12\ s^{-1})^2\ (13.8\ g\ mol^{-1}) = 1.846\ E29\ g\ mol^{-1}\ s^{-2}$

$f_{is}^{red} = 1.670\ E29\ g\ mol^{-1}\ s^{-2}$

$f_{is}^{r} = 1.754\ E29\ g\ mol^{-1}\ s^{-2}$

$\Delta G_{is}^{*} = 0.5 * 2 * 1.754\ E29\ g\ mol^{-1}\ s^{-2} * (\Delta a / 2)^2\ m^2$

Δa = 0.023, 0.019, and 0.011 Å for three different changes in bond distance

$\Delta G_{is}^{*} = 2.32\ E5 + 1.58\ E5 + 5.31\ E4\ g\ m^2\ s^{-2}\ mol^{-1}$

$\Delta G_{is\ Ru3O}^{*} = 0.443\ kJ\ mol^{-1}$ or $37\ cm^{-1}$

Ru-O_4:

The ruthenium-oxygen acetate bonds are difficult to analyze because they have many vibrational modes. Here we will use 315 and 345 cm^{-1}.[34-35]

$f_{is}^{ox} = 4 * (3.14)^2 * (10.343\ E12\ s^{-1})^2\ (13.8\ g\ mol^{-1}) = 5.828\ E28\ g\ mol^{-1}\ s^{-2}$

$f_{is}^{red} = 4.858\ E28\ g\ mol^{-1}\ s^{-2}$

$f_{is}^{r} = 5.299\ E28\ g\ mol^{-1}\ s^{-2}$

$\Delta G_{is}^{*} = 0.5 * 2 * 5.299\ E28\ g\ mol^{-1}\ s^{-2} * (\Delta a / 2)^2\ m^2$

Δa = 0.030, 0.033, 0.038, 0.034, 0.043, 0.036, 0.038, 0.036, 0.035, 0.028, 0.025, and 0.016 Å

$\Delta G_{is\ Ru\text{-}O4}^{*} = 1.77\ kJ\ mol^{-1}$ or $148\ cm^{-1}$

Pyridine distortions

Though the choice is arbitrary and mode mixing probably complicates the actual calculation to a degree well beyond the scope of this work, the lowest frequency pyridyl mode with significant bond distance changes assigned for $M_3O(py)_3$ clusters is mode 6a. The energies are 639 and 629 cm^{-1} for oxidized and reduced iron clusters, so those numbers are used here.

f_{is}^{ox} C-C $= 4 * (3.14)^2 * (19.157\ E12\ s^{-1})^2\ (6\ g\ mol^{-1}) = 8.693\ E28\ g\ mol^{-1}\ s^{-2}$

f_{is}^{red} C-C = 8.423 E28 g mol^{-1} s^{-2}

f_{is}^{ox} C-N = 9.359 E28 g mol^{-1} s^{-2}

f_{is}^{red} C-N = 9.069 E28 g mol^{-1} s^{-2}

f_{is}^{r} C-C = 8.556 E28 g mol^{-1} s^{-2}

f_{is}^{r} C-N = 9.212 E28 g mol^{-1} s^{-2}

$\Delta G_{is}^{*} = 0.5 * 2 * f_{is}^{r}$ g mol^{-1} s^{-2} * $(\Delta a / 2)^2$ m^2

$\Delta G_{is\ py}^{*}$ = 2.27 kJ mol^{-1} or 190 cm^{-1}

The total ΔG_{is}^{*} estimated here is 4.53 kJ mol^{-1}, or 380 cm^{-1}. This should of course be taken as an estimate, but is still instructive as to the order of magnitude of the inner sphere reorganization barrier. Mode mixing and a large numbers of bond distance changes and vibrational modes make this calculation more susceptible to propagated error than the single vibration used to calculate the inner sphere reorganization energy for metallocene couples. Nonetheless, a vibrational mode in the right order of magnitude was used with appropriate reduced masses for $Ru_3O(OAc)_6(py)_3$ clusters with crystallographically determined bond distances.

The outer sphere component ΔG_{os}^{*} is estimated at 450-900 cm^{-1} in CD_2Cl_2 by substituting the optical and static dielectric constants for CH_2Cl_2 from Gennett *et al.*[31] into the formula set up by Sutin for $Fe(H_2O)_6^{3+/2+}$ exchange in water,[26] and using an estimated radius of 6 angstroms and reasonable possible electron transfer distances of 8-12 angstroms taken from space filling models of the crystal structure of **6**$^{+}$ reported in this paper. Obviously the ruthenium clusters used in our study are not spheres, but the uncertainty in determining *r* for delocalized molecular orbitals constructed from 3 ruthenium atoms and an oxygen atom outweighs geometric considerations in the present discussion.

ΔG_{tot}^{*} is then 830-1280 cm-1. Assuming $\Delta G_{tot}^{*} \sim \lambda/4$, then the vertical reorganization energy λ is 3320-5120 cm^{-1}. The estimated reorganization energy for the $[Ru_3O(OAc)_6(py)_3]^{+/0}$ pair is substantially less than that of 10,000 cm^{-1} for the $[Ru_3O(OAc)_6(CO)(py)_2]^{0/-}$ pair, though the outer sphere components are likely very similar.

4.6 Conclusions

This work represents the most complete study to date of electronic structural effects in electron self-exchange reactions. The $A_2^{''}$ SOMO of the $Ru_3^{III,II,II}$ cluster $[Ru_3O(OAc)_6(CO)(L)_2]^-$ allows electronic delocalization to the π* systems of the peripheral pyridine ligands. This leads to large reorganization energies that are compensated by strong coupling, H_{AB}, that arises from effective orbital overlap between the pyridine π* systems of donor/acceptor pairs in the precursor complexes. Electron exchange between the $Ru_3^{III,III,III/III,III,II}$ pair $[Ru_3O(OAc)_6(L)_3]^{+/0}$ involves electronic configurations that are nominally $(A_2^{'})^1$ and $(A_2^{'})^2$. Electron delocalization is then restricted to the Ru_3 cores. This leads to small reorganization energies, negligibly small electronic couplings, H_{AB}, and an absence of pyridine substituent effects on rates of self-exchange.

4.7 Experimental

General. Deuterated solvents (CD_2Cl_2 99.9% D and CD_3CN 99.8% D, Cambridge Isotope) were distilled from CaH_2 under argon. Cobaltocene, decamethylcobaltocene, and ferrocenium hexafluorophosphate were used as received from Sigma Aldrich. Elemental analysis was performed by Numega Resonance Labs, San Diego, CA.

$[Ru_3O(OAc)_6(cpy)_3]$ (**5**) was prepared analogously to the literature procedure[3] for $\mathbf{6}^+$ but isolated as a neutral complex without the addition of a reductant, as reported for $Ru_3O(OAc)_6$ clusters with electron withdrawing ligands. Yield, 40%. ^{1}H NMR (500 MHz, CD_2Cl_2): δ ppm 9.21 (d, J = 6.59 Hz, 6 H), 7.91 (d, J = 6.59 Hz, 6 H), 2.01 (s, 18 H). UV/vis (CH_2Cl_2) nm (ε $M^{-1}s^{-1}$) 265 (16500), 497 (11300), 799 (sh, 5600), 936 (9300). IR (KBr) cm^{-1} 2237, 1604, 1561, 1547, 1492, 1423, 1349, 1225, 1198, 1023, 835, 689, 559, 487. ESI MS (neg. mode) m/z calc. 986.9, found 986.4. Elemental analysis: calc. for $Ru_3O(OAc)_6(cpy)_3 \cdot 4H_2O$ $C_{30}H_{38}N_6O_{17}Ru_3$ C 34.06; H 3.62; N 7.94. Found 34.12; 3.49; 7.90. CV – reduction potential for the +/0 couple is -370 mV vs. Fc/Fc^+ in CH_2Cl_2.

$[Ru_3O(OAc)_6(py)_3]$ (**6**) was prepared according to the literature procedure[3] and NMR, IR, and UV/vis analyses matched those reported. The reduction potential for the +/0 couple is -560 mV vs. Fc/Fc^+ in CH_2Cl_2. $[Ru_3O(OAc)_6(py)3][PF6]$ ($\mathbf{6}^+PF_6^-$) was prepared similarly, and crystals suitable for x-ray diffraction studies were obtained fortuitously from the slow evaporation of a CH_2Cl_2/MeOH layered diffusion.

$[Ru_3O(OAc)_6(dmap)_3][PF_6]$ ($\mathbf{7}^+PF_6^-$) was prepared in the same manner as $[Ru_3O(OAc)_6(py)_3][PF_6]$.[3] Yield, 33%. ^{1}H NMR (500 MHz, CD_2Cl_2): δ ppm 6.17 (d, J = 5.15 Hz, 6 H), 5.42 (s, 18 H), 2.77 (s, 18 H), 2.02 (d, J = 6.01 Hz, 6 H). UV/vis (CH_2Cl_2) nm (ε $M^{-1}s^{-1}$) 271 (47000), 418 (10100), 503 (5300), 629 (7600), 691 (8600). IR (KBr) cm^{-1} 1620, 1535, 1428, 1380, 1347, 1229, 1070, 1022, 841, 686, 560. ESI MS (neg. mode) m/z calc. 1041.0, found 1040.7. Elemental analysis: calc. for $C_{33}H_{48}F_6N_6O_{13}PRu_3$ C 33.34; H 4.08; N 7.09. Found 33.11; 4.04; 7.12. CV – reduction potential for the +/0 couple is -770 mV vs. Fc/Fc^+ in CH_2Cl_2.

$[Ru_3O(OAc)_6(CO)(iq)_2]$ (**4**) was synthesized by addition of 5 equivalents of isoquinoline (iq) to the $[Ru_3O(OAc)_6(CO)(H_2O)_2]$ cluster[7] dissolved in a small amount of CH_2Cl_2/MeOH. After stirring overnight, the solvent was evaporated, the solid was recrystallized from chloroform/hexanes, washed extensively with hexanes, and dried in a vacuum desiccator. Yield, 90%. Crystals suitable for x-ray diffraction studies were grown by diffusion of pentane into a solution in $CDCl_3$. ^{1}H NMR (500 MHz, $CDCl_3$): δ ppm 9.89 (s, 2 H), 9.15 (d, J = 6.37 Hz, 2 H), 8.46 (d, J = 8.23 Hz, 2 H), 8.34 (d, J = 8.23 Hz, 2 H), 8.06 (t, J = 7.88, 2 H), 7.95 (t, J = 8.09 Hz, 2 H), 2.00 (s, 12 H) 1.78 (s, 6 H). UV/vis (CD_3CN) nm (ε $M^{-1}s^{-1}$) 345 (5600), 379 (4300), 588 (3800). IR (KBr) cm^{-1} 1945, 1634, 1610, 1574, 1425, 1390, 1351. ESI MS (pos. mode) m/z calc. 960.9, found 983.6 ($M + Na^+$). Elemental analysis: calc. for $C_{31}H_{32}N_6O_{14}Ru_3$ C 38.79; H 3.36; N 2.92. Found 38.43; 3.68; 3.00. CV – reduction potential for the 0/- couple is -1250 vs. Fc/Fc^+ in MeCN.

Sample Preparation. Samples for NMR and UV/vis experiments were prepared in a nitrogen-filled glove box. Solutions were prepared in the appropriate dried deuterated solvent, and approximately half of the solution was added to 1.3 equivalents of either ferrocenium hexafluorophosphate (for **5** and **6**), cobaltocene (for $\mathbf{7}^+$), or decamethylcobaltocene (for **4**). The fully

oxidized and reduced solutions were mixed in varying proportions. A total of 0.6 mL for each sample was added to standard NMR tubes (500 MHz, Wilmad), capped, and sealed with tape. Samples for UV/vis were injected into an airtight cell with CaF_2 windows and a 0.1 mm path length before removal from the glovebox.

UV/vis Data Collection. UV/vis data were collected on a Shimadzu UV-3600 UV/vis/NIR spectrometer.

NMR Data Collection and Analysis. ^{1}H spectra (64 scans) were collected on a JEOL 500 MHz NMR spectrometer and analyzed using JEOL Delta software. Peak positions were used to determine the ratio of oxidized to reduced sample, as linear relationships have previously been confirmed.[2, 6] Peaks were fit to Lorentzian lineshapes in the Delta software. Each reported rate constant is an average of at least four values calculated from equation 1. All spectra were recorded at the ambient temperature of the instrument (18-20 ºC).

Electrochemical Measurements. Electrochemistry was performed with a BAS Epsilon potentiostat in dried deoxygenated CH_2Cl_2 with 0.1 M tetrabutylammonium hexafluorophosphate (TBAH, recrystallized from MeOH and dried under vacuum at 80 ºC) and 0.5-7 mM sample concentrations at a scan rate of 100 mV/s in a dedicated glovebox. The working electrode was a platinum disk (1.6 mm diameter). The counter electrode was a platinum wire, and the reference was the ferrocene/ferrocenium couple.

Crystallographic Structure Determinations. Single-crystal X-ray structure determinations were carried out at 100(2) K on either a Bruker P4 or Platform Diffractometer using Mo Kα radiation (λ = 0.71073 Å) in conjunction with a Bruker APEX detector. All structures were solved by direct methods using SHELXS-97 and refined with full-matrix least-squares procedures using SHELXL-97.[36] CIF files can be found as supplementary information.

Note: Much of the material for this chapter comes directly from a manuscript entitled “Electronic structural effects in self-exchange reactions” by John C. Goeltz, Eric E. Benson, and Clifford P.

Kubiak, which has been published in *Journal of Physical Chemistry B,* **2010,** *114,* 14729-14734. http://dx.doi.org/10.1021/jp103009b The dissertation author is the primary author of this manuscript.

4.8 Appendix

Table 4-2. Crystal data and structure refinement for complex **4**.

Identification code	jg_041409_0m	
Empirical formula	C34 H35 Cl9 N2 O14 Ru3	
Formula weight	1317.90	
Temperature	150(2) K	
Wavelength	0.71073 Å	
Crystal system	Monoclinic	
Space group	P2(1)/n	
Unit cell dimensions	a = 14.657(6) Å	α= 90°.
	b = 18.300(8) Å	β= 95.826(6)°.
	c = 17.958(8) Å	γ = 90°.
Volume	4792(4) $Å^3$	
Z	4	
Density (calculated)	1.827 Mg/m^3	
Absorption coefficient	1.497 mm^{-1}	
F(000)	2600	
Crystal size	0.30 x 0.20 x 0.10 mm^3	
Theta range for data collection	1.59 to 25.68°.	
Index ranges	-17<=h<=17, -22<=k<=22, -21<=l<=21	
Reflections collected	43463	
Independent reflections	9022 [R(int) = 0.0455]	
Completeness to theta = 25.00°	100.0 %	
Absorption correction	Semi-empirical from equivalents	
Max. and min. transmission	0.8648 and 0.6623	
Refinement method	Full-matrix least-squares on F^2	
Data / restraints / parameters	9022 / 0 / 619	
Goodness-of-fit on F^2	1.051	
Final R indices [I>2sigma(I)]	R1 = 0.0388, wR2 = 0.0866	

Table 4-2. Crystal data and structure refinement for complex **4**. continued.

R indices (all data)	R1 = 0.0529, wR2 = 0.0959
Largest diff. peak and hole	1.714 and -1.471 e.Å^{-3}

Table 4-3. Bond lengths [Å] and angles [°] for complex **4**.

C(27A)-C(28A)	1.34(3)
C(27A)-N(2)	1.486(17)
C(28A)-C(25)	1.537(17)
C(29A)-C(24)	1.305(12)
C(29A)-C(30A)	1.346(15)
C(30A)-C(31A)	1.41(3)
C(31A)-C(26)	1.17(2)
C(27B)-N(2)	1.27(2)
C(27B)-C(28B)	1.38(3)
C(28B)-C(25)	1.20(2)
C(29B)-C(30B)	1.367(17)
C(29B)-C(24)	1.602(17)
C(30B)-C(31B)	1.38(2)
C(31B)-C(26)	1.53(2)
C(25)-C(24)	1.409(8)
C(25)-C(26)	1.422(9)
C(24)-C(23)	1.435(8)
C(23)-N(2)	1.285(7)
C(22)-C(21)	1.369(6)
C(22)-N(1)	1.370(5)
C(14)-N(1)	1.316(6)
C(14)-C(15)	1.413(6)
C(1)-O(14)	1.158(6)
C(1)-Ru(2)	1.842(5)
C(3)-C(2)	1.501(6)
C(21)-C(20)	1.408(7)
C(20)-C(15)	1.410(6)
C(20)-C(19)	1.430(6)
C(15)-C(16)	1.412(6)
C(16)-C(17)	1.368(7)
C(19)-C(18)	1.354(7)
C(18)-C(17)	1.405(7)

Table 4-3. Bond lengths [Å] and angles [°] for complex **4**, continued.

C(34)-Cl(5)	1.748(6)
C(34)-Cl(4)	1.764(7)
C(34)-Cl(6)	1.765(6)
C(32)-Cl(1)	1.750(5)
C(32)-Cl(3)	1.755(5)
C(32)-Cl(2)	1.758(5)
C(33)-Cl(8)	1.750(5)
C(33)-Cl(9)	1.752(5)
C(33)-Cl(7)	1.755(5)
N(1)-Ru(3)	2.117(3)
C(4)-O(4)	1.258(6)
C(4)-O(2)	1.262(6)
C(4)-C(5)	1.515(7)
C(2)-O(5)	1.255(5)
C(2)-O(3)	1.263(5)
C(10)-O(6)	1.256(5)
C(10)-O(9)	1.263(5)
C(10)-C(11)	1.501(6)
C(12)-O(7)	1.259(5)
C(12)-O(8)	1.270(5)
C(12)-C(13)	1.504(6)
C(8)-O(10)	1.263(5)
C(8)-O(12)	1.265(6)
C(8)-C(9)	1.510(7)
C(6)-O(13)	1.257(5)
C(6)-O(11)	1.271(5)
C(6)-C(7)	1.504(6)
N(2)-Ru(1)	2.129(4)
O(1)-Ru(3)	1.888(3)
O(1)-Ru(1)	1.894(3)
O(1)-Ru(2)	2.056(3)
O(2)-Ru(1)	2.040(4)
O(3)-Ru(1)	2.059(3)

Table 4-3. Bond lengths [Å] and angles [°] for complex **4**, continued.

O(4)-Ru(2)	2.093(3)
O(5)-Ru(2)	2.074(3)
O(6)-Ru(2)	2.076(3)
O(7)-Ru(2)	2.090(3)
O(8)-Ru(3)	2.032(3)
O(9)-Ru(3)	2.042(3)
O(10)-Ru(3)	2.062(3)
O(11)-Ru(3)	2.033(3)
O(12)-Ru(1)	2.049(3)
O(13)-Ru(1)	2.058(3)

C(28A)-C(27A)-N(2)	116.1(12)
C(27A)-C(28A)-C(25)	121.5(13)
C(24)-C(29A)-C(30A)	119.2(10)
C(29A)-C(30A)-C(31A)	121.9(14)
C(26)-C(31A)-C(30A)	118.5(18)
N(2)-C(27B)-C(28B)	129.8(19)
C(25)-C(28B)-C(27B)	120.3(18)
C(30B)-C(29B)-C(24)	118.8(12)
C(29B)-C(30B)-C(31B)	118.7(16)
C(30B)-C(31B)-C(26)	123.5(16)
C(28B)-C(25)-C(24)	114.4(11)
C(28B)-C(25)-C(26)	124.9(11)
C(24)-C(25)-C(26)	117.0(7)
C(28B)-C(25)-C(28A)	26.7(16)
C(24)-C(25)-C(28A)	117.6(8)
C(26)-C(25)-C(28A)	124.8(9)
C(29A)-C(24)-C(25)	116.8(7)
C(29A)-C(24)-C(23)	122.8(7)
C(25)-C(24)-C(23)	116.7(6)
C(29A)-C(24)-C(29B)	38.1(6)
C(25)-C(24)-C(29B)	119.2(6)
C(23)-C(24)-C(29B)	120.2(7)

Table 4-3. Bond lengths [Å] and angles [°] for complex **4**, continued.

N(2)-C(23)-C(24)	124.3(6)
C(21)-C(22)-N(1)	122.1(4)
N(1)-C(14)-C(15)	123.9(4)
O(14)-C(1)-Ru(2)	178.5(4)
C(22)-C(21)-C(20)	120.1(4)
C(21)-C(20)-C(15)	118.0(4)
C(21)-C(20)-C(19)	123.5(4)
C(15)-C(20)-C(19)	118.5(4)
C(16)-C(15)-C(20)	120.0(4)
C(16)-C(15)-C(14)	122.5(4)
C(20)-C(15)-C(14)	117.5(4)
C(17)-C(16)-C(15)	120.1(4)
C(18)-C(19)-C(20)	119.9(4)
C(19)-C(18)-C(17)	121.6(4)
C(16)-C(17)-C(18)	120.0(5)
Cl(5)-C(34)-Cl(4)	108.4(4)
Cl(5)-C(34)-Cl(6)	111.0(3)
Cl(4)-C(34)-Cl(6)	109.9(3)
Cl(1)-C(32)-Cl(3)	111.0(3)
Cl(1)-C(32)-Cl(2)	110.6(3)
Cl(3)-C(32)-Cl(2)	109.2(3)
C(31A)-C(26)-C(25)	123.5(13)
C(31A)-C(26)-C(31B)	22.2(11)
C(25)-C(26)-C(31B)	118.7(10)
Cl(8)-C(33)-Cl(9)	109.9(3)
Cl(8)-C(33)-Cl(7)	110.6(3)
Cl(9)-C(33)-Cl(7)	110.8(3)
C(14)-N(1)-C(22)	118.4(4)
C(14)-N(1)-Ru(3)	121.4(3)
C(22)-N(1)-Ru(3)	120.2(3)
O(4)-C(4)-O(2)	127.6(4)
O(4)-C(4)-C(5)	117.3(5)
O(2)-C(4)-C(5)	115.1(5)

Table 4-3. Bond lengths [Å] and angles [°] for complex **4**, continued.

O(5)-C(2)-O(3)	127.0(4)
O(5)-C(2)-C(3)	116.4(4)
O(3)-C(2)-C(3)	116.5(4)
O(6)-C(10)-O(9)	126.8(4)
O(6)-C(10)-C(11)	116.7(4)
O(9)-C(10)-C(11)	116.5(4)
O(7)-C(12)-O(8)	127.1(4)
O(7)-C(12)-C(13)	116.9(4)
O(8)-C(12)-C(13)	116.1(4)
O(10)-C(8)-O(12)	126.6(4)
O(10)-C(8)-C(9)	116.4(4)
O(12)-C(8)-C(9)	117.0(4)
O(13)-C(6)-O(11)	126.3(4)
O(13)-C(6)-C(7)	118.2(4)
O(11)-C(6)-C(7)	115.6(4)
C(27B)-N(2)-C(23)	108.6(10)
C(27B)-N(2)-C(27A)	27.1(13)
C(23)-N(2)-C(27A)	122.5(8)
C(27B)-N(2)-Ru(1)	127.4(10)
C(23)-N(2)-Ru(1)	122.7(4)
C(27A)-N(2)-Ru(1)	113.5(7)
Ru(3)-O(1)-Ru(1)	120.63(16)
Ru(3)-O(1)-Ru(2)	119.71(15)
Ru(1)-O(1)-Ru(2)	119.63(14)
C(4)-O(2)-Ru(1)	130.1(3)
C(2)-O(3)-Ru(1)	133.3(3)
C(4)-O(4)-Ru(2)	131.7(3)
C(2)-O(5)-Ru(2)	128.2(3)
C(10)-O(6)-Ru(2)	128.9(3)
C(12)-O(7)-Ru(2)	134.5(3)
C(12)-O(8)-Ru(3)	128.7(3)
C(10)-O(9)-Ru(3)	133.0(3)
C(8)-O(10)-Ru(3)	132.7(3)

Table 4-3. Bond lengths [Å] and angles [°] for complex **4**, continued.

C(6)-O(11)-Ru(3)	124.8(3)
C(8)-O(12)-Ru(1)	125.6(3)
C(6)-O(13)-Ru(1)	131.8(3)
O(1)-Ru(1)-O(2)	92.58(13)
O(1)-Ru(1)-O(12)	94.38(12)
O(2)-Ru(1)-O(12)	172.72(13)
O(1)-Ru(1)-O(13)	96.11(12)
O(2)-Ru(1)-O(13)	88.90(13)
O(12)-Ru(1)-O(13)	88.22(13)
O(1)-Ru(1)-O(3)	95.78(12)
O(2)-Ru(1)-O(3)	92.46(13)
O(12)-Ru(1)-O(3)	88.98(13)
O(13)-Ru(1)-O(3)	167.96(12)
O(1)-Ru(1)-N(2)	176.28(17)
O(2)-Ru(1)-N(2)	83.83(17)
O(12)-Ru(1)-N(2)	89.26(16)
O(13)-Ru(1)-N(2)	84.80(14)
O(3)-Ru(1)-N(2)	83.46(14)
C(1)-Ru(2)-O(1)	179.45(17)
C(1)-Ru(2)-O(5)	88.15(17)
O(1)-Ru(2)-O(5)	91.30(12)
C(1)-Ru(2)-O(6)	89.24(17)
O(1)-Ru(2)-O(6)	91.30(12)
O(5)-Ru(2)-O(6)	177.38(12)
C(1)-Ru(2)-O(7)	89.07(17)
O(1)-Ru(2)-O(7)	90.82(12)
O(5)-Ru(2)-O(7)	84.93(12)
O(6)-Ru(2)-O(7)	95.36(12)
C(1)-Ru(2)-O(4)	87.16(17)
O(1)-Ru(2)-O(4)	92.94(12)
O(5)-Ru(2)-O(4)	94.46(12)
O(6)-Ru(2)-O(4)	85.08(13)
O(7)-Ru(2)-O(4)	176.20(12)

Table 4-3. Bond lengths [Å] and angles [°] for complex **4**, continued.

O(1)-Ru(3)-O(8)	93.72(12)
O(1)-Ru(3)-O(11)	93.76(12)
O(8)-Ru(3)-O(11)	172.50(12)
O(1)-Ru(3)-O(9)	96.70(13)
O(8)-Ru(3)-O(9)	92.76(12)
O(11)-Ru(3)-O(9)	86.95(12)
O(1)-Ru(3)-O(10)	95.21(12)
O(8)-Ru(3)-O(10)	87.47(12)
O(11)-Ru(3)-O(10)	91.26(12)
O(9)-Ru(3)-O(10)	168.05(12)
O(1)-Ru(3)-N(1)	179.53(14)
O(8)-Ru(3)-N(1)	86.54(13)
O(11)-Ru(3)-N(1)	85.98(13)
O(9)-Ru(3)-N(1)	83.69(13)
O(10)-Ru(3)-N(1)	84.40(13)

Symmetry transformations used to generate equivalent atoms:

Table 4-4. Crystal data and structure refinement for complex $\mathbf{6}^{+}PF_6^{-}$.

Identification code	eb_091109b_0m	
Empirical formula	C27 H33 F6 N3 O13 P Ru3	
Formula weight	1055.74	
Temperature	150(2) K	
Wavelength	0.71073 Å	
Crystal system	Monoclinic	
Space group	P2(1)/n	
Unit cell dimensions	a = 21.330(2) Å	α= 90°.
	b = 7.7725(8) Å	β= 100.666(2)°.
	c = 22.864(2) Å	γ = 90°.
Volume	3725.2(7) $Å^3$	
Z	4	
Density (calculated)	1.882 Mg/m^3	
Absorption coefficient	1.337 mm^{-1}	
F(000)	2084	
Crystal size	0.50 x 0.20 x 0.10 mm^3	
Theta range for data collection	1.45 to 25.64°.	
Index ranges	-25<=h<=25, -8<=k<=9, -27<=l<=27	
Reflections collected	35643	
Independent reflections	7003 [R(int) = 0.0612]	
Completeness to theta = 25.00°	100.0 %	
Absorption correction	Semi-empirical from equivalents	
Max. and min. transmission	0.8779 and 0.5545	
Refinement method	Full-matrix least-squares on F^2	
Data / restraints / parameters	7003 / 0 / 484	
Goodness-of-fit on F^2	1.068	
Final R indices [I>2sigma(I)]	R1 = 0.0448, wR2 = 0.1002	
R indices (all data)	R1 = 0.0613, wR2 = 0.1088	
Largest diff. peak and hole	2.156 and -0.671 $e.Å^{-3}$	

Table 4-5. Bond lengths [Å] and angles [°] for complex $\mathbf{6}^{+}PF_6^{-}$.

C(1)-O(3)	1.255(7)
C(1)-O(2)	1.261(6)
C(1)-C(2)	1.506(7)
C(2)-H(2A)	0.9800
C(2)-H(2B)	0.9800
C(2)-H(2C)	0.9800
C(3)-O(4)	1.257(6)
C(3)-O(5)	1.259(7)
C(3)-C(4)	1.497(8)
C(4)-H(4A)	0.9800
C(4)-H(4B)	0.9800
C(4)-H(4C)	0.9800
C(5)-O(6)	1.256(6)
C(5)-O(7)	1.261(6)
C(5)-C(6)	1.504(8)
C(6)-H(6A)	0.9800
C(6)-H(6B)	0.9800
C(6)-H(6C)	0.9800
C(7)-O(9)	1.249(6)
C(7)-O(8)	1.257(6)
C(7)-C(8)	1.501(7)
C(8)-H(8A)	0.9800
C(8)-H(8B)	0.9800
C(8)-H(8C)	0.9800
C(9)-O(11)	1.262(6)
C(9)-O(10)	1.267(7)
C(9)-C(10)	1.492(7)
C(10)-H(10A)	0.9800
C(10)-H(10B)	0.9800
C(10)-H(10C)	0.9800
C(11)-O(13)	1.255(6)
C(11)-O(12)	1.272(7)

Table 4-5. Bond lengths [Å] and angles [°] for complex $\mathbf{6}^{+}PF_6^{-}$, continued.

C(11)-C(12)	1.491(7)
C(12)-H(12A)	0.9800
C(12)-H(12B)	0.9800
C(12)-H(12C)	0.9800
C(13)-N(1)	1.346(7)
C(13)-C(14)	1.382(8)
C(13)-H(13)	0.9500
C(14)-C(15)	1.380(9)
C(14)-H(14)	0.9500
C(15)-C(16)	1.386(9)
C(15)-H(15)	0.9500
C(16)-C(17)	1.373(8)
C(16)-H(16)	0.9500
C(17)-N(1)	1.352(7)
C(17)-H(17)	0.9500
C(18)-N(2)	1.341(8)
C(18)-C(19)	1.394(8)
C(18)-H(18)	0.9500
C(19)-C(20)	1.381(9)
C(19)-H(19)	0.9500
C(20)-C(21)	1.375(9)
C(20)-H(20)	0.9500
C(21)-C(22)	1.391(8)
C(21)-H(21)	0.9500
C(22)-N(2)	1.351(7)
C(22)-H(22)	0.9500
C(23)-N(3)	1.354(7)
C(23)-C(24)	1.370(8)
C(23)-H(23)	0.9500
C(24)-C(25)	1.392(8)
C(24)-H(24)	0.9500
C(25)-C(26)	1.380(8)
C(25)-H(25)	0.9500

Table 4-5. Bond lengths [Å] and angles [°] for complex $\mathbf{6}^{+}PF_6^{-}$, continued.

C(26)-C(27)	1.388(8)
C(26)-H(26)	0.9500
C(27)-N(3)	1.355(7)
C(27)-H(27)	0.9500
N(1)-Ru(2)	2.104(4)
N(2)-Ru(3)	2.110(4)
N(3)-Ru(1)	2.092(5)
O(1)-Ru(2)	1.913(4)
O(1)-Ru(1)	1.943(4)
O(1)-Ru(3)	1.947(3)
O(2)-Ru(1)	2.043(4)
O(3)-Ru(2)	2.044(4)
O(4)-Ru(1)	2.039(4)
O(5)-Ru(2)	2.047(4)
O(6)-Ru(2)	2.035(4)
O(7)-Ru(3)	2.041(4)
O(8)-Ru(2)	2.037(4)
O(9)-Ru(3)	2.034(4)
O(10)-Ru(3)	2.015(4)
O(11)-Ru(1)	2.026(4)
O(12)-Ru(3)	2.024(4)
O(13)-Ru(1)	2.034(4)
F(1)-P(1)	1.592(4)
F(2)-P(1)	1.603(4)
F(3)-P(1)	1.597(4)
F(4)-P(1)	1.605(5)
F(5)-P(1)	1.603(5)
F(6)-P(1)	1.579(5)
O(3)-C(1)-O(2)	126.3(5)
O(3)-C(1)-C(2)	117.1(5)
O(2)-C(1)-C(2)	116.6(5)
C(1)-C(2)-H(2A)	109.5

Table 4-5. Bond lengths [Å] and angles [°] for complex $\mathbf{6}^{+}PF_6^{-}$, continued.

C(1)-C(2)-H(2B)	109.5
H(2A)-C(2)-H(2B)	109.5
C(1)-C(2)-H(2C)	109.5
H(2A)-C(2)-H(2C)	109.5
H(2B)-C(2)-H(2C)	109.5
O(4)-C(3)-O(5)	125.4(5)
O(4)-C(3)-C(4)	116.9(5)
O(5)-C(3)-C(4)	117.7(5)
C(3)-C(4)-H(4A)	109.5
C(3)-C(4)-H(4B)	109.5
H(4A)-C(4)-H(4B)	109.5
C(3)-C(4)-H(4C)	109.5
H(4A)-C(4)-H(4C)	109.5
H(4B)-C(4)-H(4C)	109.5
O(6)-C(5)-O(7)	125.6(5)
O(6)-C(5)-C(6)	117.2(5)
O(7)-C(5)-C(6)	117.1(5)
C(5)-C(6)-H(6A)	109.5
C(5)-C(6)-H(6B)	109.5
H(6A)-C(6)-H(6B)	109.5
C(5)-C(6)-H(6C)	109.5
H(6A)-C(6)-H(6C)	109.5
H(6B)-C(6)-H(6C)	109.5
O(9)-C(7)-O(8)	126.3(5)
O(9)-C(7)-C(8)	116.3(5)
O(8)-C(7)-C(8)	117.4(5)
C(7)-C(8)-H(8A)	109.5
C(7)-C(8)-H(8B)	109.5
H(8A)-C(8)-H(8B)	109.5
C(7)-C(8)-H(8C)	109.5
H(8A)-C(8)-H(8C)	109.5
H(8B)-C(8)-H(8C)	109.5
O(11)-C(9)-O(10)	125.3(5)

Table 4-5. Bond lengths [Å] and angles [°] for complex $\mathbf{6}^{+}PF_6^{-}$, continued.

O(11)-C(9)-C(10)	117.9(5)
O(10)-C(9)-C(10)	116.7(5)
C(9)-C(10)-H(10A)	109.5
C(9)-C(10)-H(10B)	109.5
H(10A)-C(10)-H(10B)	109.5
C(9)-C(10)-H(10C)	109.5
H(10A)-C(10)-H(10C)	109.5
H(10B)-C(10)-H(10C)	109.5
O(13)-C(11)-O(12)	125.7(5)
O(13)-C(11)-C(12)	117.1(5)
O(12)-C(11)-C(12)	117.2(5)
C(11)-C(12)-H(12A)	109.5
C(11)-C(12)-H(12B)	109.5
H(12A)-C(12)-H(12B)	109.5
C(11)-C(12)-H(12C)	109.5
H(12A)-C(12)-H(12C)	109.5
H(12B)-C(12)-H(12C)	109.5
N(1)-C(13)-C(14)	121.8(5)
N(1)-C(13)-H(13)	119.1
C(14)-C(13)-H(13)	119.1
C(15)-C(14)-C(13)	119.4(6)
C(15)-C(14)-H(14)	120.3
C(13)-C(14)-H(14)	120.3
C(14)-C(15)-C(16)	119.0(5)
C(14)-C(15)-H(15)	120.5
C(16)-C(15)-H(15)	120.5
C(17)-C(16)-C(15)	118.8(6)
C(17)-C(16)-H(16)	120.6
C(15)-C(16)-H(16)	120.6
N(1)-C(17)-C(16)	122.6(6)
N(1)-C(17)-H(17)	118.7
C(16)-C(17)-H(17)	118.7
N(2)-C(18)-C(19)	122.4(6)

Table 4-5. Bond lengths [Å] and angles [°] for complex $\mathbf{6}^{+}PF_6^{-}$, continued.

N(2)-C(18)-H(18)	118.8
C(19)-C(18)-H(18)	118.8
C(20)-C(19)-C(18)	118.7(6)
C(20)-C(19)-H(19)	120.7
C(18)-C(19)-H(19)	120.7
C(21)-C(20)-C(19)	119.4(6)
C(21)-C(20)-H(20)	120.3
C(19)-C(20)-H(20)	120.3
C(20)-C(21)-C(22)	119.0(6)
C(20)-C(21)-H(21)	120.5
C(22)-C(21)-H(21)	120.5
N(2)-C(22)-C(21)	122.0(6)
N(2)-C(22)-H(22)	119.0
C(21)-C(22)-H(22)	119.0
N(3)-C(23)-C(24)	122.3(5)
N(3)-C(23)-H(23)	118.8
C(24)-C(23)-H(23)	118.8
C(23)-C(24)-C(25)	119.1(5)
C(23)-C(24)-H(24)	120.5
C(25)-C(24)-H(24)	120.5
C(26)-C(25)-C(24)	119.5(6)
C(26)-C(25)-H(25)	120.3
C(24)-C(25)-H(25)	120.3
C(25)-C(26)-C(27)	118.8(5)
C(25)-C(26)-H(26)	120.6
C(27)-C(26)-H(26)	120.6
N(3)-C(27)-C(26)	122.0(5)
N(3)-C(27)-H(27)	119.0
C(26)-C(27)-H(27)	119.0
C(13)-N(1)-C(17)	118.4(5)
C(13)-N(1)-Ru(2)	120.7(4)
C(17)-N(1)-Ru(2)	120.9(4)
C(18)-N(2)-C(22)	118.3(5)

Table 4-5. Bond lengths [Å] and angles [°] for complex $\mathbf{6}^{+}PF_6^{-}$, continued.

C(18)-N(2)-Ru(3)	122.0(4)
C(22)-N(2)-Ru(3)	119.5(4)
C(23)-N(3)-C(27)	118.4(5)
C(23)-N(3)-Ru(1)	119.9(4)
C(27)-N(3)-Ru(1)	121.6(4)
Ru(2)-O(1)-Ru(1)	119.95(18)
Ru(2)-O(1)-Ru(3)	120.34(19)
Ru(1)-O(1)-Ru(3)	119.71(18)
C(1)-O(2)-Ru(1)	132.8(4)
C(1)-O(3)-Ru(2)	131.7(3)
C(3)-O(4)-Ru(1)	133.1(4)
C(3)-O(5)-Ru(2)	132.5(4)
C(5)-O(6)-Ru(2)	134.5(4)
C(5)-O(7)-Ru(3)	130.3(4)
C(7)-O(8)-Ru(2)	130.2(4)
C(7)-O(9)-Ru(3)	132.8(3)
C(9)-O(10)-Ru(3)	133.9(4)
C(9)-O(11)-Ru(1)	131.6(4)
C(11)-O(12)-Ru(3)	132.0(3)
C(11)-O(13)-Ru(1)	134.0(4)
F(6)-P(1)-F(1)	91.7(3)
F(6)-P(1)-F(3)	89.7(3)
F(1)-P(1)-F(3)	178.7(3)
F(6)-P(1)-F(5)	92.0(3)
F(1)-P(1)-F(5)	90.0(3)
F(3)-P(1)-F(5)	89.8(3)
F(6)-P(1)-F(2)	178.7(3)
F(1)-P(1)-F(2)	88.7(2)
F(3)-P(1)-F(2)	90.0(2)
F(5)-P(1)-F(2)	89.2(3)
F(6)-P(1)-F(4)	90.2(3)
F(1)-P(1)-F(4)	89.6(3)
F(3)-P(1)-F(4)	90.5(3)

Table 4-5. Bond lengths [Å] and angles [°] for complex $\mathbf{6}^{+}PF_6^{-}$, continued.

F(5)-P(1)-F(4)	177.7(3)
F(2)-P(1)-F(4)	88.5(3)
O(1)-Ru(1)-O(11)	95.74(16)
O(1)-Ru(1)-O(13)	93.21(15)
O(11)-Ru(1)-O(13)	91.82(17)
O(1)-Ru(1)-O(4)	96.04(15)
O(11)-Ru(1)-O(4)	168.18(16)
O(13)-Ru(1)-O(4)	88.51(17)
O(1)-Ru(1)-O(2)	94.12(15)
O(11)-Ru(1)-O(2)	88.97(17)
O(13)-Ru(1)-O(2)	172.52(16)
O(4)-Ru(1)-O(2)	89.20(17)
O(1)-Ru(1)-N(3)	178.93(15)
O(11)-Ru(1)-N(3)	83.57(17)
O(13)-Ru(1)-N(3)	86.02(16)
O(4)-Ru(1)-N(3)	84.68(16)
O(2)-Ru(1)-N(3)	86.68(16)
O(1)-Ru(2)-O(6)	94.24(15)
O(1)-Ru(2)-O(8)	94.03(15)
O(6)-Ru(2)-O(8)	92.21(18)
O(1)-Ru(2)-O(3)	94.17(15)
O(6)-Ru(2)-O(3)	86.80(18)
O(8)-Ru(2)-O(3)	171.79(15)
O(1)-Ru(2)-O(5)	97.35(16)
O(6)-Ru(2)-O(5)	168.21(15)
O(8)-Ru(2)-O(5)	89.12(17)
O(3)-Ru(2)-O(5)	90.21(18)
O(1)-Ru(2)-N(1)	178.45(16)
O(6)-Ru(2)-N(1)	85.90(17)
O(8)-Ru(2)-N(1)	84.42(16)
O(3)-Ru(2)-N(1)	87.38(16)
O(5)-Ru(2)-N(1)	82.57(16)
O(1)-Ru(3)-O(10)	96.87(15)

Table 4-5. Bond lengths [Å] and angles [°] for complex $\mathbf{6}^{+}PF_6^{-}$, continued.

O(1)-Ru(3)-O(12)	92.94(15)
O(10)-Ru(3)-O(12)	90.46(19)
O(1)-Ru(3)-O(9)	96.03(15)
O(10)-Ru(3)-O(9)	167.09(15)
O(12)-Ru(3)-O(9)	89.42(19)
O(1)-Ru(3)-O(7)	93.61(15)
O(10)-Ru(3)-O(7)	90.06(18)
O(12)-Ru(3)-O(7)	173.32(15)
O(9)-Ru(3)-O(7)	88.58(18)
O(1)-Ru(3)-N(2)	177.91(17)
O(10)-Ru(3)-N(2)	81.04(17)
O(12)-Ru(3)-N(2)	87.00(17)
O(9)-Ru(3)-N(2)	86.06(17)
O(7)-Ru(3)-N(2)	86.50(17)

Symmetry transformations used to generate equivalent atoms:

4.9 References.

1. Glover, S. D.; Goeltz, J. C.; Lear, B. J.; Kubiak, C. P., *Eur. J. Inorg. Chem.* **2009**, 585-594.

2. Walsh, J. L.; Baumann, J. A.; Meyer, T. J., *Inorg. Chem.* **1980,** *19*, 2145-2151.

3. Baumann, J. A.; Salmon, D. J.; Wilson, S. T.; Meyer, T. J.; Hatfield, W. E., *Inorg. Chem.* **1978,** *17*, 3342-3350.

4. Baumann, J. A.; Wilson, S. T.; Salmon, D. J.; Hood, P. L.; Meyer, T. J., *J. Am. Chem. Soc.* **1979,** *101*, 2916-2920.

5. Delarosa, R.; Chang, P. J.; Salaymeh, F.; Curtis, J. C., *Inorg. Chem.* **1985,** *24*, 4229-4231.

6. Goeltz, J. C.; Hanson, C. J.; Kubiak, C. P., *Inorg. Chem.* **2009,** *48*, 4763-4767.

7. Ito, T.; Hamaguchi, T.; Nagino, H.; Yamaguchi, T.; Kido, H.; Zavarine, I. S.; Richmond, T.; Washington, J.; Kubiak, C. P., *J. Am. Chem. Soc.* **1999,** *121*, 4625-4632.

8. Ito, T.; Hamaguchi, T.; Nagino, H.; Yamaguchi, T.; Washington, J.; Kubiak, C. P., *Science (USA)* **1997,** *277*, 660-3.

9. Lear, B. J.; Glover, S. D.; Salsman, J. C.; Londergan, C. H.; Kubiak, C. P., *J. Am. Chem. Soc.* **2007,** *129*, 12772-12779.

10. Londergan, C. H.; Salsman, J. C.; Lear, B. J.; Kubiak, C. P., *Chem. Phys.* **2006,** *324*, 57-62.

11. Londergan, C. H.; Salsman, J. C.; Ronco, S.; Dolkas, L. M.; Kubiak, C. P., *J. Am. Chem. Soc.* **2002,** *124*, 6236-6237.

12. Salsman, J. C.; Kubiak, C. P.; Ito, T., *J. Am. Chem. Soc.* **2005,** *127*, 2382-2383.

13. Salsman, J. C.; Ronco, S.; Londergan, C. H.; Kubiak, C. P., *Inorg. Chem.* **2006,** *45*, 547-554.

14. Glover, S. D.; Lear, B. J.; Salsman, J. C.; Londergan, C. H.; Kubiak, C. P., *Phil. Trans. Roy. Soc. A* **2008,** *366*, 177-185.

15. Goeltz, J. C.; Benson, E. E.; Kubiak, C. P., *J. Phys. Chem. B* **2010,** *114*, 14729-14734.

16. Chan, M.-S.; DeRoos, J. B.; Wahl, A. C., *J. Phys. Chem.* **1973,** *77*, 2163-2165.

17. Brown, H. C., *Determination of Organic Structures by Physical Methods*. Academic Press: New York, 1955.

18. Brunschwig, B. S.; Creutz, C.; Sutin, N., *Chem. Soc. Rev.* **2002,** *31*, 168-184.

19. Marcus, R. A., *Annu. Rev. Phys. Chem.* **1964,** *15*, 155.

20. Newton, M. D., *Theor. Chem. Acc.* **2003,** *110*, 307-321.

21. Endicott, J. F.; Uddin, M. J., *Coord. Chem. Rev.* **2001,** *219*, 687-712.

22. Stanbury, D. M., *Nuclear factors in main-group electron transfer reactions*. 1997; Vol. 253, p 165-182.

23. Ballhausen, C. J.; Gray, H. B., *Molecular Orbital Theory*. 1st ed.; Benjamin: New York, 1965.

24. Marr, S. B.; Carvel, R. O.; Richens, D. T.; Lee, H. J.; Lane, M.; Stavropoulos, P., *Inorg. Chem.* **2000,** *39*, 4630-4638.

25. Marsh, R. E., *Acta Crystallogr B* **2002,** *58*, 893-899.

26. Sutin, N., *Prog. Inorg. Chem.* **1983,** *30*, 441-498.

27. Nielson, R. M.; Golovin, M. N.; McManis, G. E.; Weaver, M. J., *J. Am. Chem. Soc.* **1988,** *110*, 1745-1749.

28. Londergan, C. H.; Rocha, R. C.; Brown, M. G.; Shreve, A. P.; Kubiak, C. P., *J. Am. Chem. Soc.* **2003,** *125*, 13912-13913.

29. Rocha, R. C.; Brown, M. G.; Londergan, C. H.; Salsman, J. C.; Kubiak, C. P.; Shreve, A. P., *J. Phys. Chem. A.* **2005,** *109*, 9006-9012.

30. Nielson, R. M.; Golovin, M. N.; McManis, G. E.; Weaver, M. J., *J. Am. Chem. Soc.* **1988,** *110*, 1745-1749.

31. Gennett, T.; Milner, D. F.; Weaver, M. J., *J. Phys. Chem.* **1985,** *89*, 2787-2794.

32. Toma, H. E.; Araki, K.; Alexiou, A. D. P.; Nikolaou, S.; Dovidauskas, S., *Coord. Chem. Rev.* **2001,** *219*, 187-234.

33. Londergan, C. H.; Kubiak, C. P., *J. Phys. Chem. A* **2003,** *107*, 9301-9311.

34. Meesuk, L.; Jayasooriya, U. A.; Cannon, R. D., *J. Am. Chem. Soc.* **1987,** *109*, 2009-2016.

35. Gennett, T.; Milner, D. F.; Weaver, M. J., *The Journal of Physical Chemistry* **1985,** *89*, 2787-2794.

36. Sheldrick, G. M., *Acta Crystallogr A* **2008,** *64*, 112-122.

Chapter 5

Mixed valency across hydrogen bonds: a first look

5.1 Introduction

Mixed valency and proton-coupled electron transfer (PCET) are widely explored and relatively well understood fields,[1-9] but there are few reports from the intersection of the two.[10] There are many reported studies of photoinduced electron transfer across hydrogen bonds,[4, 11-15] often yielding surprisingly large donor-acceptor couplings and a large range of observed kinetic isotope effects. Symmetric ground state electron transfer coupled to one or more protons would offer a platform for experimental insight into fundamental electron transfer, electron delocalization as a stabilizing factor for hydrogen bonds in self-assembly, the stability of hydrogen bonds in the presence of electron density, and the many multi-electron multi-proton transformations in natural and artificial photosynthesis.

Complex **1** (Fig. 5-1), an oxo-centered trinuclear ruthenium cluster with one carbonyl, one pyridyl, and one isonicotinic acid ligand affords multiple chromophores and oxidation states, as well as access to a simple hydrogen bonding motif, the head-to-head dicarboxylic acid dimer.[16] Partial reduction of **1** results in the monoanionic dimer $(\mathbf{1})_2^-$ while full reduction gives a dianionic dimer, $(\mathbf{1})_2^{2-}$, each with a distinct electronic structure.

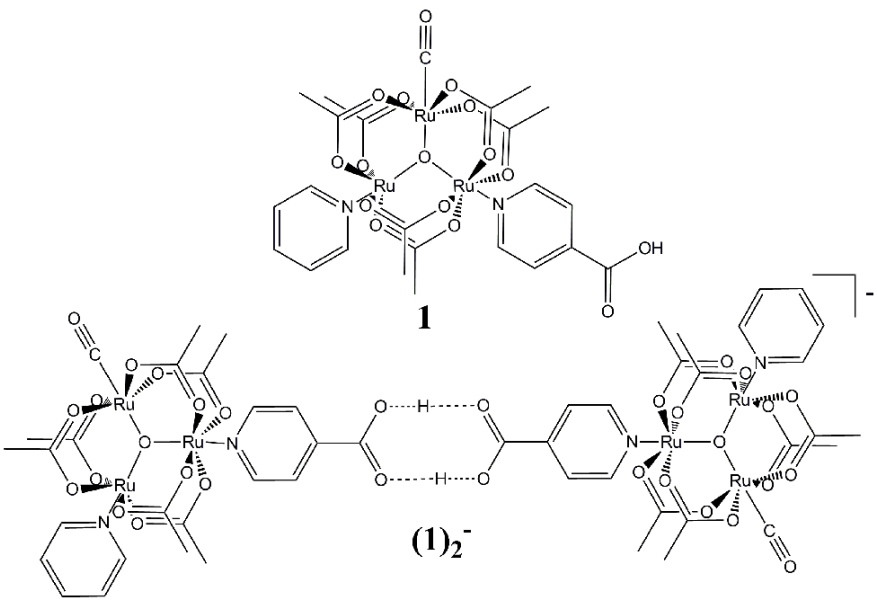

Figure 5-1. Structures of the isolated neutral ruthenium cluster **1** and the mixed valence dicarboxylic acid dimer $(\mathbf{1})_2^-$.

5.2 Electrochemistry

Previous studies predict electronic communication in reduced states of **1**, based on symmetry allowed interactions of the cluster dπ system with pyridine π* orbitals.[17-19] Anodic reactions are found to be reversible one-electron processes in all cases, irrespective of solvent polarity and state of protonation, as shown in Figure 5-2.

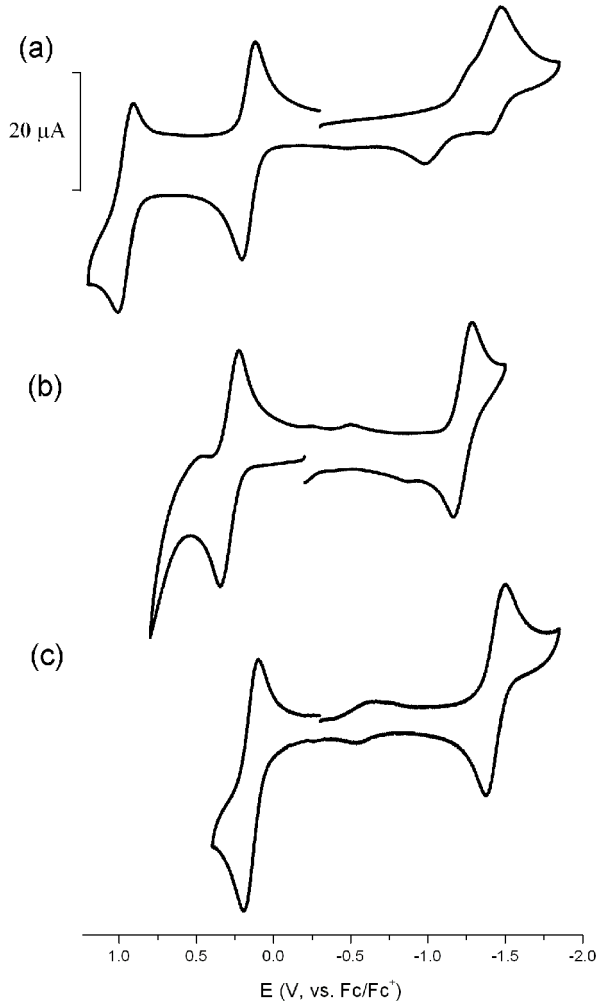

Figure 5-2. Electrochemistry of 1 mM **1** in (a) CH_2Cl_2, (b) DMSO and (c) the deprotonated Bu_4N^+ carboxylate salt of **1** in CH_2Cl_2. All solutions contained 0.1 M Bu_4NPF_6, and used an Au WE, Pt CE, and Fc/Fc^+ REF.

Figure 5-3 shows the cathodic electrochemistry of **1** in CH_2Cl_2 and DMSO. The reduction of the protonated cluster in CH_2Cl_2 (Fig 2, red solid line) shows two waves, and the reoxidation shows two waves with a larger apparent splitting. This can be explained by an ECE mechanism where E is a one electron reduction and C is a reversible dimerization. Reduced cluster $\mathbf{1}^-$ reacts with neutral **1** in the diffusion layer to form a mixed-valence dimer $(\mathbf{1})_2^-$ which can then be reduced again to form a doubly reduced dimer $(\mathbf{1})_2^{2-}$, giving two reduction waves. This dimer is then reoxidized in two one electron steps split symmetrically about the half wave potential of the monomer, resulting in waves of approximately half the peak current of the one electron cluster oxidations seen at positive

potentials. The neutral dimer falls apart to yield the neutral monomer **1**. Consistent with a dimerization step, the use of a solvent known to disrupt hydrogen bonding (DMSO, Figure 5-3, black dashed line) or use of the deprotonated cluster (Bu_4N^+ carboxylate salt, Figure 5-2) results in a single reversible cathodic process with peak currents comparable to the anodic waves.

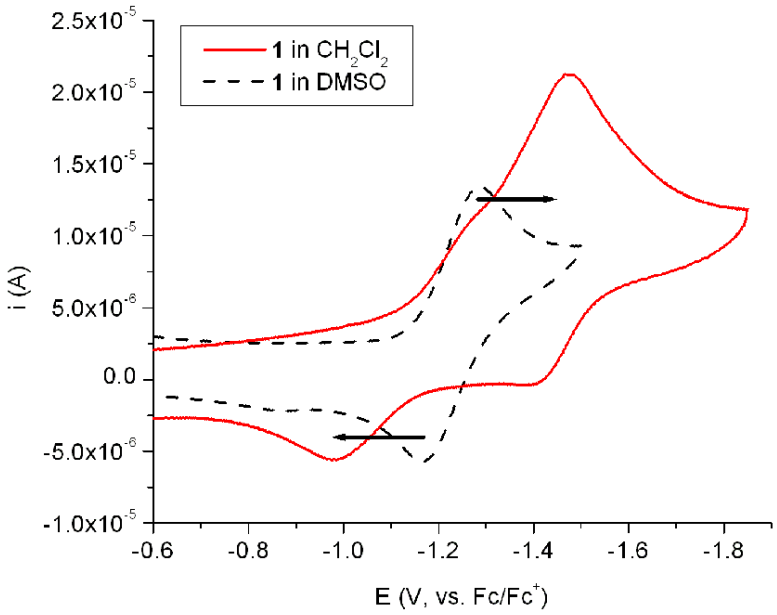

Figure 5-3. Cathodic electrochemistry of **1** in CH_2Cl_2 (red solid line) and DMSO (black dashed line), with arrows to indicate splitting of the reduction upon dimerization. ~1 mM with 0.1 M Bu_4NPF_6, Au WE, Pt CE, and Fc/Fc^+ REF.

5.3 Measurement of diffusion coefficients and hydrodynamic radii to distinguish monomers from dimers

The assignment of neutral **1** as a monomer and the reduced states as dimers is supported by diffusion coefficients measured by rotating disk voltammetry measurements on **1** and diffusion ordered NMR spectroscopy (DOSY) on neutral and reduced states of **1**. No neutral dimer is detected by IR, NMR, or rotating disk electrochemistry at millimolar concentrations in MeCN or CH_2Cl_2 supporting a $K_{dim} < 0.01$ for **1**.

Using a rotating glassy carbon disk electrode, anodic linear sweep voltammograms of **1** were recorded at a scan rate of 100 mV/s and rotation rates of 200-2000 rpm. The oxidation displayed Levich-Koutecky behavior, with D_0 = 1.12(6) x 10^{-7} cm^2 s^{-1} in CH_2Cl_2 and 1.46(6) x 10^{-7} cm^2 s^{-1} in MeCN. For comparison, a triruthenium cluster with one carbonyl and two pyridine ligands gave D_0 = 9.9(4) x 10^{-8} cm^2 s^{-1} in CH_2Cl_2 and 1.19(7) x 10^{-7} cm^2 s^{-1} in MeCN.

1, $(\mathbf{1})_2^-$, and $(\mathbf{1})_2^{2-}$ were characterized by DOSY at -20 ºC in CD_3CN and hydrodynamic radii were determined by comparison of the measured diffusion coefficients with a ferrocene internal standard to obviate the differences in solution viscosity between samples. Table 5-1 shows the ratios of diffusion coefficients, the corresponding hydrodynamic radii, and crystallographic or calculated (DFT) radii. The assumption made here is that the differences between the crystallographic radii and hydrodynamic radii are small (as in the known values r_H = 0.32 nm and r_{xtal} = 0.29 nm for ferrocene) and sample independent. The calculated radii in the table are spherical for Fc and **1**. Perrin's oblate spheroid formalism[20] is used for the distinctly non-spherical dimers, and the predicted radius is 0.73 nm, instead of 0.63 nm obtained using a spherical model.

Table 5-1. Ratios of diffusion coefficients and experimental and calculated hydrodynamic radii.

Species	**D/D_{Fc}**	**r_{DOSY} (nm)**	**$r_{xtal/calc}$ (nm)**
Ferrocene	1	n/a	0.29
1	0.59	0.49	0.50
$(\mathbf{1})_2^-$	0.34	0.83	0.73
$(\mathbf{1})_2^{2-}$	0.31	0.93	0.73

While not necessarily related to dimerization, another measure of thermodynamic stability, the comproportionation constant, can be calculated from the splitting in the reoxidation waves of $(\mathbf{1})_2^{2-}$. $K_c \sim 10^7$ for the mixed valence ion in CH_2Cl_2 at 100 mV/s scan rates indicating a highly stable mixed valence ion with respect to disproportionation. Significant contributions are expected from both electrostatic and electronic structure factors.[21]

5.4 Spectroelectrochemistry

The electronic structures of the three oxidation states were probed by infrared and UV/vis/near IR spectroelectrochemistry, shown in Figure 5-4. Figure 5-4(a) shows the ν(CO) region of the infrared. The neutral cluster shows the usual band at 1945 cm^{-1}, and a fully reduced sample shows a single band at 1900 cm^{-1} with the usual shift seen for a single reduction of a carbonyl substituted $Ru_3O(OAc)_6$ cluster. A half reduced sample shows a slight shift for the "neutral" band to about 1940 cm^{-1}, consistent with an increase in pyridine donor ability upon dimerization with a reduced cluster, but otherwise simply a superposition of the neutral and reduced species. This confirms an electron-localized structure, with an upper bound on the electron transfer rate constant (k_{ET}) of ~10^{10} s^{-1}.

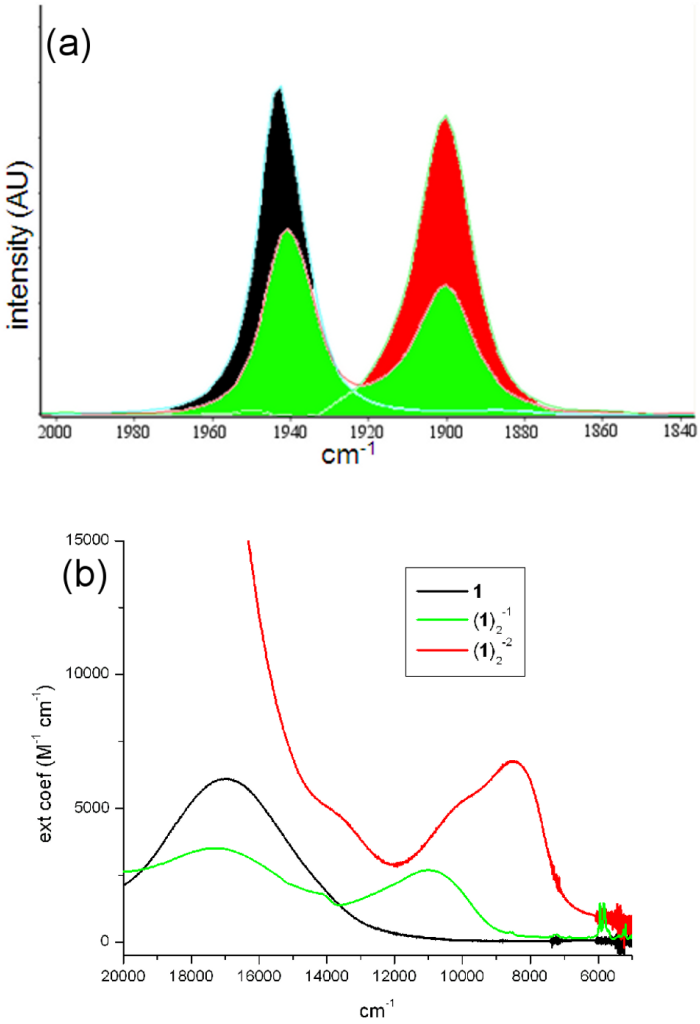

Figure 5-4. IR and UV/vis/NIR spectra of **1**, 3 mM in MeCN, -20 ºC. (a) ν(CO) region of the infrared, showing electron localization on the IR timescale in the singly reduced mixed valence dimer (green). (b) UV/vis/NIR, showing a distinct electronic structure for the mixed valence dimer (green).

Figure 5-4(b) shows UV/vis/NIR spectra obtained as **1** is stepped through two one-electron reductions, with equivalent results obtained by either chemical or electrochemical reduction. The fully reduced cluster spectrum (red line) is similar to other reduced carbonyl substituted triruthenium clusters,[22-23] with several bands evident between 7000-12000 cm^{-1}, and an increase in intensity and blue shift of the intracluster band observed at 588 nm (17000 cm^{-1}) in the neutral species. The monoanionic species identified as $(\mathbf{1})_2^-$ exhibits an unusual spectral response, not simply the

superposition of neutral and fully reduced spectra that might be expected in view of the simple weighted average of neutral and reduced ν(CO) bands in the infrared spectra in Figure 5-4(a). The intracluster absorption decreases in intensity, as is seen in singly reduced dimers of triruthenium clusters bridged by pyrazine or 4-4'-bipyridine,[22] but the near-IR shows an absorption profile at much higher energy than the fully reduced dimer with a ν_{max} of 11000 cm^{-1} (green trace) instead of 8500 cm^{-1} (red trace). Several possible explanations for the mixed valence electronic structure merit immediate discussion: orbital destabilization due to electron-electron repulsion, an exciton shift, a non-Gaussian Marcus-Hush intervalence charge transfer (IVCT) band and a hypsochromic shift of the cluster-to-ligand charge transfer (CLCT) transitions due to stabilization of the ground state.

Red shifts upon sequential reduction similar in appearance to those in Figure 5-4(b) have been observed in CLCT transitions of trispyridyl triruthenium clusters.[24] This was attributed to destabilization of occupied cluster orbitals by increasing electron-electron repulsion. Applying this explanation to $(\mathbf{1})_2^{-/2-}$ would require sequential population of a single molecular orbital, and thus a delocalized Robin-Day Class III classification.[9] The IR spectra preclude a delocalized electronic structure (Fig. 5-4(a)) and thus electronic occupancy as an explanation for the band positions in $(\mathbf{1})_2^-$ and $(\mathbf{1})_2^{2-}$.

An exciton shift might be invoked for $(\mathbf{1})_2^{2-}$ as a dimer of chromophores,[25] relative to $(\mathbf{1})_2^-$. However the exciton splitting falls off as the cube of the distance between the dipole moment centers[26-27] (~14 Å for these dimers) and is calculated to be on the order of 50 cm^{-1} for these species, more than an order of magnitude lower than the observed 2500 cm^{-1} shift.

If the mixed valence dimer $(\mathbf{1})_2^-$ is moderately coupled and fits solidly in the Robin-Day Class II regime, a distinct electronic signature is expected in lieu of a weighted average of the neutral and doubly reduced spectra. This has been observed in a mixed valence hydrogen bonded assembly.[10] When the non-Gaussian absorption profile in the near-IR spectrum of $(\mathbf{1})_2^-$ is treated as a single IVCT transition, the electronic coupling, H_{ab}, and the total reorganization energy, λ, can be extracted using the measured transition dipole moment and Marcus-Hush theory.[1, 28-29] Such treatment gives H_{ab} = 370 cm^{-1} and λ = 11000 cm^{-1} using a Ru-Ru distance of 14 Å for the electron

transfer distance r_{ab}. The reorganization energy is in very good agreement with thermodynamic estimates for 0/- couples of triruthenium clusters.[17, 30] The predicted linewidth at half-max is 4650 cm^{-1}, wider than the observed $\Delta\nu_{1/2}$ of 3600 cm^{-1}. However, the *half*-width at half max on the high energy side is 2325 cm^{-1}, half the predicted bandwidth. H_{ab}/λ = 3% appears too small to justify narrowing of an IVCT band, but H_{ab} may actually be larger if the electron transfer distance r is shorter than the Ru-Ru intercluster distance. The main problem with this line of reasoning is that it cannot explain the disappearance of the CLCT transitions from the cluster to the pyridine and isonicotinic acid ligands observed in $(\mathbf{1})_2^{2-}$ and in other anionic clusters of this type.

If the near IR absorption profile in $(\mathbf{1})_2^{-}$ is indeed two CLCT transitions (e.g. cluster-to-pyridine and cluster-to-isonicotinic acid) as it is in $(\mathbf{1})_2^{2-}$, the large hypsochromic shift can be explained as a stabilization of the ground state by mixed valency across hydrogen bonds. Stabilization of ground states by hydrogen bonding or ion pairing is well known,[31-33] but the effect is not evident in the fully reduced species $(\mathbf{1})_2^{2-}$, confirmed as a dimer by diffusion NMR experiments. This means that the combination of hydrogen bonding and mixed valency stabilizes the ground state of $(\mathbf{1})_2^{-}$ by ~2500 cm^{-1} (or 7.1 kcal/mol, or 310 meV).

5.5 Conclusions

$(\mathbf{1})_2^{-}$ is the best characterized system to date for exploration of proton-dependent or proton-coupled mixed valency, where in the latter case the electron transfer depends explicitly on the proton coordinate. The large apparent stabilization of ~7 kcal/mol from the combination of mixed valency and hydrogen bonding is enticing, and begs for future work on larger self-assembled systems, as well as measurement of the electron transfer rate constant. The following chapter describes the solvent dependence of electrochemistry and electronic spectroscopy, variation of the electron donating ability of the ancillary pyridine ligand, and deuteration of the pyridine carboxylic acid. This work begins to illuminate the behavior of hydrogen bonded systems subjected to repeated electron transfer, as well as stabilization of the hydrogen bonds by electron exchange.

5.6 Experimental

General. All chemicals were used as received unless otherwise noted. CD_3CN was distilled under nitrogen from CaH_2. Electrochemistry and spectroscopy solvents were sparged with argon and dried over alumina. Elemental analysis was performed by Numega Resonance Labs in San Diego, CA.

Synthesis and characterization. Complex **1** was synthesized by the usual methods, except that it was purified by reprecipitation instead of chromatography. $Ru_3O(OAc)_6(CO)(pyridine)(H_2O)$[19, 22] (118 mg, 0.148 mmol) was stirred in 40 mL CH_2Cl_2 and 10 mL MeOH in an ice bath. Isonicotinic acid (190 mg, 1.54 mmol) was added as a solid over three minutes, and the reaction was allowed to come to room temperature slowly and stirred for 48 hours. It gradually turned from blue to teal in color. The reaction was rotavapped at 35 ºC. The residue was taken up in unstabilized CH_2Cl_2 and filtered through celite to remove excess isonicotinic acid. The solvent was reduced to a minimum, and the product was precipitated with excess hexanes, and collected on a frit. It was washed several times with hexanes, and dried on the frit overnight covered by a rubber stopper for a typical yield of 80% of blue-green solid. If the compound degraded (as was observed over a matter of months of storage in a desiccator) it could be repurified by similar methods.

^{1}H NMR (500 MHz, DMSO-d_6): δ ppm 9.00 (d, J = 6.30 Hz, 2 H), 8.96 (d, J = 4.58 Hz, 2 H), 8.57 (d, J = 6.30 Hz, 2 H), 8.35 (t, J = 8.02 Hz, 1 H), 8.22 (td, J = 6.30 Hz, 2 H), 1.94 (s, 6 H), 1.93 (s, 6 H), 1.72 (s, 6 H). UV/vis (CH_2Cl_2) nm (ε $M^{-1}s^{-1}$) 354 (5200), 408 (5100), 588 (6200). IR (KBr) cm^{-1} 3441 (br), 1950, 1736, 1716 (sh), 1609, 1573, 1449 (sh), 1424, 1349, 690.ESI MS (neg. mode) m/z calc. (**1**-H^+)$^-$ 903.8, found 903.5, (**1**)$_2^-$ calc 1807.7, found 1808.0. Elemental analysis: Calc. for $Ru_3O(OAc)_6(CO)(py)(4nic)$ $C_{24}H_{28}N_2O_{16}Ru_3$ C 31.90; H 3.12; N 3.10. Found 32.24; 3.23; 2.97.

Spectroscopy. UV/vis/NIR data were collected on a Shimadzu UV-3600 UV/vis/NIR spectrometer and infrared spectra were collected on a Bruker Equinox 55 FTIR spectrometer. Infrared spectroelectrochemistry was performed in a custom built reflectance cell,[34] and UV/vis/NIR

SEC was performed in a cell based on a published design,[35] but sealed in a quartz cuvette with a septum, with wires threaded through the top. Reduced samples were not stable at room temperature.

Electrochemistry. Electrochemistry was performed with a BAS Epsilon potentiostat in dried deoxygenated CH_2Cl_2 or DMSO with 0.1 M tetrabutylammonium hexafluorophosphate (TBAH, recrystallized from MeOH and dried under vacuum at 80 ºC) and 0.5-3 mM sample concentrations at a scan rate of 100-500 mV/s in a dedicated glovebox. The working electrode was a gold disk (1.6 mm diameter). The counter electrode was a platinum wire, and the reference was the ferrocene/ferrocenium couple.

Rotating disk electrochemistry. 75 mL of a solution (0.49 mM in **1**, 0.1 M in Bu_4NPF_6) was placed in a reactor. A freshly polished glassy carbon rotating disk electrode, 28 mm diameter, was lowered into the solution, and a platinum wire counter electrode and a silver wire pseudo-reference were placed in the solution through other openings in the reactor. Anodic linear sweep voltammograms were recorded at a scan rate of 100 mV/s and rotation rates of 200-2000 rpm.

^{1}H DOSY – Diffusion Ordered Spectroscopy. A 1.6 mM solution of **1** in CD_3CN (distilled from CaH_2) was prepared in a nitrogen filled glove box. A small amount of ferrocene was added as an internal diffusion standard. About half of the solution was pipetted into a second vial, and reduced with decamethylcobaltocene. As the reduced solution degrades at room temperature, it was quickly mixed in varying proportions with the neutral solution, sealed in NMR tubes, taken out of the box, and cooled on dry ice to retard degradation.

DOSY spectra were collected on a JEOL 500 MHz instrument, with 16384 points per scan, 16 scans for each gradient, and 32 gradient amplitudes ranging from 30 mT/m to 250 mT/m. Data was analyzed with the “continuous” mode (i.e. not a fixed number of discrete species) in JEOL Delta software, and diffusion coefficients for the ruthenium clusters were calculated by comparison with ferrocene. Both neutral **1** and the fully reduced dimer $(\mathbf{1})_2^{2-}$ gave narrow diamagnetic lineshapes. This is expected for **1**, as the HOMO for such clusters is a singly degenerate delocalized orbital. The possibility of anti-ferromagnetic coupling will be investigated in subsequent studies.

Calculation of H_{ab}. The transition dipole moment $|\mu_{12}|$ = 2.28 D for the near-IR absorption of $(\mathbf{1})_2^-$ was calculated by integrating the area under a plot of the reduced extinction coefficient, $\varepsilon(\nu)/(\nu)$. The area was measured by fitting to several Gaussian bands in Origin 6.0 and summing the area of the peaks, excluding the peak required to fit the higher energy band at ~17000 cm^{-1}. H_{ab} = 370 cm^{-1} was then calculated from $H_{ab} = |\mu_{12}| * \nu_{max}/(e * r_{ab})$ using for r_{ab} the calculated intercluster distance of 14 Å. λ was taken to be ν_{max}. The predicted width was calculated from $\Delta\nu_{1/2}^{o} = [16RTln2(\lambda)]^{1/2}$ = 4650 cm^{-1} (remembering that T = -20 ºC). $\Gamma = 1-(\Delta\nu_{1/2}/\Delta\nu_{1/2}^{o})$ and is predicted to be between 0 and 0.5 for moderately coupled Class II systems. For $(\mathbf{1})_2^-$, with $\Delta\nu_{1/2}$ = 3600 cm^{-1} and $\Delta\nu_{1/2}^{o}$ = 4650 cm^{-1}, Γ = 0.22, with "narrowing" on the low energy side.[1, 28-29] The half-width at half max for the high energy side is 2325 cm^{-1}, nearly exactly half the predicted value.

Note: Much of the material for this chapter comes directly from a manuscript entitled "Mixed valency across hydrogen bonds" by John C. Goeltz and Clifford P. Kubiak, which has been published in *Journal of the American Chemical Society,* **2010,** *132,* 17390-17392. http://dx.doi.org/10.1021/ja108841k The dissertation author is the primary author of this manuscript.

5.7 References

1. Brunschwig, B. S.; Creutz, C.; Sutin, N., *Chem. Soc. Rev.* **2002,** *31*, 168-184.
2. Lebeau, E. L.; Binstead, R. A.; Meyer, T. J., *J. Am. Chem. Soc.* **2001,** *123*, 10535-10544.
3. Cukier, R. I.; Nocera, D. G., *Annu. Rev. Phys. Chem.* **1998,** *49*, 337-369.
4. Derege, P. J. F.; Williams, S. A.; Therien, M. J., *Science (USA)* **1995,** *269*, 1409-1413.
5. Mayer, J. M., *Annu. Rev. Phys. Chem.* **2004,** *55*, 363-390.
6. Sjodin, M.; Styring, S.; Akermark, B.; Sun, L. C.; Hammarstrom, L., *J. Am. Chem. Soc.* **2000,** *122*, 3932-3936.
7. Hammes-Schiffer, S., *Acc. Chem. Res.* **2001,** *34*, 273-281.
8. Marcus, R. A., *Annu. Rev. Phys. Chem.* **1964,** *15*, 155.
9. Robin, M. B.; Day, P., *Adv. Inorg. Chem. Radiochem.* **1967,** *10*, 247.

10. Sun, H.; Steeb, J.; Kaifer, A. E., *J. Am. Chem. Soc.* **2006,** *128*, 2820-2821.

11. Hsu, T. L. C.; Engebretson, D. S.; Helvoigt, S. A.; Nocera, D. G., *Inorg. Chim. Acta* **1995,** *240*, 551-557.

12. Papoutsakis, D.; Kirby, J. P.; Jackson, J. E.; Nocera, D. G., *Chem. Eur. J.* **1999,** *5*, 1474-1480.

13. Sessler, J. L.; Sathiosatham, M.; Brown, C. T.; Rhodes, T. A.; Wiederrecht, G., *J. Am. Chem. Soc.* **2001,** *123*, 3655-3660.

14. Kurlancheek, W.; Cave, R. J., *J. Phys. Chem. A* **2006,** *110*, 14018-14028.

15. Betts, J. N.; Beratan, D. N.; Onuchic, J. N., *J. Am. Chem. Soc.* **1992,** *114*, 4043-4046.

16. Goeltz, J. C.; Kubiak, C. P., *J. Am. Chem. Soc* **2010,** *132*, 17390-17392.

17. Goeltz, J. C.; Benson, E. E.; Kubiak, C. P., *J. Phys. Chem. B* **2010**, ASAP.

18. Goeltz, J. C.; Hanson, C. J.; Kubiak, C. P., *Inorg. Chem.* **2009,** *48*, 4763-4767.

19. Salsman, J. C.; Ronco, S.; Londergan, C. H.; Kubiak, C. P., *Inorg. Chem.* **2006,** *45*, 547-554.

20. Perrin, F., *J. Phys. Radium* **1936,** *7*, 1-11.

21. Richardson, D. E.; Taube, H., *Coord. Chem. Rev.* **1984,** *60*, 107-129.

22. Ito, T.; Hamaguchi, T.; Nagino, H.; Yamaguchi, T.; Kido, H.; Zavarine, I. S.; Richmond, T.; Washington, J.; Kubiak, C. P., *J. Am. Chem. Soc.* **1999,** *121*, 4625-4632.

23. Abe, M.; Sasaki, Y.; Yamada, Y.; Tsukahara, K.; Yano, S.; Yamaguchi, T.; Tominaga, M.; Taniguchi, I.; Ito, T., *Inorg. Chem.* **1996,** *35*, 6724-6734.

24. Baumann, J. A.; Salmon, D. J.; Wilson, S. T.; Meyer, T. J.; Hatfield, W. E., *Inorg. Chem.* **1978,** *17*, 3342-3350.

25. Kobayashi, N.; Lam, H.; Nevin, W. A.; Janda, P.; Leznoff, C. C.; Lever, A. B. P., *Inorg. Chem.* **1990,** *29*, 3415-3425.

26. Kasha, M., *Radiat. Res.* **1963,** *20*, 55-71.

27. Osuka, A.; Maruyama, K., *J. Am. Chem. Soc.* **1988,** *110*, 4454-4456.

28. D'Alessandro, D. M.; Keene, F. R., *Chem. Rev.* **2006,** *106*, 2270-2298.

29. D'Alessandro, D. M.; Keene, F. R., *Chem. Soc. Rev.* **2006,** *35*, 424-440.

30. Londergan, C. H.; Salsman, J. C.; Lear, B. J.; Kubiak, C. P., *Chem. Phys.* **2006,** *324*, 57-62.

31. Rodionova, G. N.; Krutovskaya, I. V.; Rodionov, A. N.; Tuchin, Y. G.; Karpov, V. V., *J. Appl. Spec.* **1980,** *32*, 344-348.

32. Piotrowiak, P.; Kobetic, R.; Schatz, T.; Strati, G., *J. Phys. Chem.* **1995,** *99*, 2250-2253.

33. Skoog, D. A.; Holler, J. F.; Nieman, T. A., *Principles of Instrumental Analysis*. 5th ed.; Harcourt Brace and Company: Orlando, 1998.

34. Zavarine, I. S.; Kubiak, C. P., *J. Electroanal. Chem.* **2001,** *495*, 106-109.

35. Krejcik, M.; Danek, M.; Hartl, F., *J. Electroanal. Chem.* **1991,** *317*, 179-187.

Chapter 6

Mixed valency across hydrogen bonds: a more complete description

6.1 Introduction

Noncovalent interactions are often implicated in both assembly and electron transfer in natural systems,[1-6] but very few synthetic systems are available to probe the intersection of the two, particularly for ground state electron transfer of mixed valency.[7-10] The previous chapter left us with an intriguing but incomplete picture of mixed valency across hydrogen bonds. It laid out a single complex that displayed some very interesting behavior in a wide range of experiments but left us without a measure of the electronic coupling (H_{ab}) or the electron transfer rate constant (k_{ET}). This chapter attempts to fill in the gaps by systematic variation of the cluster ancillary ligands and the solvents, and by playing a few tricks in the NMR spectrometer.

Complexes **1**-**3** (Figure 6-1) allow insight into hydrogen bonds as a bridge for electron transfer by comparison with the well understood electron transfer in systems such as **4**-**7**. Reduced states of **4**-**7** have significant electron density in pyridyl π^* orbitals, resulting in fast inter- (**4**-**6**) and intramolecular (**7**) electron transfer rate constants for relatively large reorganization energies ($\lambda \sim 11000\ cm^{-1}$) in the 0/- couples.[11-16] Electron density is also expected on pyridyl π^* systems of **1**-**3**, but additional spectroscopic and electrochemical behaviors may be attributed to hydrogen bonding from the isonicotinic acid ligand.

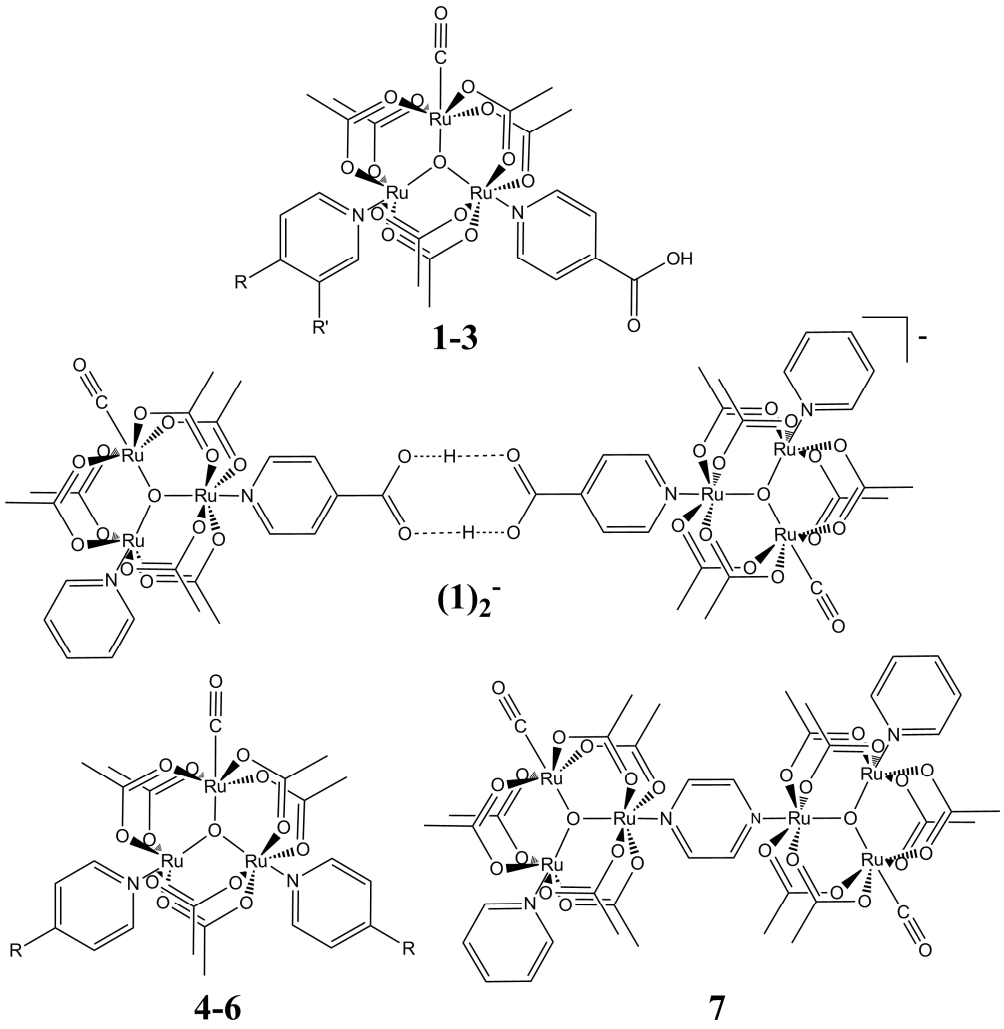

Figure 6-1. Structures of ruthenium clusters discussed in this chapter. R = H, R' = H in complex **1**, R = (dimethyl)amino, R' = H in complex **2**, and R = H, R' = F in complex **3**. Complex $(\mathbf{1})_2^-$ is a mixed valence hydrogen bonded dimer. Also shown are the previously studied clusters **4-6** and dimer of clusters **7**. R = cyano in complex **4**, R = H in complex **5**, and R = (dimethyl)amino in complex **6**.

The behavior of **1** was discussed in the previous chapter,[17] but systematic studies of ancillary pyridine ligand and solvent dependence were needed to fully understand the mixed valency and the hydrogen bonding evident in spectroscopic and electrochemical results. Briefly, **1** was found to dimerize upon one or two electron reduction in MeCN to form a mixed valence singly reduced dimer, $(\mathbf{1})_2^-$, and a doubly reduced dimer $(\mathbf{1})_2^{-2}$ based on diffusion coefficients measured by diffusion ordered NMR spectroscopy (DOSY). Electron transfer in the mixed valence dimer was slow on the

IR timescale ($<10^{10}$ s^{-1}) but the electronic absorptions in the near-IR were ~2500 cm^{-1} higher in energy than those of the doubly reduced dimer. Since that study, derivative **2** was synthesized using 4-(dimethyl)aminopyridine (dmap), a more electron donating pyridine and **3** with 3-fluoropyridine, allowing for ^{19}F NMR experiments.

This chapter describes the electrochemical and spectroscopic behavior of **1** - **3** in several solvents, as well as an attempt to estimate of the intramolecular rate constant by NMR. Unfortunately but not unexpectedly,[18] the measurement of k_{ET} for the mixed valence dimer was confounded by the fact that neither of the "exchanging species" could be isolated in the NMR. Neutral dimers were not observed, and neither were any paramagnetic species not undergoing exchange. Comparing ^1H and ^{19}F spectra resulted in bracketing the electron transfer rate constant for $(\mathbf{3})_2^-$ as 1×10^3 $s^{-1} < k_{ET} < 8.6 \times 10^4$ s^{-1} in CD_3CN at -20 ºC.

6.2 Electrochemistry

The electrochemistry of $Ru_3O(OAc)_6(CO)(L)_2$ clusters has been known for some time.[12, 18-21] The donor ability of the pyridine strongly affects the oxidation and reduction potentials for **4**-**6**, with a somewhat greater effect noticeable in the reductions. This is explained by electron delocalization onto the pyridine π^* system, which is symmetry allowed in the reduced states but forbidden in the neutral and oxidized states.[11] Pyrazine bridged dimers of these clusters (e.g. **7**, Figure 6-1) exhibit strong electronic communication in cathodic electrochemistry, with $\Delta E_{1/2}$ ranging from 200-450 mV, depending on the solvent and pyridine donor ability. More electron donating pyridines increase the observed splitting, as well as the rate of electron transfer, k_{ET}, by pushing the energy of the clusters closer to that of the pyrazine bridge π^*.[15]

The anodic electrochemistry of **1** and **2** is straightforward, with two single electron oxidations visible within common solvent windows (Figure 6-2). The cathodic electrochemistry, where electronic communication might be expected, is somewhat more complicated. Two overlapping single electron waves are observed as the voltage is swept negative, and two well separated reoxidation waves are observed on returning to rest potential. This can be explained by an

ECE mechanism where E is a reversible one electron reduction and C is a reversible dimerization. Reduced cluster $\mathbf{1}^-$ reacts with neutral **1** in the diffusion layer to form a mixed-valence dimer $(\mathbf{1})_2^-$ which can then be reduced again to form a doubly reduced dimer $(\mathbf{1})_2^{2-}$, giving two reduction waves. This dimer is then reoxidized in two one electron steps split symmetrically about the half wave potential of the monomer, resulting in waves of approximately half the peak current of the one electron cluster oxidations seen at positive potentials. The neutral dimer falls apart to yield the neutral monomer **1**. The splitting of the return waves appears quite large, on the order of 400 mV in CH_2Cl_2 at 1 mM concentration and 100 mV/s scan rate. This will be discussed in greater detail below.

The waveform is stable to repeated scanning, but is highly solvent, concentration, and scan rate dependent, and is also dependent on the protonation of the isonicotinic acid ligand. Consistent with a hydrogen bonded dimer, the use of a solvent known to disrupt hydrogen bonding (DMSO), or the prior deprotonation of the cluster results in a single reversible cathodic wave of the same peak height as the oxidation waves. Figure 6-2 shows cyclic voltammograms of (a) **1** in CH_2Cl_2, (b) **1** in DMSO, and (c) **1**-Bu_4N, the deprotonated tetrabutylammonium salt, in CH_2Cl_2.

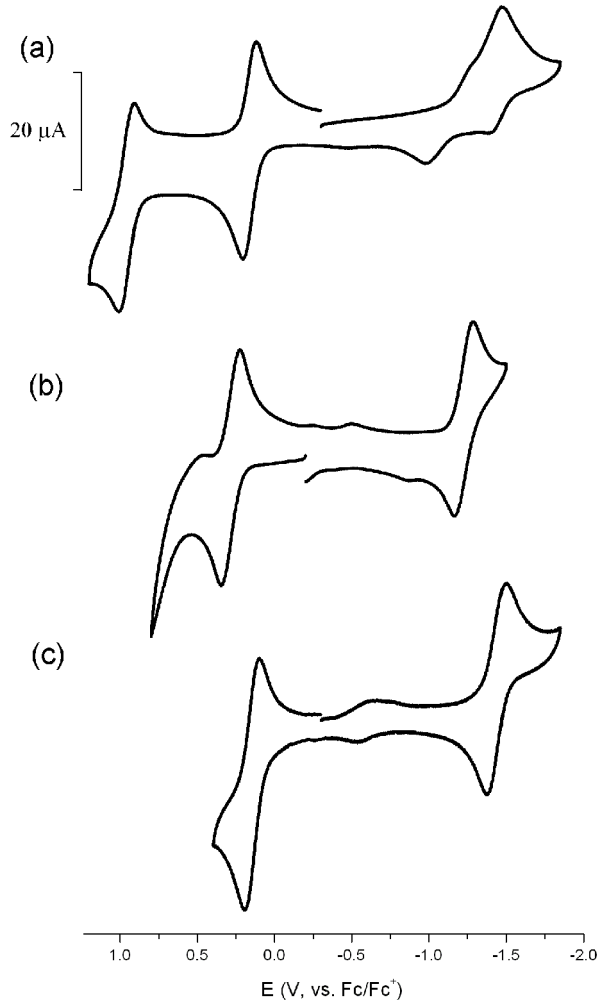

Figure 6-2. Electrochemistry of (a) **1** in CH_2Cl_2, (b) **1** in DMSO, and (c) **1**-Bu_4N, the deprotonated tetrabutylammonium salt, in CH_2Cl_2. Each sample was 1 mM with 0.1 M Bu_4NPF_6, an Au WE, Pt CE, and Fc/Fc^+ REF. The scan rate was 100 mV/s.

DMSO was the only non-aqueous solvent found to completely disrupt the dimerization of **1**. Otherwise the splitting in the reoxidation waves was dependent on the choice of solvent, the scan rate, and the concentration. Reduction potentials for 1 mM **1** or **2** at a scan rate of 100 mV/s are shown in Table 6-1. At these conditions, the splitting tracks very well with the solvent dielectric constant, indicating that solvent polarity directly affects the dimerization (see Figure 6-3). A plot of scan rate versus observed peak potential for **2** (1 mM in MeCN) is shown in Figure 6-4.

Extrapolation to a scan rate of 0 gives a $\Delta E_{1/2}$ of about 120 mV for both **1** and **2** at 1 mM concentration in MeCN.

Table 6-1. Reduction potentials in mV, versus Fc/Fc^+ for **1** and **2**, 1 mM, scan rate of 100 mV/s, with solvent dielectric constants.

Complex	Solvent	Dielectric constant	$E_{1/2}^{2+/+}$	$E_{1/2}^{+/0}$	$E_{1/2}^{0/-\ (dimer)}$	$E_{1/2}^{-/2-}$ (dimer)
1	THF	7.52	+820	+100	-1170	-1570
1	CH_2Cl_2	9.08	+971	+200	-1020	-1430
1	PhCN	25.9	+769	+90	-1200	-1520
1	DMF	36.71	n/a	+220	-1070	-1330
1	MeCN	37.5	+920	+200	-1040	-1320
1	DMSO	47.2	n/a	+290	-1220	n/a
1-Bu_4N	CH_2Cl_2	9.08	+960	+150	-1430	n/a
2	CH_2Cl_2	9.08	+790	+40	-1230	-1620
2	MeCN	37.5	+820	+220	-1080	-1364

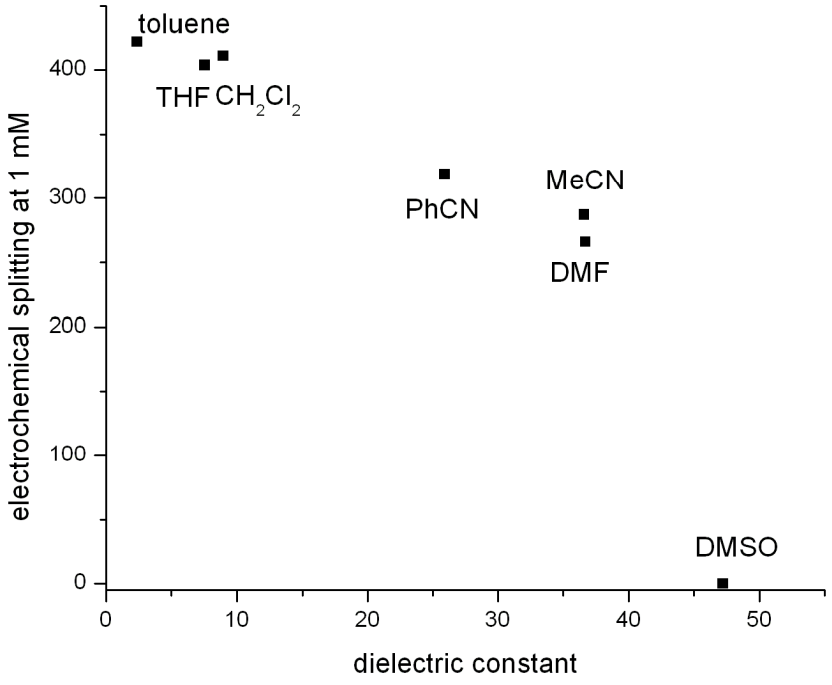

Figure 6-3. Plot of $\Delta E_{1/2}$ (in mV) for the oxidations of the doubly reduced dimer $(\mathbf{1})_2^{2-}$ at 1 mM concentration and 100 mV/s scan rate versus solvent dielectric constant.

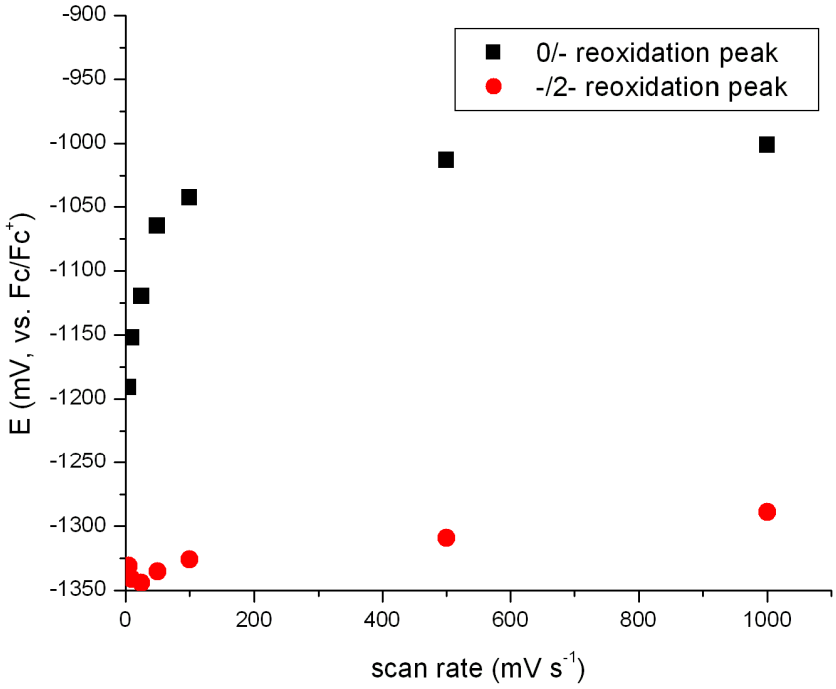

Figure 6-4. Plot of scan rate versus peak potentials for reoxidation waves of **2**, 1 mM in MeCN.

The splitting is clearly a mixture of thermodynamic and kinetic effects, though it is sufficiently complicated that digital simulation of the waves in DigiSim software has yet to yield reasonable parameters. Based on electronic spectra, *vide infra*, the thermodynamic stabilization from hydrogen bonding appears to be relatively solvent independent, so the solvent dielectric parameter is likely indicative of differences in dimerization kinetics rather than thermodynamics. This is also consistent with comparable (and small) electronic couplings in **1**-**3**, which will also be discussed in greater detail in reference to the electronic spectra.

6.3 Infrared spectroscopy

As discussed in previous chapters, the ν(CO) band is a reliable indicator of the redox state and electronic distribution in $Ru_3O(OAc)_6(CO)(L)_2$ clusters, appearing at ~1940 cm^{-1} for neutral clusters and ~1900 cm^{-1} for singly reduced clusters.[12] It has also been a useful marker for electron

transfer kinetics in pyrazine bridged dimers of Ru_3O clusters.[13-16] In the mixed valence monoanion **7**$^-$ (Figure 6-1), partial coalescence of the neutral and reduced ν(CO) bands is consistent with picosecond lifetimes for electron transfer.

With this in mind we investigated the infrared spectroelectrochemistry of the hydrogen bonded assemblies, monitoring the ν(CO) band at increasingly negative applied potentials. For both **1** and **2**, a smooth transition is observed in going from the neutral clusters to the mixed valence monoanions $(\mathbf{1})_2^-$ and $(\mathbf{2})_2^-$, then to the fully reduced dimers $(\mathbf{1})_2^{2-}$ and $(\mathbf{2})_2^{2-}$. Data for **1** in MeCN at -20 ºC are shown in Figure 6-5. No ET behavior is visible on the IR timescale (~10^{10} s^{-1}), though the small shift of the neutral cluster ν(CO) from 1945 cm^{-1} in **1** to 1940 cm^{-1} in $(\mathbf{1})_2^-$ is consistent with the reduced cluster increasing the electron donating ability of the isonicotinic acid ligand on the neutral cluster. Similar shifts have been seen previously upon increasing the ligand donor ability, for example upon substitution of dmap for pyridine.[12] The nominally ν(CO) band for the carboxylic acid, present in the neutral complex at 1740 cm^{-1}, was not observed in any reduced state. Frustratingly, it is presumed to shift and coincide with solvent, acetate, or aromatic vibrational modes.

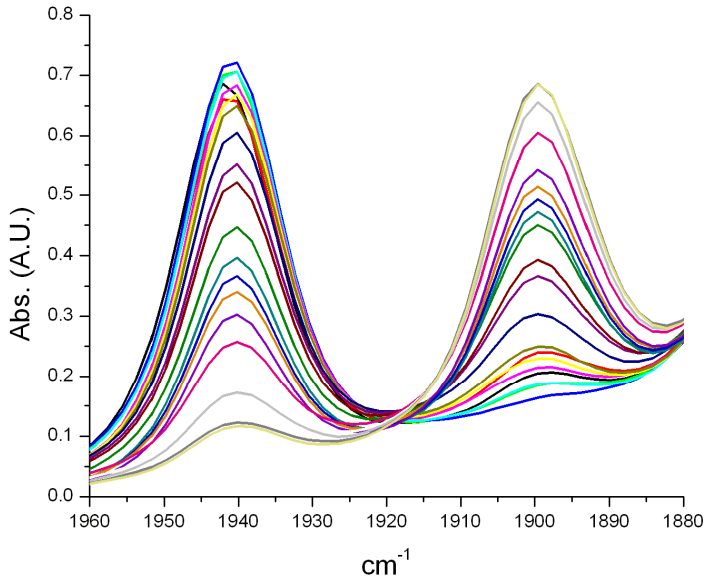

Figure 6-5. Infrared spectroelectrochemistry of **1** in MeCN at -20 ºC. Upon reduction the ν(CO) band shifts to lower energy by about 40 cm^{-1}. Complex **2** gives equivalent results. No ET kinetics are observed on this timescale.

6.4 Nuclear magnetic resonance

Electron transfer in the mixed valence species $(\mathbf{1})_2^-$ and $(\mathbf{2})_2^-$ was seen to be trapped on the infrared timescale, so kinetic information was sought in ^{1}H NMR experiments. Diffusion ordered NMR spectroscopy (DOSY) was previously used to confirm dimerization upon reduction, as discussed in chapter 5.[17] Comparison with a ferrocene internal standard (with a known hydrodynamic radius) showed that neutral **1** was monomeric, and that $(\mathbf{1})_2^-$ and $(\mathbf{1})_2^{2-}$ were dimeric.

Isolation of the pure mixed valence dimers $(\mathbf{1})_2^-$ or $(\mathbf{2})_2^-$ has thus far been unsuccessful, but a range of "oxidation states" may be probed by NMR by mixing neutral and reduced samples in various proportions in a glove box and quickly chilling them on dry ice before inserting them into the spectrometer. The aromatic regions of spectra for **1** with varied amounts of reductant in CD_3CN at -20 ºC are shown in Figure 6-6. Interestingly, both the neutral species and the doubly reduced dimer have typical narrow diamagnetic lineshapes (bottom and top traces in Figure 6-6). The electrons are

not delocalized on the IR timescale, and thus do not occupy a single orbital in the reduced dimer as discussed in the previous chapter. This suggests that the highest energy electrons in $(\mathbf{1})_2^{2-}$ are antiferromagnetically coupled, a phenomenon that might be investigated in a separate study.

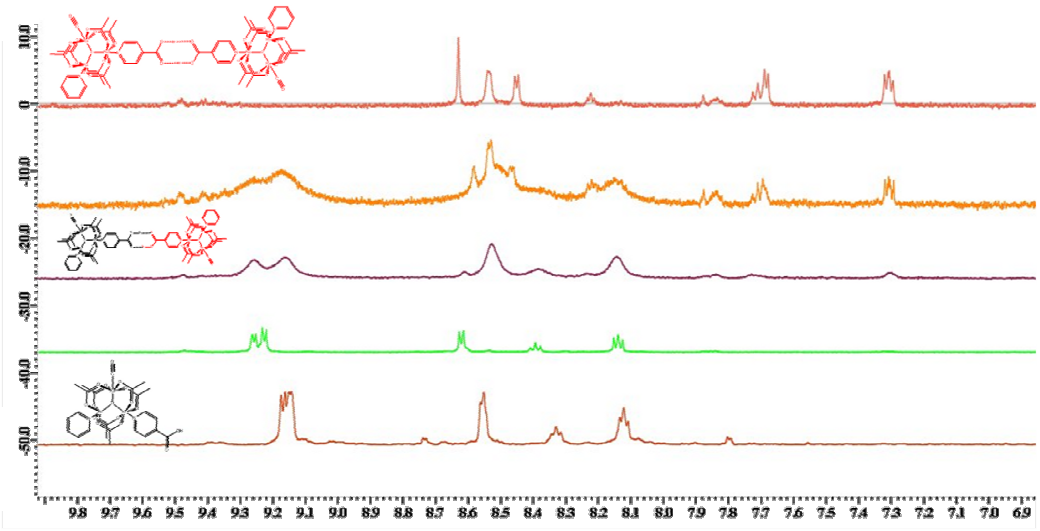

Figure 6-6. ^{1}H spectra of **1** in CD_3CN at -20 ºC with varying amounts of the reductant decamethylcobaltocene. The bottom trace is neutral **1**, the middle trace (purple) is nearly pure $(\mathbf{1})_2^-$ and the top trace is fully reduced $(\mathbf{1})_2^{2-}$ with an excess of reductant.

Meyer et al. attempted a similar experiment with a pyrazine bridged dimer similar to **7** but with pyridine ligands in places of the carbonyl ligands.[18] Their determination of k_{ET} was confounded by multiple competing equilibria on comparable timescales, as is ours. Electron transfer in the mixed valence species $(\mathbf{1})_2^-$ appears to be in the fast regime, as a single set of broadened pyridyl peaks is observed for the main species (purple trace, middle of Figure 6-6). They are close in position to the peaks of the neutral species, and if ET is truly in the fast regime, then the positions should be averages of the diamagnetic and paramagnetic contributions. The paramagnetic species thus has very similar chemical shifts and it would not take very fast exchange to average the peaks and yield the observed spectra. Simulation with WinDNMR gives a minimum k_{ET} on the order of 1000 s^{-1} for peaks 100 Hz apart to give a single peak with a width of about 25 Hz, as observed.[22] Unfortunately

the rate constant could be as high as 10^9 s^{-1} and still be consistent with the observed NMR and IR spectra.

As a range of 6 orders of magnitude of possible rate constants is somewhat unsatisfying, complex **3** was synthesized to facilitate ^{19}F NMR studies where the peaks might be well separated enough to be in the slow exchange regime. ^{1}H spectra for **3**, $(\mathbf{3})_2^-$ and $(\mathbf{3})_2^{2-}$ were comparable to those obtained for the pyridyl and dmap derivatives, with a single set of resonances observed for the mixed valence species and diamagnetic lineshapes for the neutral and doubly reduced species. ^{19}F spectra did indeed prove to be in the slow exchange regime, with peaks separated by almost 40 kHz (Figure 6-7).

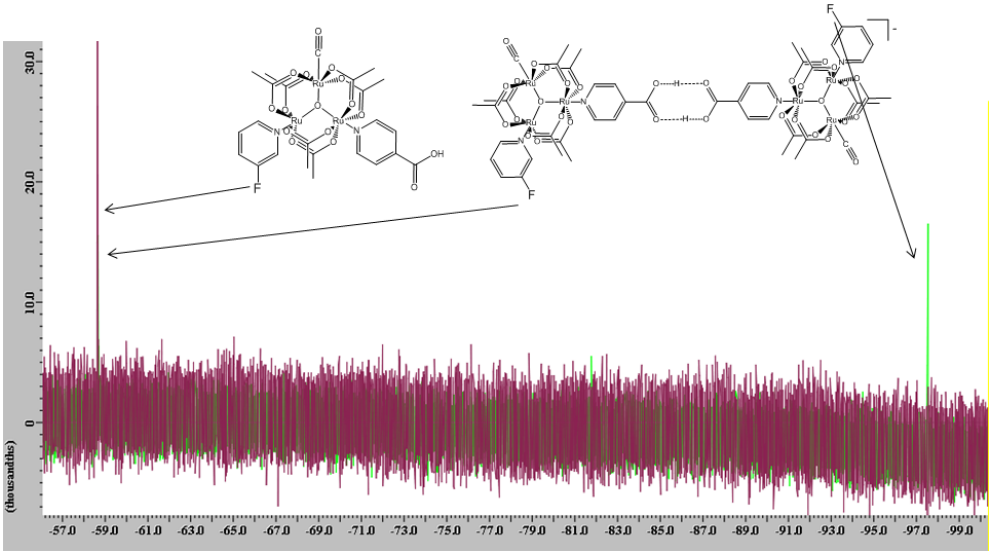

Figure 6-7. ^{19}F NMR spectra for **3**, and $(\mathbf{3})_2^-$ at -20 ºC in CD_3CN, with x-axis in kHz. **3** displays one resonance at ca. -58 kHz and $(\mathbf{3})_2^-$ displays 2 resonances at -58 kHz and -98 kHz, indicating slow exchange on this timescale.

The neutral complex **3** had one resonance attributed to the fluoropyridine ligand at -125 ppm (-58 kHz). The mixed valence dimer $(\mathbf{3})_2^-$ had peaks at ca. -125 ppm and -207 ppm (-98 kHz). Strangely, no peaks were observed in the fully reduced dimer $(\mathbf{3})_2^{2-}$. In all spectra, the resonance around -58 kHz was more intense and allowed easy fitting of the data. The peak displayed weak coupling to the adjacent protons in **3**, but was broadened somewhat and shifted slightly upfield in $(\mathbf{3})_2^-$. It broadened and shifted further upfield with increasing temperature (Figure 6-8). All of these

phenomena are consistent with slow exchange, giving an upper limit of 8.6 x 10^4 s^{-1} for an exchanging species not yet in the intermediate regime (coalescing to a single peak). Clearly the peaks are not close to being coalesced, so k_{ET} is likely a good deal slower than the upper bound.

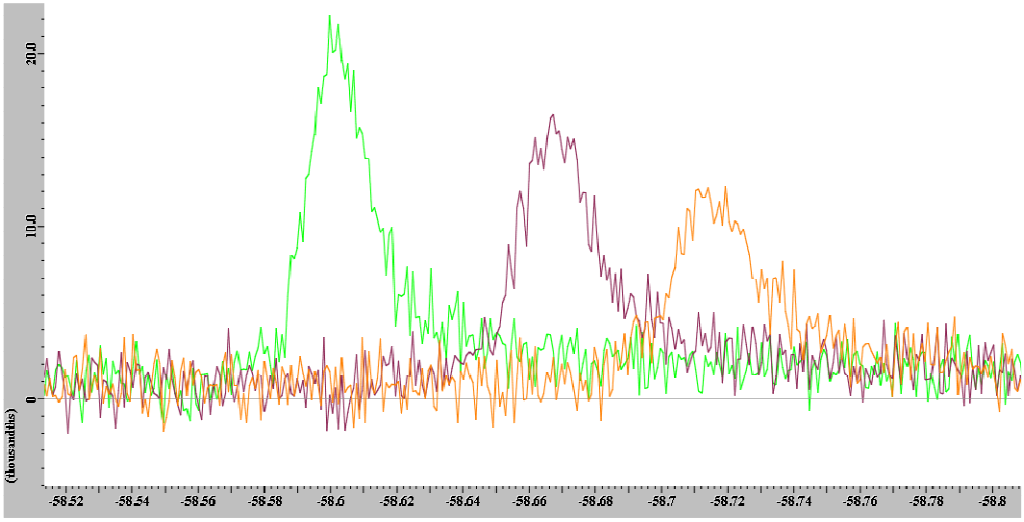

Figure 6-8. ^{19}F NMR spectra for the "neutral" resonance of $(\mathbf{3})_2^-$ at -35 ºC (left), -20 ºC (center), and -10 ºC (right) in CD_3CN, with x-axis in kHz. The peaks broaden with increasing temperature, consistent with slow exchange.

6.5 Electronic spectroscopy

The electronic spectra of **1** and **2** in various oxidation states were obtained under nitrogen at -20 ºC in acetonitrile and THF. The neutral species exhibit typical absorptions for this class of complex. The fully reduced dimers are also typical, with a broad, multi-peak near-infrared profile ranging from about 7000 – 12000 cm^{-1} corresponding to nominally cluster dπ to ligand π* MLCT transitions. The mixed valence dimers $(\mathbf{1})_2^-$ and $(\mathbf{2})_2^-$ are atypical, and exhibit a near-IR profile at much higher energy than expected. Figure 6-9 shows the electronic spectra for **1**, $(\mathbf{1})_2^-$, and $(\mathbf{1})_2^{2-}$ in MeCN.

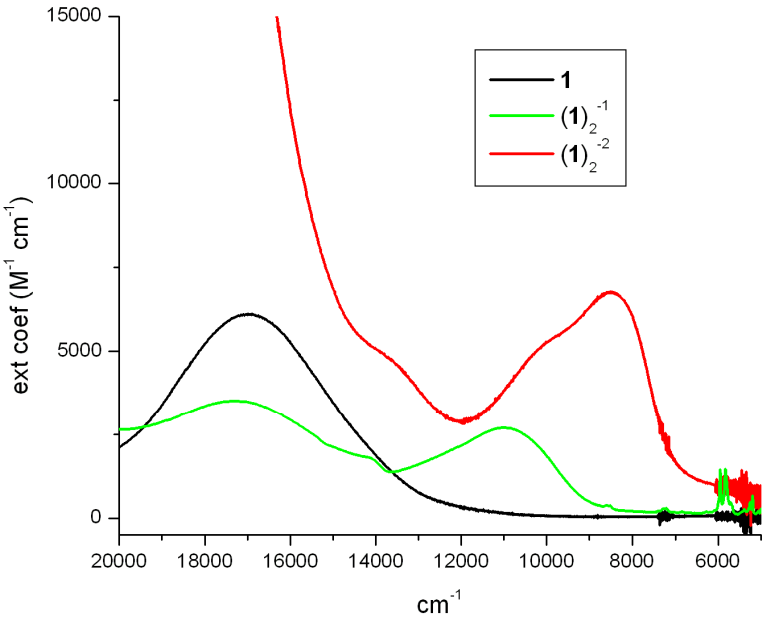

Figure 6-9. Electronic spectra for **1**, $(\mathbf{1})_2^-$, and $(\mathbf{1})_2^{2-}$ in MeCN.

The region from 18000 to 8000 cm-1 was fit to three bands for $(\mathbf{1})_2^-$ and $(\mathbf{2})_2^-$ in MeCN and THF, an intracluster transition and two MLCT transitions (see Figure 6-10 for a sample fit). The two lower energy MLCT bands for each experimental fit were summed and are presented in Figure 6-11, and band parameters are summarized in Table 6-2. The profile indicates that this region is indeed made up of multiple peaks and not an asymmetric IVCT band, as might have been expected for these moderately coupled systems.[1, 17, 23]

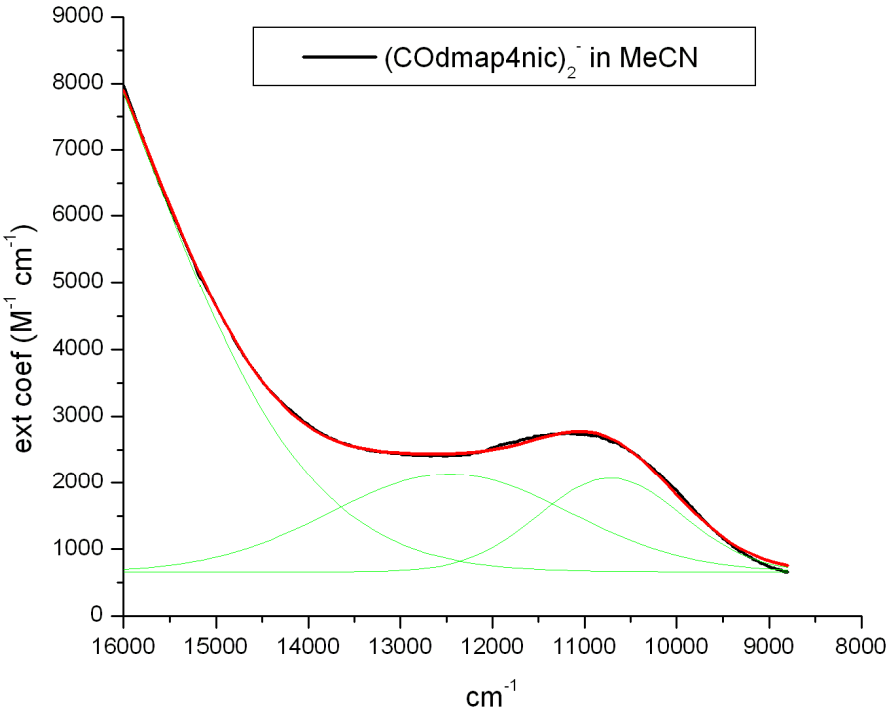

Figure 6-10. Curve fitting for UV/vis/NIR spectrum of complex $(\mathbf{2})_2^-$ in MeCN. The two lower energy bands are summed to give a representation of the NIR profiles of **1** and **2** in Figure 6-11 and Table 6-2.

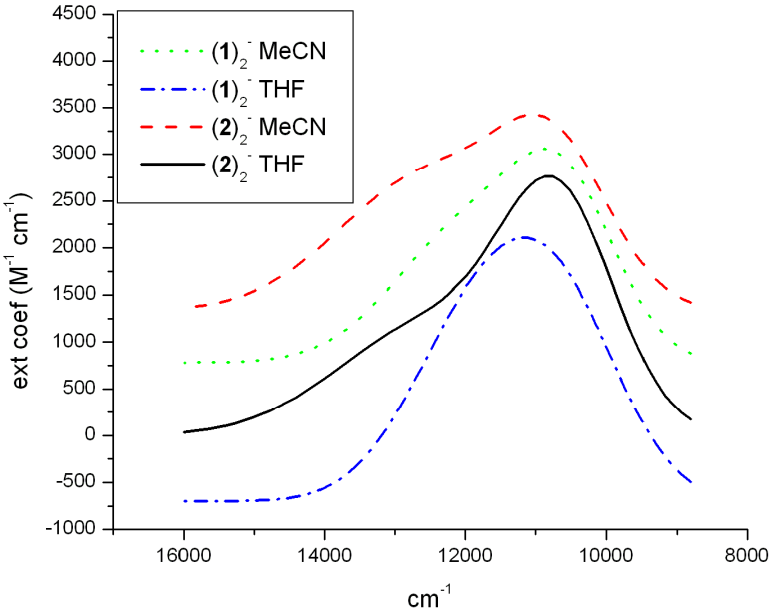

Figure 6-11. Sums of near-IR bands from curve fitting in the mixed valence dimers, offset vertically for visual clarity.

Table 6-2. Parameters found by fitting the near-IR region to two Gaussian absorption bands.

Sample	Solvent	Band 1 ν_{max} (cm^{-1})	$\nu_{1/2}$ (cm^{-1})	ε (M^{-1} cm^{-1})	Band 2 ν_{max} (cm^{-1})	$\nu_{1/2}$ (cm^{-1})	ε (M^{-1} cm^{-1})
$(\mathbf{1})_2^-$	MeCN	11900	2170	1490	10600	1440	1450
$(\mathbf{1})_2^-$	THF	11800	1920	1900	10600	1700	1660
$(\mathbf{2})_2^-$	MeCN	12500	2600	1470	10700	1550	1400
$(\mathbf{2})_2^-$	THF	12400	2700	1200	10700	1590	2230

The bands seem remarkably insensitive, changing only slightly with solvent and ligand substitution. Discussion of this phenomenon is facilitated by an understanding of electronic spectra for $\mathbf{4}^-$-$\mathbf{6}^-$. Ligand substitution leads to large changes in reduction potential and rates of intermolecular electron exchange (see chapters 1 and 3), but does not lead to large differences in the near-IR absorption profiles as shown in Figure 6-12.

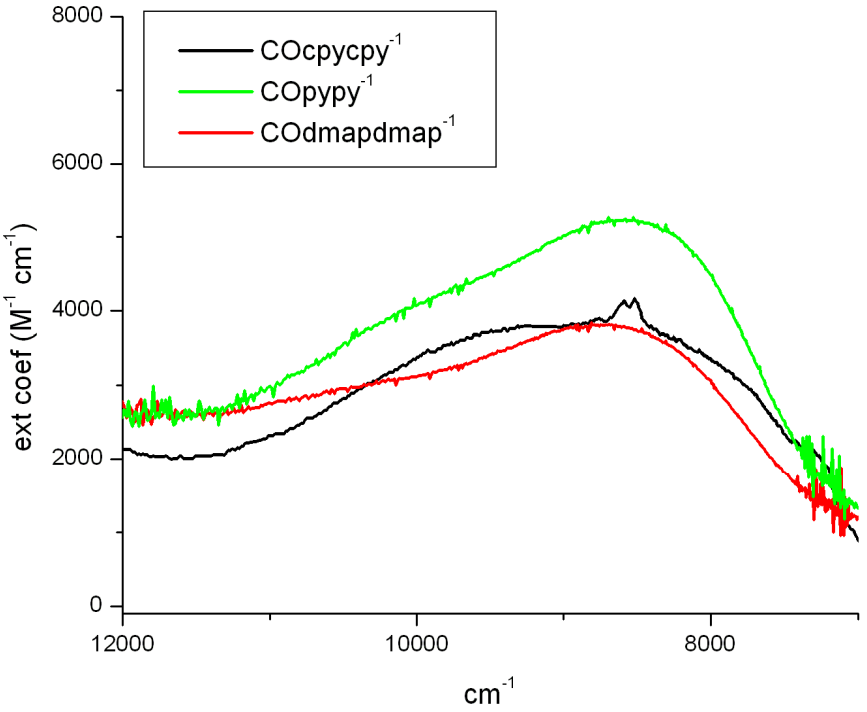

Figure 6-12. Electronic spectra for **4**$^{-}$-**6**$^{-}$ in MeCN, showing the relative insensitivity of the NIR profile of reduced "monomer" clusters to pyridine ligand substitution.

Examining molecular orbital (MO) diagrams for the clusters once again sheds light on their behavior. Figure 6-13 shows an MO diagram for the Ru_3O core, and Figure 6-14 shows qualitative MO diagrams for mixing of the cluster SOMO and pyridine π* orbitals of **3**$^{-}$-**5**$^{-}$. As discussed at length by Glover, Lear, and Kubiak,[16, 24] pyridines of differing donor ability inductively shift the energy levels of the cluster. More pertinent to this work is the allowed orbital mixing. In the case of clusters **4**$^{-}$-**6**$^{-}$, the mixing is such that the two allowed MLCT type transitions remain at nearly the same energies. The singly occupied HOMO has less pyridine π* character as the ligand becomes more donating. In other words, it looks more and more like the Ru_3O core, which explains slower intermolecular self-exchange as discussed in some detail in chapters 3 and 4.

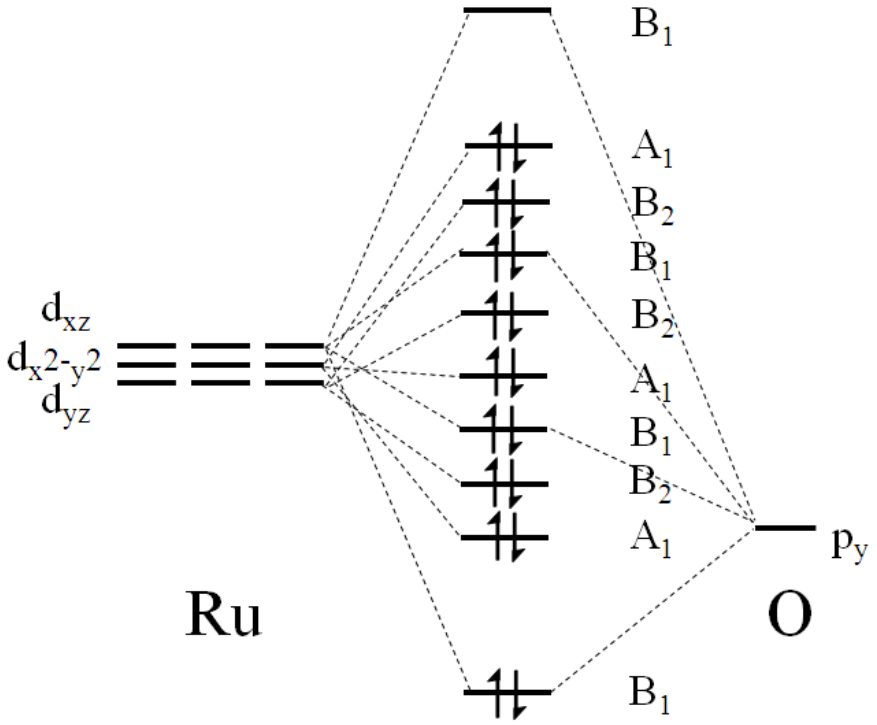

Figure 6-13. Qualitative molecular orbital diagram for the Ru_3O component of clusters **4**, **5**, and **6**. Clusters **1**, **2**, and **3** have similar electronic structure with slightly lower symmetry (C_S).

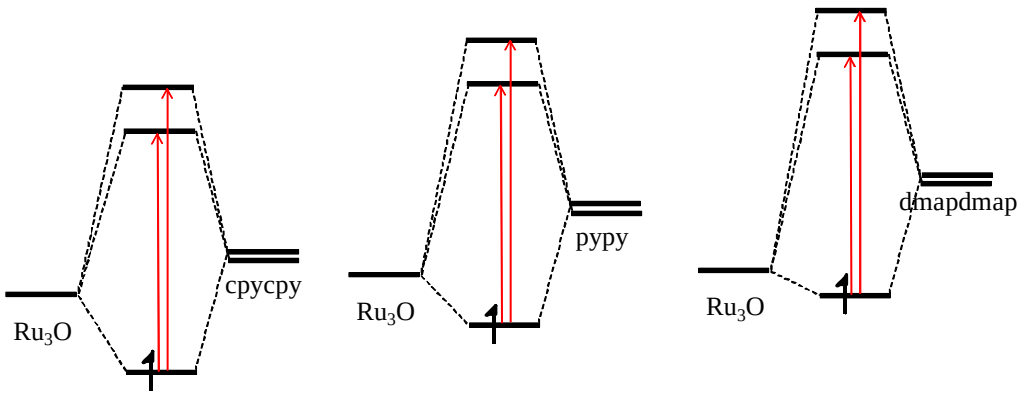

Figure 6-14. Qualitative molecular orbital diagrams showing allowed mixing for the cluster LUMO and pyridine ligand π* orbitals for the clusters **4**$^-$, **5**$^-$, and **6**$^-$.

Here this understanding provides a solid framework for discussion of the nicotinic acid substituted clusters **1**-**3**. The degree of orbital mixing in **4**$^-$-**6**$^-$ varies substantially, but the optical transition energies vary only slightly. The same is true in comparing the mixed valence species (**1**)$_2^-$

and $(\mathbf{2})_2^-$, consistent with the observations in Figure 6-9 and Table 6-2. However this line of reasoning can also help explain the difference between the mixed valence species $(\mathbf{1})_2^-$ and the doubly reduced isovalent $(\mathbf{1})_2^{2-}$. Qualitative MO diagrams for **1**, $(\mathbf{1})_2^-$ and $(\mathbf{1})_2^{2-}$ are shown in Figure 6-14.

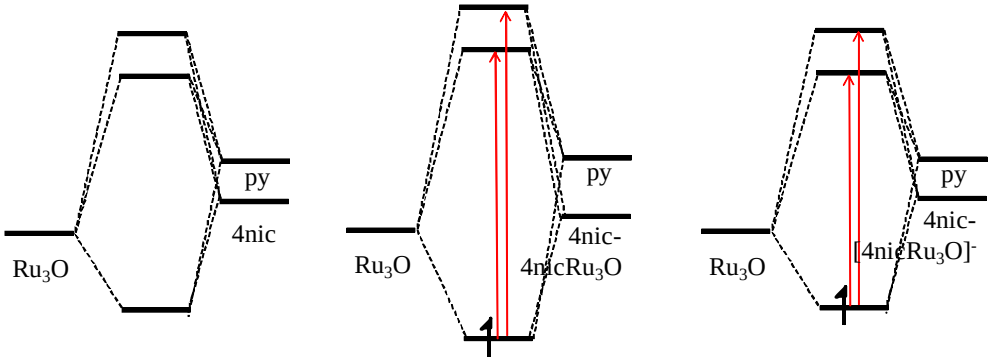

Figure 6-15. Qualitative molecular orbital diagrams for **1**, $(\mathbf{1})_2^-$ and $(\mathbf{1})_2^{2-}$.

In this MO description, the hydrogen bonding of the bridging ligand 4-nicotinic acid to another isonicotinic acid ligated to a ruthenium cluster appears to stabilize the 4nic π* orbital to a degree that mixing with the Ru_3O core is substantial. Increased mixing both stabilizes the SOMO and destabilizes the unoccupied orbitals. This stabilization is not seen in the doubly reduced dimer $(\mathbf{1})_2^{2-}$, indicating that hydrogen bonding brings about added delocalization (i.e. extension of the effective π* orbital) only in the mixed valence species. This description may be favored over the "stabilization of the ground state" initially used to explain this phenomenon[25] simply because it is more specific. Electroabsorption spectroscopy or resonance Raman spectroscopy with a tunable excitation wavelength would provide evidence for or against this description, but are both undertakings for another day.

6.6 Crystallography

A single crystal of **2** suitable for X-ray diffraction was grown from slow evaporation of a 1 mM solution in acetonitrile under ambient laboratory conditions. An ORTEP plot is shown in Figure

6-16. The structure is generally unremarkable except that it crystallizes as a monomer, with two acetonitrile molecules and two adventitious water molecules in the asymmetric unit. The two water molecules appear to stabilize the packing, with hydrogen bonding contacts to both the carboxylic acid group and an acetate group of a neighboring cluster. Attempts at crystallizing the mixed valence state and the fully reduced state have thus far been fruitless, but work continues.

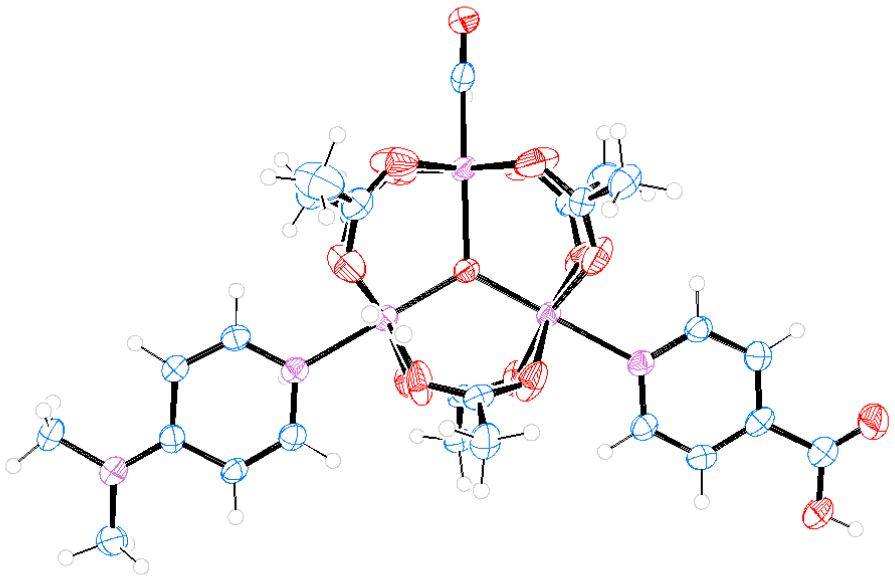

Figure 6-16. ORTEP (50% probability) of complex **2**. Solvent molecules have been omitted for clarity.

6.7 Conclusions

Complexes **1-3** have been characterized spectroscopically and electrochemically and exhibit unique properties attributed to the combination of mixed valency and hydrogen bonding. Our initial explanation was that this combination stabilizes the ground state for these mixed valence species by about 2500 cm^{-1}, or 7 kcal/mol. More specifically, MO theory points to increased orbital mixing due to the hydrogen bonding of the electron donor to an acceptor. If this is true, it would be more accurate to say that the HOMO-LUMO gap was increased by about 2500 cm^{-1}, and that the ground state was stabilized by somewhat less than that amount. The electrochemical splitting is highly scan

rate dependent, and extrapolation to infinitely slow scan rates gives thermodynamic $\Delta E_{1/2}$ values on the order of ~120 mV for both **1** and **2** at 1 mM in MeCN. The splitting is also concentration dependent, and a complete analytical expression accounting for both the concentration and scan rate dependence was not worked out at the time of this writing.

The fact that the stabilization observed in the electronic spectra and the thermodynamic splitting observed in cyclic voltammetry are comparable in $(\mathbf{1})_2^-$ and $(\mathbf{2})_2^-$ is consistent with attenuation of electronic communication by the large stabilization of the ground state relative to the bridge energy levels. Increasing the cluster energy level involved in the reduction with a more electron donating pyridine is insufficient to increase the stability from hydrogen bonding or electronic communication. Of course the electron transfer distance *r* could be quite small if electron density in the donor extends out onto the nicotinic acid π^* system as expected.

The bracketing of the electron transfer rate constant for $(\mathbf{3})_2^-$ as $1 \times 10^3\ s^{-1} < k_{ET} < 8.6 \times 10^4\ s^{-1}$ allows a bit more analysis. The Marcus-Hush expression,[4] as explained by Sutin,[26] attempts to relate λ, k_{ET}, and H_{ab} quantitatively. When applied to these mixed valence hydrogen bonded clusters, using $\lambda = 11000\ cm^{-1}$, H_{ab} is calculated to be quite small, on the order of 10-50 cm^{-1}, Figure 6-17. This is consistent with the conspicuous absence of a classical intervalence charge transfer (IVCT) band in the near-IR of the mixed valence species. Such a small magnitude of electronic coupling suggests that an IVCT band is indeed there, but is likely of low molar extinction coefficient and simply lost underneath the other absorptions in that region.

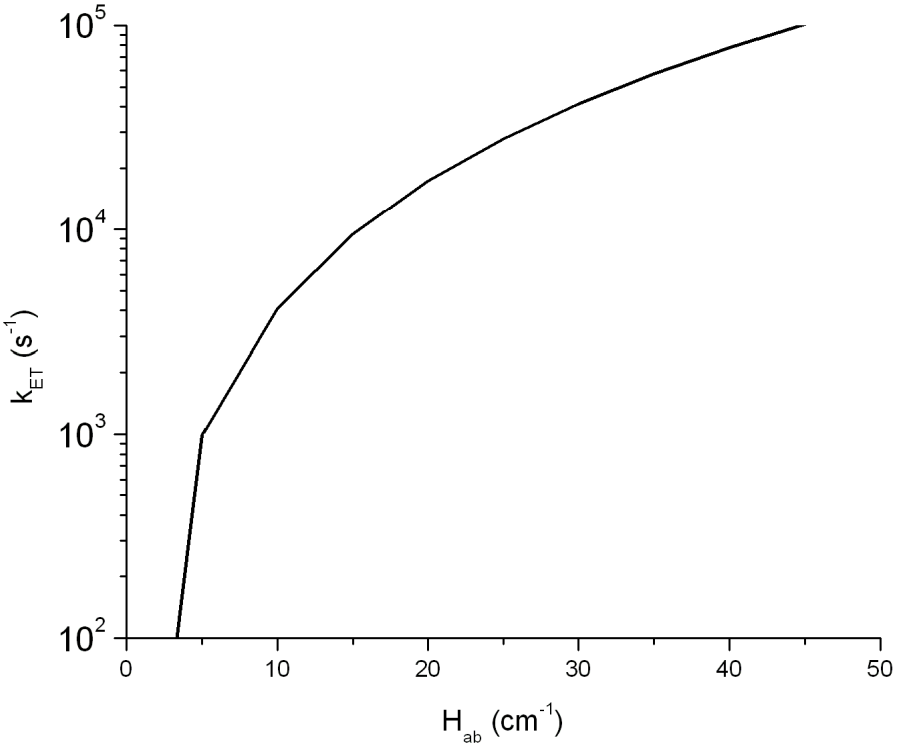

Figure 6-17. Calculated rate constants for given values of H_{ab} with λ = 11000 cm^{-1}.

6.8 Experimental

General. All chemicals were used as received unless otherwise noted. CD_3CN was distilled under nitrogen from CaH_2. Electrochemistry and spectroscopy solvents were sparged with argon and dried over alumina on a solvent system. Elemental analysis was performed by Numega Resonance Labs in San Diego, CA. Clusters **1** and **2** were unstable in solution at room temperature in the reduced states, particularly the doubly reduced dimers. At -20 ºC, the complexes were stable in acetonitrile, and fairly stable (for a period of minutes) in THF. Stability dictated the choice of solvents for the various experiments that otherwise might appear arbitrary. The reduced states appeared to be stable on the electrochemical timescale in all solvents investigated.

Synthesis and characterization. Complex **1** was synthesized by the usual methods,[13, 15] except that it was purified by reprecipitation instead of chromatography. $Ru_3O(OAc)_6(CO)(pyridine)(H_2O)$ (118 mg, 0.148 mmol) was stirred in 40 mL CH_2Cl_2 and 10 mL MeOH in an ice bath. Isonicotinic acid (190 mg, 1.54 mmol) was added as a solid over three minutes, and the reaction was allowed to come to room temperature slowly and stirred for 48 hours. It gradually turned from blue to teal in color. The reaction was rotavapped at 35 ºC. The residue was taken up in unstabilized CH_2Cl_2 and filtered through celite to remove excess isonicotinic acid. The solvent was reduced to a minimum, and the product was precipitated with excess hexanes, and collected on a frit. It was washed several times with hexanes, and dried on the frit overnight covered by a rubber stopper for a typical yield of 80%. If the compound degraded (as was observed over a matter of months of storage in a desiccator) it could be repurified by similar methods. ^{1}H NMR (500 MHz, DMSO-d6): δ ppm 9.00 (d, J = 6.30 Hz, 2 H), 8.96 (d, J = 4.58 Hz, 2 H), 8.57 (d, J = 6.30 Hz, 2 H), 8.35 (t, J = 8.02 Hz, 1 H), 8.22 (td, J = 6.30 Hz, 2 H), 1.94 (s, 6 H), 1.93 (s, 6 H), 1.72 (s, 6 H). UV/vis (CH_2Cl_2) nm (ε $M^{-1}s^{-1}$) 354 (5200), 408 (5100), 588 (6200). IR (KBr) cm^{-1} 3441 (br), 1950, 1736, 1716 (sh), 1609, 1573, 1449 (sh), 1424, 1349, 690. ESI MS (neg. mode) m/z calc. $(1\text{-}H^+)^-$ 903.8, found 903.5, $(1)_2^-$ calc 1807.7, found 1808.0. Elemental analysis: Calc. for $Ru_3O(OAc)_6(CO)(py)(4nic)$ $C_{24}H_{28}N_2O_{16}Ru_3$ C 31.90; H 3.12; N 3.10. Found 32.24; 3.23; 2.97.

Complex **2** was prepared in an analogous fashion. ^{1}H NMR (300 MHz, DMSO-d6): δ ppm 9.11 (d, J = 6.51 Hz, 2 H), 8.81 (d, J = 7.02 Hz, 2 H), 8.63 (d, J = 6.51 Hz, 2 H), 7.44 (t, J = 7.02 Hz, 2 H), 3.30 (s, 6 H), 1.93 (s, 6 H), 1.91 (s, 6 H), 1.70 (s, 6 H). UV/vis (CH_2Cl_2) nm (ε $M^{-1}s^{-1}$) 261 (6900), 313 (8100), 404 (3250), 590 (6500). IR (KBr) cm^{-1} 3444 (br), 1941, 1735, 1716 (sh), 1609, 1575, 1539, 1423, 1389, 1349, 1230, 1021, 688. ESI MS (neg. mode) m/z calc. $(\mathbf{2}\text{-}H^+)^-$ 947.9, found 946.1, $(\mathbf{2})_2^-$ calc 1890.79, found 1890.44. Elemental analysis: Calc. for $Ru_3O(OAc)_6(CO)(dmap)(4nic)\cdot 4H_2O$ $C_{26}H_{41}N_3O_{20}Ru_3$ C 30.65; H 4.06; N 4.12. Found C 30.49; H 4.08; N 4.26.

Complex **3** was prepared in an analogous fashion except that addition of 3-fluoropyridine to the carbonylated cluster required a brief reflux instead of the usual room temperature treatment. ^{1}H

NMR (300 MHz, DMSO-d6): δ ppm (note: 3fpy signals overlap with 4nic signals and two of the three acetate signals overlap) 9.01 (d, J = 6.5 Hz, 2 H), 8.78 (m, 2 H), 8.62 (d, J = 6.0 Hz, 2 H), 8.34 (m, 2 H), 2.00 (s, 12 H), 1.80 (s, 6 H). ^{19}F NMR (282 MHz, DMSO-d6): δ ppm -124.2 (s). UV/vis (MeCN) nm (ε $M^{-1}s^{-1}$) 365 (2600), 588 (2300). IR (KBr) cm^{-1} 3446 (br), 1953, 1737, 1716 (sh), 1607, 1573, 1483, 1441 (sh), 1424, 1388, 1349, 1260, 1240, 689. ESI MS (neg. mode) m/z calc. (**3**-H^+)$^-$ 921.8, found, 921.0 Elemental analysis: Calc. for $Ru_3O(OAc)_6(CO)(3fpy)(4nic)\bullet H_2O$ $C_{24}H_{29}FN_2O_{17}Ru_3$ C 30.68; H 3.11; N 2.98. Found C 30.73; H 3.44; N 3.07.

Sample Preparation. Samples for NMR, IR, and UV/vis/NIR experiments were prepared in a nitrogen-filled glove box. For NMR, a total of 0.6 mL for each sample was added to standard NMR tubes (500 MHz, Wilmad), capped, and sealed with tape. Samples for UV/vis/NIR were pipetted into a 0.1 mm path length quartz cuvette and sealed with a septum with PTFE tubing threaded through it. A solution of decamethylcobaltocene was taken up in a syringe, and the syringe was fitted onto the end of the tubing, sealing the system before removal from the glovebox. Samples were chilled to -20 ºC in a variable temperature sample compartment in the instrument before reducing agent was added.

UV/vis/NIR Data Collection. UV/vis/NIR data were collected on a Shimadzu UV-3600 UV/vis/NIR spectrometer at -20 ºC. Curve fitting of spectra to multiple Gaussian peaks was performed in Origin 6.0.

Infrared Data Collection. Infrared spectra were obtained on a Bruker Equinox 55 spectrometer using KBr, standard liquid cells, or a custom built reflectance spectroelectrochemical cell.[27]

NMR Data Collection and Analysis. ^{1}H spectra and ^{19}F (128 scans) were collected on a JEOL 500 MHz NMR spectrometer and analyzed using JEOL Delta software. Peaks were fit to Lorentzian lineshapes in the Delta software with no linebroadening.

Electrochemical Measurements. Electrochemistry was performed with a BAS Epsilon potentiostat in dried deoxygenated solvents with 0.1 M tetrabutylammonium hexafluorophosphate (TBAH, recrystallized from MeOH and dried under vacuum at 80 ºC) and 0.01-3 mM sample

concentrations in a dedicated glovebox. The working electrode was a gold disk (1.6 mm diameter). The counter electrode was a platinum wire, and the reference was the ferrocene/ferrocenium couple or a silver wire with Fc internal standard.

Crystallographic Structure Determination. The single-crystal X-ray structure determination was carried out at 100(2) K on a Bruker Kappa Diffractometer using Cu K_α radiation (λ = 1.54178 Å) in conjunction with a Bruker APEX-2 detector. The structure was solved by direct methods using Bruker Apex software using SHELXTL and refined with full-matrix least-squares procedures in SHELX-97[28] using OLEX2.[29]

6.9 Appendix

Table 6-3. Crystal data and structure refinement for complex **2**.

Identification code	shelxl	
Empirical formula	C30 H43 N5 O18 Ru3	
Formula weight	1064.90	
Temperature	100(2) K	
Wavelength	1.54178 Å	
Crystal system	Monoclinic	
Space group	P2(1)/n	
Unit cell dimensions	a = 14.0951(7) Å	α= 90°.
	b = 14.9495(8) Å	β= 108.636(3)°.
	c = 20.1290(10) Å	γ = 90°.
Volume	4019.1(4) $Å^3$	
Z	4	
Density (calculated)	1.760 Mg/m^3	
Absorption coefficient	9.710 mm^{-1}	
F(000)	2136	
Crystal size	0.10 x 0.10 x 0.05 mm^3	
Theta range for data collection	3.38 to 64.52°.	
Index ranges	-16<=h<=16, -17<=k<=17, -23<=l<=22	
Reflections collected	16851	

Table 6-3. Crystal data and structure refinement for complex **2**, continued.

Independent reflections	6618 [R(int) = 0.0366]
Completeness to theta = 60.00°	99.5 %
Absorption correction	Semi-empirical from equivalents
Max. and min. transmission	0.6424 and 0.4435
Refinement method	Full-matrix least-squares on F^2
Data / restraints / parameters	6618 / 6 / 528
Goodness-of-fit on F^2	1.029
Final R indices [I>2sigma(I)]	R1 = 0.0431, wR2 = 0.1148
R indices (all data)	R1 = 0.0576, wR2 = 0.1340
Largest diff. peak and hole	1.052 and -1.155 e.$Å^{-3}$

Table 6-4. Bond lengths [Å] and angles [°] for complex **2**.

Ru(1)-C(1)	1.845(7)
Ru(1)-O(1)	2.057(4)
Ru(1)-O(5)	2.062(5)
Ru(1)-O(3)	2.066(5)
Ru(1)-O(2)	2.071(5)
Ru(1)-O(4)	2.075(5)
Ru(2)-O(1)	1.899(4)
Ru(2)-O(6)	2.028(4)
Ru(2)-O(8)	2.040(4)
Ru(2)-O(7)	2.044(4)
Ru(2)-O(9)	2.051(4)
Ru(2)-N(1)	2.101(5)
Ru(3)-O(1)	1.895(4)
Ru(3)-O(12)	2.044(4)
Ru(3)-O(10)	2.048(4)
Ru(3)-O(11)	2.049(4)
Ru(3)-O(13)	2.051(4)
Ru(3)-N(2)	2.142(5)
O(2)-C(2)	1.233(8)
O(3)-C(4)	1.230(8)
O(4)-C(12)	1.228(8)
O(5)-C(10)	1.234(8)
O(6)-C(2)	1.231(8)
O(7)-C(6)	1.236(7)
O(8)-C(8)	1.253(7)
O(9)-C(4)	1.245(7)
O(10)-C(8)	1.241(7)
O(11)-C(6)	1.232(8)
O(12)-C(10)	1.236(8)
O(13)-C(12)	1.234(7)
O(14)-C(1)	1.146(8)
O(15)-C(26)	1.295(8)

Table 6-4. Bond lengths [Å] and angles [°] for complex **2**, continued.

O(15)-H(15)	0.8400
O(16)-C(26)	1.212(8)
N(1)-C(18)	1.349(8)
N(1)-C(14)	1.351(7)
N(2)-C(21)	1.334(7)
N(2)-C(25)	1.354(8)
N(2S)-C(3S)	1.168(12)
N(3)-C(16)	1.344(8)
N(3)-C(20)	1.449(8)
N(3)-C(19)	1.454(8)
C(2)-C(3)	1.512(9)
C(3)-H(3A)	0.9800
C(3)-H(3C)	0.9800
C(3)-H(3B)	0.9800
C(3S)-C(4S)	1.450(14)
C(4)-C(5)	1.516(8)
C(4S)-H(4SB)	0.9800
C(4S)-H(4SC)	0.9800
C(4S)-H(4SA)	0.9800
C(5)-H(5C)	0.9800
C(5)-H(5A)	0.9800
C(5)-H(5B)	0.9800
C(6)-C(7)	1.512(8)
C(7)-H(7A)	0.9800
C(7)-H(7C)	0.9800
C(7)-H(7B)	0.9800
C(8)-C(9)	1.497(8)
C(9)-H(9A)	0.9800
C(9)-H(9B)	0.9800
C(9)-H(9C)	0.9800
C(10)-C(11)	1.490(9)
C(11)-H(11C)	0.9800
C(11)-H(11A)	0.9800

Table 6-4. Bond lengths [Å] and angles [°] for complex **2**, continued.

C(11)-H(11B)	0.9800
C(12)-C(13)	1.515(9)
C(13)-H(13A)	0.9800
C(13)-H(13B)	0.9800
C(13)-H(13C)	0.9800
C(14)-C(15)	1.361(9)
C(14)-H(14)	0.9500
C(15)-C(16)	1.419(9)
C(15)-H(15A)	0.9500
C(16)-C(17)	1.410(8)
C(17)-C(18)	1.357(8)
C(17)-H(17)	0.9500
C(18)-H(18)	0.9500
C(19)-H(19B)	0.9800
C(19)-H(19C)	0.9800
C(19)-H(19A)	0.9800
C(20)-H(20A)	0.9800
C(20)-H(20C)	0.9800
C(20)-H(20B)	0.9800
C(21)-C(22)	1.372(8)
C(21)-H(21)	0.9500
C(22)-C(23)	1.395(9)
C(22)-H(22)	0.9500
C(23)-C(24)	1.380(9)
C(23)-C(26)	1.498(9)
C(24)-C(25)	1.366(9)
C(24)-H(24)	0.9500
C(25)-H(25)	0.9500
O(18)-H(18A)	0.852(10)
O(18)-H(18B)	0.853(10)
O(17)-H(17A)	0.856(10)
O(17)-H(17B)	0.853(10)
N(1S)-C(1S)	1.136(10)

Table 6-4. Bond lengths [Å] and angles [°] for complex **2**, continued.

C(1S)-C(2S)	1.421(13)
C(2S)-H(2SB)	0.9800
C(2S)-H(2SC)	0.9800
C(2S)-H(2SA)	0.9800
C(1)-Ru(1)-O(1)	179.1(2)
C(1)-Ru(1)-O(5)	89.0(2)
O(1)-Ru(1)-O(5)	90.61(17)
C(1)-Ru(1)-O(3)	89.3(2)
O(1)-Ru(1)-O(3)	91.12(16)
O(5)-Ru(1)-O(3)	178.27(19)
C(1)-Ru(1)-O(2)	88.2(2)
O(1)-Ru(1)-O(2)	92.61(17)
O(5)-Ru(1)-O(2)	84.8(3)
O(3)-Ru(1)-O(2)	95.0(3)
C(1)-Ru(1)-O(4)	86.7(2)
O(1)-Ru(1)-O(4)	92.58(17)
O(5)-Ru(1)-O(4)	95.6(3)
O(3)-Ru(1)-O(4)	84.4(3)
O(2)-Ru(1)-O(4)	174.79(19)
O(1)-Ru(2)-O(6)	95.48(18)
O(1)-Ru(2)-O(8)	94.68(16)
O(6)-Ru(2)-O(8)	169.71(19)
O(1)-Ru(2)-O(7)	93.86(17)
O(6)-Ru(2)-O(7)	85.0(3)
O(8)-Ru(2)-O(7)	92.7(2)
O(1)-Ru(2)-O(9)	94.68(16)
O(6)-Ru(2)-O(9)	93.0(2)
O(8)-Ru(2)-O(9)	87.8(2)
O(7)-Ru(2)-O(9)	171.38(17)
O(1)-Ru(2)-N(1)	178.44(17)
O(6)-Ru(2)-N(1)	85.27(19)
O(8)-Ru(2)-N(1)	84.61(17)

Table 6-4. Bond lengths [Å] and angles [°] for complex **2**, continued.

O(7)-Ru(2)-N(1)	87.56(18)
O(9)-Ru(2)-N(1)	83.92(17)
O(1)-Ru(3)-O(12)	94.07(16)
O(1)-Ru(3)-O(10)	94.59(16)
O(12)-Ru(3)-O(10)	171.27(17)
O(1)-Ru(3)-O(11)	94.19(16)
O(12)-Ru(3)-O(11)	85.7(2)
O(10)-Ru(3)-O(11)	92.5(2)
O(1)-Ru(3)-O(13)	95.57(16)
O(12)-Ru(3)-O(13)	92.2(2)
O(10)-Ru(3)-O(13)	88.1(2)
O(11)-Ru(3)-O(13)	170.13(17)
O(1)-Ru(3)-N(2)	177.83(16)
O(12)-Ru(3)-N(2)	87.29(17)
O(10)-Ru(3)-N(2)	84.09(17)
O(11)-Ru(3)-N(2)	87.59(17)
O(13)-Ru(3)-N(2)	82.68(17)
Ru(3)-O(1)-Ru(2)	121.66(19)
Ru(3)-O(1)-Ru(1)	119.47(19)
Ru(2)-O(1)-Ru(1)	118.87(18)
C(2)-O(2)-Ru(1)	134.0(4)
C(4)-O(3)-Ru(1)	132.3(4)
C(12)-O(4)-Ru(1)	134.3(5)
C(10)-O(5)-Ru(1)	132.7(4)
C(2)-O(6)-Ru(2)	132.9(5)
C(6)-O(7)-Ru(2)	132.3(4)
C(8)-O(8)-Ru(2)	132.2(4)
C(4)-O(9)-Ru(2)	133.4(4)
C(8)-O(10)-Ru(3)	132.1(4)
C(6)-O(11)-Ru(3)	131.8(4)
C(10)-O(12)-Ru(3)	133.1(4)
C(12)-O(13)-Ru(3)	133.3(4)
C(26)-O(15)-H(15)	109.5

Table 6-4. Bond lengths [Å] and angles [°] for complex **2**, continued.

C(18)-N(1)-C(14)	116.8(5)
C(18)-N(1)-Ru(2)	121.9(4)
C(14)-N(1)-Ru(2)	121.2(4)
C(21)-N(2)-C(25)	117.2(5)
C(21)-N(2)-Ru(3)	122.2(4)
C(25)-N(2)-Ru(3)	120.6(4)
C(16)-N(3)-C(20)	121.1(5)
C(16)-N(3)-C(19)	120.4(5)
C(20)-N(3)-C(19)	117.8(6)
O(14)-C(1)-Ru(1)	178.1(6)
O(6)-C(2)-O(2)	126.7(6)
O(6)-C(2)-C(3)	116.0(6)
O(2)-C(2)-C(3)	117.4(6)
C(2)-C(3)-H(3A)	109.5
C(2)-C(3)-H(3C)	109.5
H(3A)-C(3)-H(3C)	109.5
C(2)-C(3)-H(3B)	109.5
H(3A)-C(3)-H(3B)	109.5
H(3C)-C(3)-H(3B)	109.5
N(2S)-C(3S)-C(4S)	178.7(9)
O(3)-C(4)-O(9)	127.3(6)
O(3)-C(4)-C(5)	116.0(6)
O(9)-C(4)-C(5)	116.7(6)
C(3S)-C(4S)-H(4SB)	109.5
C(3S)-C(4S)-H(4SC)	109.5
H(4SB)-C(4S)-H(4SC)	109.5
C(3S)-C(4S)-H(4SA)	109.5
H(4SB)-C(4S)-H(4SA)	109.5
H(4SC)-C(4S)-H(4SA)	109.5
C(4)-C(5)-H(5C)	109.5
C(4)-C(5)-H(5A)	109.5
H(5C)-C(5)-H(5A)	109.5
C(4)-C(5)-H(5B)	109.5

Table 6-4. Bond lengths [Å] and angles [°] for complex **2**, continued.

H(5C)-C(5)-H(5B)	109.5
H(5A)-C(5)-H(5B)	109.5
O(11)-C(6)-O(7)	126.2(6)
O(11)-C(6)-C(7)	117.5(5)
O(7)-C(6)-C(7)	116.2(6)
C(6)-C(7)-H(7A)	109.5
C(6)-C(7)-H(7C)	109.5
H(7A)-C(7)-H(7C)	109.5
C(6)-C(7)-H(7B)	109.5
H(7A)-C(7)-H(7B)	109.5
H(7C)-C(7)-H(7B)	109.5
O(10)-C(8)-O(8)	126.4(5)
O(10)-C(8)-C(9)	116.1(5)
O(8)-C(8)-C(9)	117.4(5)
C(8)-C(9)-H(9A)	109.5
C(8)-C(9)-H(9B)	109.5
H(9A)-C(9)-H(9B)	109.5
C(8)-C(9)-H(9C)	109.5
H(9A)-C(9)-H(9C)	109.5
H(9B)-C(9)-H(9C)	109.5
O(5)-C(10)-O(12)	127.1(6)
O(5)-C(10)-C(11)	116.6(5)
O(12)-C(10)-C(11)	116.3(5)
C(10)-C(11)-H(11C)	109.5
C(10)-C(11)-H(11A)	109.5
H(11C)-C(11)-H(11A)	109.5
C(10)-C(11)-H(11B)	109.5
H(11C)-C(11)-H(11B)	109.5
H(11A)-C(11)-H(11B)	109.5
O(4)-C(12)-O(13)	126.5(6)
O(4)-C(12)-C(13)	115.9(6)
O(13)-C(12)-C(13)	117.6(6)
C(12)-C(13)-H(13A)	109.5

Table 6-4. Bond lengths [Å] and angles [°] for complex **2**, continued.

C(12)-C(13)-H(13B)	109.5
H(13A)-C(13)-H(13B)	109.5
C(12)-C(13)-H(13C)	109.5
H(13A)-C(13)-H(13C)	109.5
H(13B)-C(13)-H(13C)	109.5
N(1)-C(14)-C(15)	123.8(5)
N(1)-C(14)-H(14)	118.1
C(15)-C(14)-H(14)	118.1
C(14)-C(15)-C(16)	120.1(5)
C(14)-C(15)-H(15A)	120.0
C(16)-C(15)-H(15A)	120.0
N(3)-C(16)-C(17)	123.0(5)
N(3)-C(16)-C(15)	122.0(5)
C(17)-C(16)-C(15)	115.0(5)
C(18)-C(17)-C(16)	121.3(5)
C(18)-C(17)-H(17)	119.4
C(16)-C(17)-H(17)	119.4
N(1)-C(18)-C(17)	123.1(5)
N(1)-C(18)-H(18)	118.5
C(17)-C(18)-H(18)	118.5
N(3)-C(19)-H(19B)	109.5
N(3)-C(19)-H(19C)	109.5
H(19B)-C(19)-H(19C)	109.5
N(3)-C(19)-H(19A)	109.5
H(19B)-C(19)-H(19A)	109.5
H(19C)-C(19)-H(19A)	109.5
N(3)-C(20)-H(20A)	109.5
N(3)-C(20)-H(20C)	109.5
H(20A)-C(20)-H(20C)	109.5
N(3)-C(20)-H(20B)	109.5
H(20A)-C(20)-H(20B)	109.5
H(20C)-C(20)-H(20B)	109.5
N(2)-C(21)-C(22)	123.0(6)

Table 6-4. Bond lengths [Å] and angles [°] for complex **2**, continued.

N(2)-C(21)-H(21)	118.5
C(22)-C(21)-H(21)	118.5
C(21)-C(22)-C(23)	119.0(6)
C(21)-C(22)-H(22)	120.5
C(23)-C(22)-H(22)	120.5
C(24)-C(23)-C(22)	118.6(5)
C(24)-C(23)-C(26)	120.0(6)
C(22)-C(23)-C(26)	121.4(6)
C(25)-C(24)-C(23)	118.4(6)
C(25)-C(24)-H(24)	120.8
C(23)-C(24)-H(24)	120.8
N(2)-C(25)-C(24)	123.7(5)
N(2)-C(25)-H(25)	118.1
C(24)-C(25)-H(25)	118.1
O(16)-C(26)-O(15)	124.0(6)
O(16)-C(26)-C(23)	122.2(6)
O(15)-C(26)-C(23)	113.7(6)
H(18A)-O(18)-H(18B)	109(3)
H(17A)-O(17)-H(17B)	107(3)
N(1S)-C(1S)-C(2S)	175.7(10)
C(1S)-C(2S)-H(2SB)	109.5
C(1S)-C(2S)-H(2SC)	109.5
H(2SB)-C(2S)-H(2SC)	109.5
C(1S)-C(2S)-H(2SA)	109.5
H(2SB)-C(2S)-H(2SA)	109.5
H(2SC)-C(2S)-H(2SA)	109.5

Symmetry transformations used to generate equivalent atoms:

6.10 References

1. Brunschwig, B. S.; Creutz, C.; Sutin, N., *Chem. Soc. Rev.* **2002,** *31*, 168-184.

2. Cukier, R. I.; Nocera, D. G., *Annu. Rev. Phys. Chem.* **1998,** *49*, 337-369.

3. Hammes-Schiffer, S., *Acc. Chem. Res.* **2001,** *34*, 273-281.

4. Marcus, R. A., *Annu. Rev. Phys. Chem.* **1964,** *15*, 155.

5. Mayer, J. M., *Annu. Rev. Phys. Chem.* **2004,** *55*, 363-390.

6. Robin, M. B.; Day, P., *Adv. Inorg. Chem. Radiochem.* **1967,** *10*, 247.

7. Dempsey, J. L.; Esswein, A. J.; Manke, D. R.; Rosenthal, J.; Soper, J. D.; Nocera, D. G., *Inorg. Chem.* **2005,** *44*, 6879-6892.

8. Derege, P. J. F.; Williams, S. A.; Therien, M. J., *Science* **1995,** *269*, 1409-1413.

9. Irebo, T.; Reece, S. Y.; Sjödin, M.; Nocera, D. G.; Hammarström, L., *J. Am. Chem. Soc.* **2007,** *129*, 15462-15464.

10. Sun, H.; Steeb, J.; Kaifer, A. E., *J. Am. Chem. Soc.* **2006,** *128*, 2820-2821.

11. Goeltz, J. C.; Benson, E. E.; Kubiak, C. P., *J. Phys. Chem. B* **2010,** *114*, 14729-14734.

12. Goeltz, J. C.; Hanson, C. J.; Kubiak, C. P., *Inorg. Chem.* **2009,** *48*, 4763-4767.

13. Ito, T.; Hamaguchi, T.; Nagino, H.; Yamaguchi, T.; Kido, H.; Zavarine, I. S.; Richmond, T.; Washington, J.; Kubiak, C. P., *J. Am. Chem. Soc.* **1999,** *121*, 4625-4632.

14. Lear, B. J.; Glover, S. D.; Salsman, J. C.; Londergan, C. H.; Kubiak, C. P., *J. Am. Chem. Soc.* **2007,** *129*, 12772-12779.

15. Salsman, J. C.; Ronco, S.; Londergan, C. H.; Kubiak, C. P., *Inorg. Chem.* **2006,** *45*, 547-554.

16. Glover, S. D.; Lear, B. J.; Salsman, J. C.; Londergan, C. H.; Kubiak, C. P., *Phil. Trans. Roy. Soc. A* **2008,** *366*, 177-185.

17. Goeltz, J. C.; Kubiak, C. P., *J. Am. Chem. Soc* **2010**, submitted.

18. Walsh, J. L.; Baumann, J. A.; Meyer, T. J., *Inorg. Chem.* **1980,** *19*, 2145-2151.

19. Baumann, J. A.; Salmon, D. J.; Wilson, S. T.; Meyer, T. J.; Hatfield, W. E., *Inorg. Chem.* **1978,** *17*, 3342-3350.

20. Baumann, J. A.; Wilson, S. T.; Salmon, D. J.; Hood, P. L.; Meyer, T. J., *J. Am. Chem. Soc.* **1979,** *101*, 2916-2920.

21. Toma, H. E.; Cunha, C. J.; Cipriano, C., *Inorg. Chim. Acta* **1988,** *154*, 63-66.

22. Sandstrom, J., *Dynamic NMR spectroscopy*. Academic Press: 1982.

23. D'Alessandro, D. M.; Keene, F. R., *Chem. Rev.* **2006,** *106*, 2270-2298.

24. Lear, B. J.; Glover, S. D.; Salsman, J. C.; Londergan, C. H.; Kubiak, C. P., *J. Am. Chem.Soc.* **2007,** *129*, 12772-12779.

25. Goeltz, J. C.; Kubiak, C. P., *J. Am. Chem. Soc* **2010,** *132*, 17390-17392.

26. Sutin, N., *Prog Inorg Chem* **1983,** *30*, 441-498.

27. Zavarine, I. S.; Kubiak, C. P., *J. Electroanal. Chem.* **2001,** *495*, 106-109.

28. Sheldrick, G. M., *Acta Cryst. A* **2008,** *64*, 112-122.

29. Dolomanov, O. V.; Bourhis, L. J.; Gildea, R. J.; Howard, J. A. K.; Puschmann, H., *J. Appl. Cryst.* **2009,** *42*, 339-341.